Influence and reactivation of pre-existing rift faults during the development of an overlying fault network, northern Browse Basin, NW Australia

Eirik Wiese

Master thesis in

Petroleum Geoscience

Department of Earth Science

University of Bergen

September 2017

Abstract

Focusing on multiple events and interaction of different fault networks with the time being common in extensional settings such as passive margins and continental rifts. This study aims to better understand the interaction in normal fault networks and the influence of pre-existing structures on fault network growth and development. This is done by interpretation on 3-D reflection seismic volumes in the northern Caswell Sub-basin in the Browse Basin offshore the Australian NW Shelf. The focus is towards structural analysis of geometries, throw, spatial heterogeneity, characterise and analyse interactions and the influence of reactivation on underlying major rift faults.

The normal fault network comprise Paleozoic-Mesozoic underlying ENE-trending rift faults setting up series of horsts and grabens. Above the rift-structures, is the ENE- to E-trending Neogene faults mostly spatially arranged as conjugated fault sets in en-echelon arrays. The spatial heterogeneity analysis and throw distribution show areas of distributed faulting with several faults and low throws, and areas of more localised faulting with fewer faults and greater throws. The high throws at Neogene faults match spatially with high throws at the rift faults, often at segments with geometric connection between the two fault populations.

Interpretation of time-thickness maps show greatest amount of syn-rift activity in Permian and Triassic and lesser activity in Jurassic and Early Cretaceous, although basin sag is the main mechanism for thickening in Early Cretaceous. Extensional stress imposed in Miocene with similar orientation to pre-existing faults, cause nucleation of Neogene faults that dip-propagate simultaneously as pre-existing faults reactivate. Rotational splays created through the Cretaceous succession, connect the two fault populations by geometric linkage. These fault planes possess a throw minimum at the point of linkage close to the Turonian horizon, which might increase in throw with time as faults reach further equilibration stages.

This study generally highlight the importance of pre-existing structures within a multiphase extension fault network, as these function as preferred nucleation sites and control strain distribution within the later developed Neogene fault population. Both through kinematic influence with soft-linkage and geometric control with hard-linkage developed by reactivation. This has implications for the regional geology and exploration, as connected faulting and reactivation might be more extensive than previously thought. This can ultimately cause effects for trap integrity and hydrocarbon migration.

II

Acknowledgments

Table of Contents

1 Introduction

1.1 Rationale and background

In extensional settings such as continental rifts and passive margins brittle deformation is largely accommodated by normal fault networks. A normal fault network can form through one or several extensional events, with variations in extensional directions. In a single-phase extension event strain localisation can occur as faulting progresses (Mcleod *et al.*, 2000; Walsh *et al.*, 2003; Cowie *et al.*, 2005; Soliva and Schulz, 2008) to produce linked sub-horizontal and en-echelon faulting (e.g. Gawthorpe and Leeder, 2000). However, normal fault networks seen at rifts and passive margins commonly develop through multiple extension phases (e.g. Færseth, 1996; Morley *et al*., 2004; Frankowicz and McClay, 2010). This can result in geometric, kinematic and mechanical interaction between the different stress regimes and phases of faulting, producing more complex networks with a diversity of geometries, abutting and cross-cutting relationships, fault reactivation etc (e.g. Segall and Pollard, 1983; Nixon *et al*., 2014; Fossen and Rotevatn, 2016). Multiple aspects, such as the geometry of the pre-existing faults (e.g. Morley *et al*., 2004; Reeve *et al*., 2015) and local perturbation of the stress field (Maerten *et al*., 1999; 2002; Henza *et al*., 2010) will influence the final architecture of the fault network. However, the most important factor is the orientation difference between the pre-existing faults and the later imposed extensional phase(s) (Bonini *et al*., 1997; Henza *et al*., 2011; Henstra *et al*., 2015). Knowledge of the interactions between different phases of faulting is thus vital for understanding growth and development of fault networks in extensional settings.

Normal faults within a network grow by several events of incremental slip and may propagate vertically and/or horizontally as an isolated fault (Cowie and Scholz, 1992; Manzocchi *et al*., 2006; Mouslopoulou *et al*., 2009). The isolated faults can originate as spatially independent faults (Walsh and Watterson, 1988; Trudgill and Cartwright, 1994; Cartwright *et al*., 1995; Dawers and Anders, 1995; Cowie, 1998; Cowie *et al*., 2000; Walsh *et al*., 2003), that might propagate and interact kinematically, through the transfer of displacement, and later geometrically connect by breaching of relay ramp separating two overlapping faults (Peacock and Sanderson, 1991, 1994; Trudgill and Cartwright, 1994; Peacock, 2002; Fossen and Rotevatn, 2016). Alternatively, faults may originate in kinematic-interaction to another fault and then proceed in a similar fashion (Walsh *et al*., 2002, 2003; Giba *et al*., 2012). In either case numerous normal faults will grow and interact forming a fault network, however the

organisation and spatial development of the fault networks can be strongly influenced by pre-existing structures (Nixon *et al*., 2014).

Furthermore, pre-existing faults can reactivate and undergo new slip events, after being tectonically silent (Sibson, 1985; Holdsworth *et al*., 1997; Peacock, 2002), when exposed to new extensional events (e.g. Dewey and Burke, 1973; Daly *et al*., 1989; Kim *et al*., 2001; Bailey *et al*., 2005). Pre-existing faults are considered as weakness zones and are therefore an inviting target for strain (Daly *et al*., 1989; Prucha, 1992; Holdsworth *et al*., 1997; Morley *et al*., 2004). Thus they are more likely to reactivate if the later inflicting extensional phase is preferentially orientated in relation to the pre-existing fault orientation (Richard and Krantz, 1991; Bellahsen and Daniel, 2005; Baudon and Cartwright, 2008). Such reactivation can occur regionally or locally in a fault network (Nixon *et al*., 2014). Fault reactivation can occur by upward propagation of the pre-existing fault (Richard and Krantz, 1991; Nicol *et al.*, 2005; Baudon and Cartwright, 2008), or by downward propagation by a newly formed fault and resulting dip-linkage (e.g. Baudon and Cartwright, 2008). However, the extent of reactivation has not been quantified and it is still not fully understood why some faults reactivate in preference to other faults (e.g. Butler *et al*., 1997; Kelly *et al*., 1999; Baudon and Cartwright, 2008). Thus the importance of understanding reactivation of pre-existing structures and the influence on the strain distribution by faulting.

The petroleum industry has a large amount of their activity located on passive margins and rift settings, where fault networks are present (e.g. De Charpal *et al*., 1978; Ravnås *et al*., 2000). These fault networks and the interactions within are of particular interest to the petroleum industry, due to faults having the ability to create pathways or barriers for fluids and hydrocarbons, resulting in migration, traps and compartmentalization of reservoirs (Bouvier *et al*., 1989; Leveille *et al*., 1997; Aydin, 2000). Additionally fault interactions and reactivation cause effects on the overall reservoir quality and heterogeneity, by influencing trap integrity and location of spill-points (e.g. Horstad and Larter, 1997; Fossen *et al*., 2005; Gartrell *et al*., 2006; Ferrill *et al*., 2009). Furthermore, faults develop through numerous slip events, consequently in importance to seismic hazard assessments (King, 1986; Sibson, 1989; Nicol *et al*., 2010; Quigley *et al*., 2012). Normal fault networks are especially important as seismic events have the ability to move across faults and produce a larger rupture than predicted (e.g. Wesnousky, 1986; Sieh *et al*., 1993). Thus, there is a need to study and quantify the spatial distribution of faulting and throw, and document the interactions between different extension

phases and resulting fault populations, particularly where parts of the underlying fault population may reactivate.

1.2 Aim and objective

The aim of this MSc thesis is to better understand the interaction in normal fault networks and the influence of pre-existing structures on fault network growth and development. To do this I study the interaction of two generations of fault population in the Browse Basin offshore NW Australia. The two fault populations comprise an earlier Paleozoic-Mesozoic fault network and a later Neogene fault network, which are imaged and mapped in detail using 3-D and 2-D seismic reflection data. The fault populations are structurally analysed focusing on investigating geometry, variations in throw, spatial heterogeneity of faulting in order to characterise fault interactions and reactivation. The specific objectives of the thesis are:

1. Characterise the interactions between the two fault populations.
2. Analyse the distribution of faulting and strain within an overlying fault population and assess the influence of larger pre-existing underlying faults.
3. Illustrate the reactivation of larger underlying major rift faults as a response to more than one imposed extensional event.
4. Improve knowledge of the structural development of the Australian North West Shelf.

These aims and objectives will contribute to the understanding of fault network growth with one actively affecting fault population, accompanied with reactivation of pre-existing structures on a passive margin.

1.3 Thesis outline

After this short and concise introduction (chapter 1), follows chapter 2 with an insight into the theory that give the basis of the research, featuring fault networks, fault propagation with linkage and reactivation. Chapter 3 provides a walkthrough of the regional geological evolution of the Australian North West Shelf, and the structural/stratigraphic framework of the Browse Basin. Chapter 4 introduces the provided data used in the survey and, moreover, the methods applied for interpretation of the seismic data and the traditional and novel analysis techniques

used. In Chapter 5 are the first results presented, featuring main structures and characteristics, opening with main rift faults and basement structure leading onto the Neogene faulting, before ending with evidence of rift fault activity. Chapter 6 comprises the results of the fault network analysis, including the organization of faulting, distribution of throw and spatial heterogeneity analysis. Chapter 7 concentrates on the interaction of Paleozoic-Mesozoic rift faults and Neogene faults, with a focus on the relationship between fault throw and fault frequency and linkage between reactivated rift faults and individual Neogene faults. Chapter 8 will discuss the results concerning interactions between the two fault populations, strain localisation, reactivation and the implications for regional geology. Before ending with a conclusion and suggestions to further work in chapter 9.

2 Theoretical background

2.1 Normal fault networks

Normal faults are discontinuities that accommodate brittle extensional strain in the Earth's crust. However, they rarely form individually, instead accommodating strain as a network of faults, in settings such as foreland basins (e.g. Roure *et al*., 1992; Chou, 1999), intracontinental rifts (e.g. Contreras *et al*., 2000; Scholz and Hutchinson, 2000) and passive margins (e.g. De Charpal *et al*., 1978; Færseth, 1996; Ravnås *et al*., 2000). Within such normal fault networks, faults will show an array of variations in lengths, sizes and orientations (Peacock, 2002; Nixon *et al*., 2014; Peacock *et al*., 2016). A network can consist of faults being geometrically and/or kinematically linked through wall-rock deformations (e.g. Peacock and Sanderson, 1991; Soliva and Benedicto, 2004; Bull *et al*., 2006; Nicol *et al*., 2010). Potentially forming an interconnected network of normal faults (e.g. Duffy *et al*., 2015; Deng *et al*., 2017)

The faults within the network can be as simply orientated as en-echelon or colinear fault sets, developed through one single phase of extension (e.g. Gawthorpe and Leeder, 2000) (Fig. 2.1). Originating with distributed strain and accompanying numerous smaller faults (Fig. 2.1a) (Mcleod *et al.*, 2000; Cowie *et al*., 2005; Soliva and Schulz, 2008). As the extension progresses, the faults interact and link to form larger linked faults (Cartwright *et al*., 1996; Gupta *et al.*, 1998; Peacock, 2002). The strain becomes localised in these larger faults, and smaller intracontinental faults turn inactive (Fig. 2.1b) (Mcleod *et al.*, 2000; Walsh *et al*., 2003; Cowie *et al.*, 2005; Soliva and Schulz, 2008), accompanied with increasing subsidence rates as an corresponding effect (Gupta *et al.*, 1998).

Normal fault networks usually develop through more than one phase of extension, as is the case in the Ethiopian rift (Bonini *et al.*, 1997), the Westralian superbasin (Struckmeyer *et al.*, 1998; Frankowicz and McClay, 2010), Gulf of Thailand (e.g. Morley *et al*., 2004; Morley 2007) and the Northern North Sea rift (Færseth, 1996; Whipp *et al.*, 2014; Henstra *et al.*, 2015). In such fault populations, the geometry (orientation, type, spacing and weakness) of the first phase structural grain actively affect the developing network (e.g. Morley *et al*., 2004; Reeve *et al*., 2015). Thus, the underlying first-phase faults can exhibit a structural control on a growing fault network by influencing fault geometries, orientations and nucleation locations, as well as the distribution of displacement and localisation of fault-controlled depocenters (Daly *et al*., 1989; Bonini *et al.*, 1997; Keep and McClay, 1997; Bailey *et al*., 2005; Bellahsen and Daniel, 2005;

Henza *et al*., 2011; Duffy *et al*., 2015; Henstra *et al*., 2015). In addition, pre-existing faults can cause local perturbation of the stress field, due to mechanical interference between intersecting faults. This can further lead to formation of non-synchronous faults (Fig. 2.2) (Maerten *et al*., 1999; 2002; Henza *et al*., 2010).
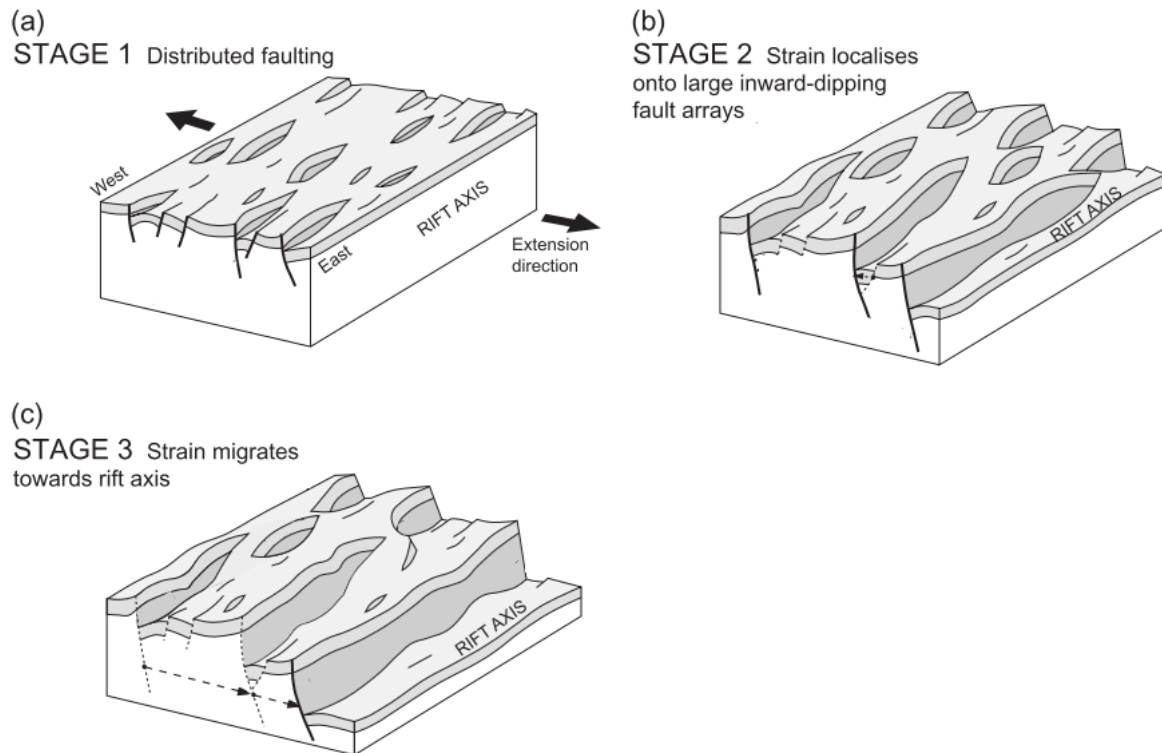
Figure. 2.1: Schematic block diagram, displaying the progressive evolution of a fault network with one extension phase, through time. Where strain become localised, as stress progresses. Modified from Cowie *et al*. (2005)

A multiphase extension fault network can be developed by stress systems with the same overall orientation (e.g. Zhang and Sanderson, 1996; Aksari *et al*., 2010) forming conjugating fault sets (e.g. Nicol *et al*., 1995; Ferrill *et al*., 2009). Further, it can also be developed by superposition of two or more stress fields with segmented en-echelon faults (e.g. Frankowicz and McClay, 2010; Giba *et al*., 2012; Brune, 2014), or variating cross-cutting orientations (Fig. 2.2) (e.g. Bonini *et al*., 1997; Keep and McClay, 1997; Kim *et al*., 2001; McClay *et al*., 2002; Bailey *et al*., 2005). The faults within a cross-cutting fault network can be separated into groups on behalf of their geometry and properties: Geometrically isolated faults (isolated faults) (e.g. Segall and Pollard, 1983; Frankowicz and McClay, 2010), geometrically isolated segmented faults (individual faults) (e.g. Segall and Pollard, 1980; Nixon *et al*., 2014; Fossen and Rotevatn, 2016), a smaller fault obliquely connected to a larger fault (splay) (e.g. Dawers and Anders,

1995; Nixon *et al*., 2014) , faults terminating at interaction to a fault with a different orientation (abutting faults) (e.g. Nixon *et al*., 2014; Duffy *et al*., 2015, 2017) and a reactivated fault segment between two abutting faults (Trailing fault)(e.g. Maerten *et al*., 1999, 2002; Nixon *et al*., 2014).
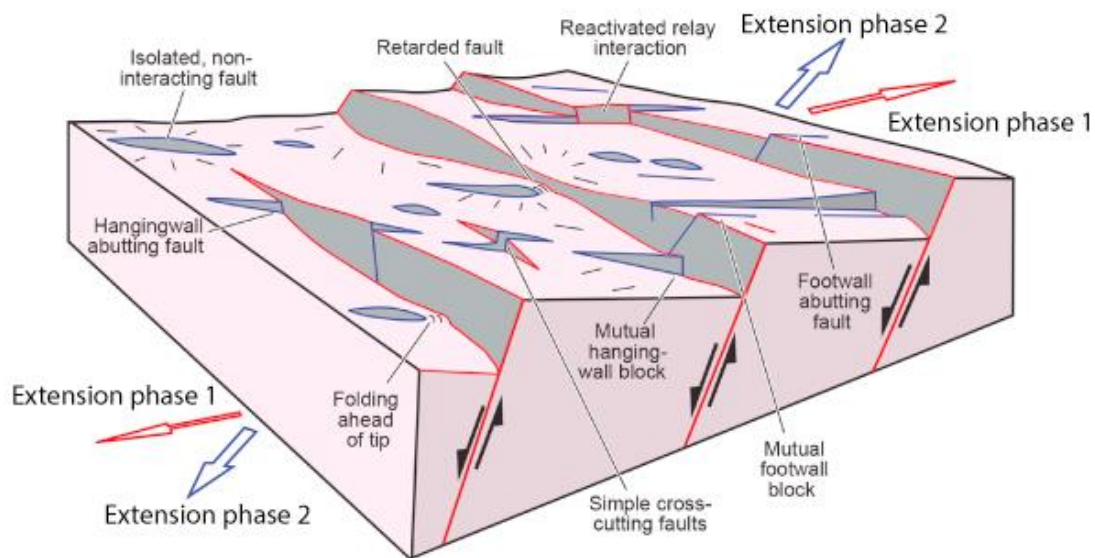

Figure. 2.2: Block diagram displaying variations in interconnected faults, formed in a network exposed to two extension phases with different orientation. Modified from Duffy *et al*. (2015)

Normal fault networks are built up by several faults that propagate and interact, with damage zones, which are areas of increased stress and connectivity favourable for hydrothermal flow (Curewitz and Karson, 1997; Zhang and Sanderson, 1998). Hence, understanding the arrangement and interactions between fault sets are important, due to fault interactions ability to create pathways or traps for fluids/hydrocarbons (Aydin, 2000) or block fluids/hydrocarbons, creating compartmentalization of aquifers (Bouvier *et al*., 1989; Leveille *et al*., 1997; Richards *et al*., 2015). Such hydrocarbon traps can be affected by fault interaction and reactivation, causing loss in trap integrity and changing location of spill point (Horstad and Larter, 1997; Gartrell *et al*., 2006; Ferrill *et al*., 2009). In addition to affecting fluids, do fault zones have localisation and deposition of metal ores and minerals (Norton and Knapp, 1977; Kerrich, 1986). Furthermore, faults interact during variating timespans from single earthquakes to million years (e.g. Bull *et al*., 2006; Nicol *et al*., 2010). Hence, fault networks are in general interest for seismic hazard and earthquake risk assessments (King, 1986; Sibson, 1989; Nicol *et al*., 2010; Quigley *et al*., 2012), especially in normal fault networks as seismic events have

the ability to shift between faults and produce a larger rupture than anticipated (e.g. Wesnousky, 1986; Sieh *et al.*, 1993).

2.2 Fault growth, linkage and interaction

The evolution of a fault network holds the growth of faults in several ways. A single isolated fault grow by incremental slip events and may propagate either laterally or vertically (Cowie and Scholz, 1992; Manzocchi *et al.*, 2006; Mouslopoulou *et al.*, 2009), and a fault growth with a linear relationship between the two is termed radial growth (fig. 2.3) (Walsh and Watterson, 1988; Cartwright *et al.*, 1995, 1996). As these smaller isolated fault segments propagate, they might start to interact kinematically and geometrically (Peacock and Sanderson 1991, 1994; Dawers and Anders, 1995). Two horizontally overlapping normal faults with kinematic interaction might form a relay ramp between them (Fig. 2.4). Which is a ductile deformed feature between two faults that interconnect hanging wall with footwall (Larsen, 1988; Peacock and Sanderson, 1991; Walsh *et al.*, 1999; Rotevatn *et al.*, 2007). At this stage, the faults are soft-linked and are still isolated segments (Fig. 2.5ii). As the faults continue to build up displacement, they start to interact and form a through-going linkage, resulting in breaching of the ramp (Fig. 2.5iii) (Peacock and Sanderson, 1991, 1994; Trudgill and Cartwright, 1994; Peacock, 2002; Fossen and Rotevatn, 2016).
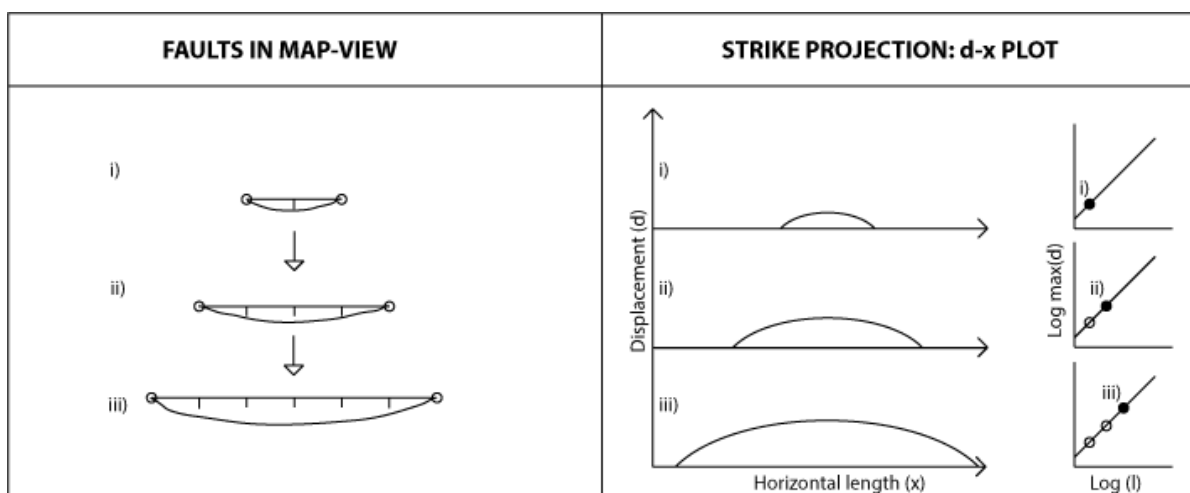

Figure. 2.3: Display the radial growth of a normal fault with time. Progressing time from i) to iii). As the fault tips propagate, the maximum displacement increase. The logarithmic graph shows a linear growth in the ratio between length and max displacement, from start to end. Redrawn from Cartwright *et al.* (1995).
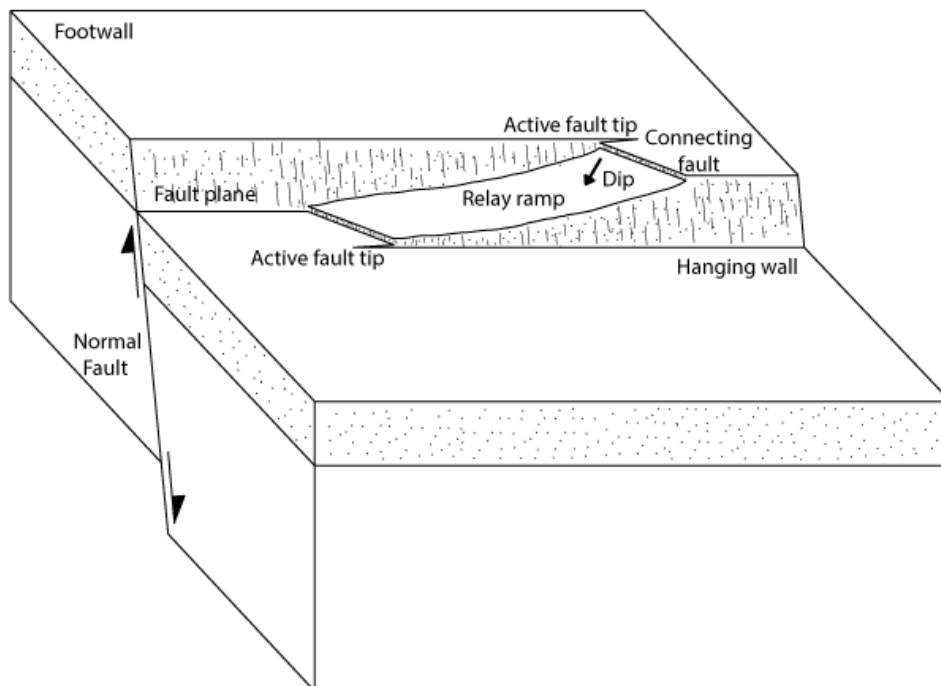
Figure. 2.4: 3D block model of two soft linked normal faults with a connecting relay ramp in between, with all the main features labelled. It visualises the same as fig. 2.5ii. At the next step the ramp will be breached and work as either a fault-bound horst or apparent drag. Redrawn from Peacock and Sanderson (1994).

Typical for isolated unrestricted faults in a displacement profile (d-x plot) is a bell-curve with largest accumulated displacement in the centre, and linearly decreasing displacement towards each fault tip (Fig. 2.3) (Barnett *et al*., 1987; Walsh and Watterson, 1987). If a fault tip is restricted, the displacement profile becomes asymmetric with the highest displacement at the terminated tip (e.g. Muraoka and Kamata, 1983; Nixon *et al*., 2014). Abutting faults exhibit much of the same properties as a restricted fault, except it has one completely locked fault tip where it can accumulate displacement (Nixon *et al*., 2014). The smaller splay faults are splitting of a larger main fault with an acute angle (Granier, 1985; McGrath and Davison, 1995; Davatzes and Aydin, 2003; Perrin *et al*., 2015), and have a displacement profile characterised by largest displacement at the intersection with decreasing displacement towards the tip (Nixon *et al*., 2014).

As two faults interact kinematically, the displacement profiles resemble two asymmetric bell-curves, with the largest displacement towards the relay ramp (Fig. 2.5ii). As the faults progress to become hard-linked, the displacement profile includes two tops close to the intersection, with a pronounced decrease at the breached ramp (Peacock and Sanderson, 1991; Soliva and

Benedicto, 2004). Even though it is worth mentioning that the sum of displacements in the relay ramp, might sum up to the amount of a bell-curve (Fig. 2.5) (Walsh and Watterson, 1987; Peacock and Sanderson, 1991; Cartwright *et al.*, 1995, 1996).
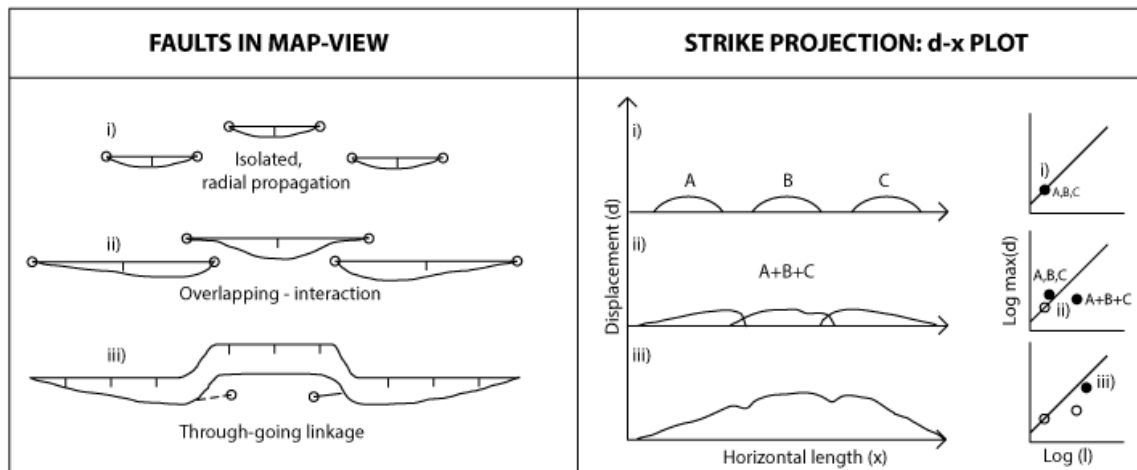
Figure. 2.5: Interaction of three normal faults through time. Displayed in map-view, dx-plot and logarithmic graph plotting maximum displacement against length. **(i)** The faults are isolated and independent of each other. **(ii)** The faults are over lapping and are soft linked with connecting relay ramps. The maximum displacement for each separate fault increase above the projected linear growth, but the fault in total end up below the line. **(iii)** There is a through-going linkage and faults are hard-linked. The dx-plot have almost the same shape as the isolated model. Redrawn from Cartwright *et al.* (1995).

There are two models of fault growth by linkage, isolated fault model (Walsh and Watterson, 1988; Trudgill and Cartwright, 1994; Cartwright *et al.*, 1995; Dawers and Anders, 1995; Cowie, 1998; Cowie *et al.*, 2000; Walsh *et al.*, 2003) and the coherent fault model (Walsh *et al.*, 2002, 2003; Giba *et al.*, 2012) (Fig. 2.6). The isolated fault model consists of numerous fault segments that initiate mechanically and spatially isolated and eventually propagate and link, forming a through going and linked system (Figs. 2.6a and b) (e.g. Trudgill and Cartwright, 1994). In the coherent fault model, the faults initiate as both spatially and mechanically connected fault segments, often at depth (Figs. 2.6c and d), which rapid develop their full trace-length followed by negligible propagation as the segments link (Walsh *et al.*, 2003). Jackson and Rotevatn (2013) indicate that in Suez Rift Egypt, the formation of faults related to second extension phase, form in kinematic coherence to the length of pre-existing faults under soft linkage. The later formed faults, above pre-existing structures formed by the coherent model. While faults with no underlying fabrics developed by the isolated model.

The two models can be distinguished by looking at dx-plots (Figs. 2.6b and d). While the isolated model might have distinguishable displacement highs, the coherent model can end up

with a plot resembling an individual isolated fault (Fig. 2.3iii) (Peacock and Sanderson, 1991; Dawers *et al*., 1993; Cartwright *et al*., 1996). However, newer research has established that once the faults are linked, the displacement can equilibrate with time and variable fault activity (e.g. Giba *et al*., 2012).
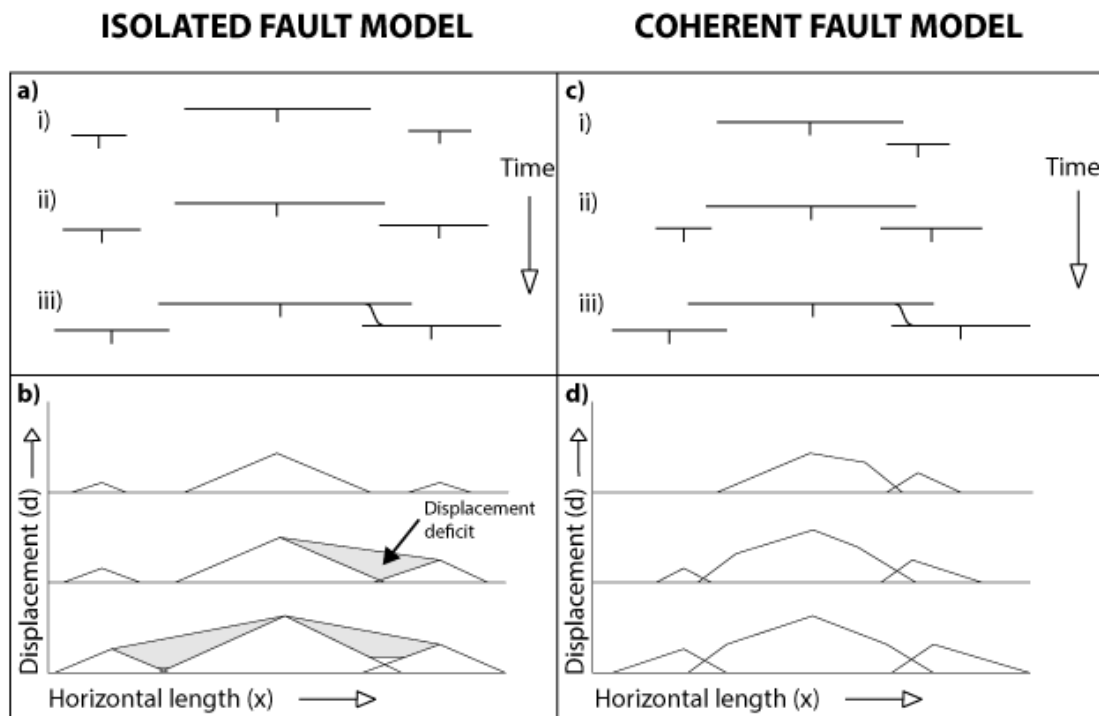
Figure 2.6: Display isolated and coherent fault model in map-view and dx-plot through time. The isolated model starts with isolated independent faults. The coherent model has faults that start soft-linked before later being hard-linked. Modified from Walsh *et al*. (2003).

2.3 Reactivation and influences of pre-existing faults

During multiple deformation events, pre-existing structures and basement faults from earlier phases of deformation can often be reactivated (e.g. Dewey and Burke, 1973; Daly *et al*., 1989; Kim *et al*., 2001; Bailey *et al*., 2005). A reactivated fault is defined as a fault that undergoes a new slip event with displacement after some time of inactivity. And have thereby undergone two or more tectonic events (Sibson, 1985; Holdsworth *et al*., 1997; Peacock, 2002). Pre-existing basement faults are weak zones compared to the surrounding crust (Daly *et al*., 1989; Prucha, 1992; Holdsworth *et al*., 1997; Morley *et al*., 2004). These weakened zones can have higher frictional coefficients and lower cohesion than the surrounding rock (Daly *et al*., 1989; Krantz, 1991; Sibson, 1995), Therefore making them an attractive target for crustal strain, compared to compartmentalisation of strain in new faults (Prucha, 1992; Holdsworth *et al*.,

1997). Additionally, Nixon *et al.* (2014) provide evidence that reactivation of basement structures can occur locally as well as regionally within a fault network.

Most usual is by upward propagation of segments from a pre-existing fault (e.g. Richard and Krantz, 1991; Nicol *et al.*, 2005; Baudon and Cartwright, 2008b). The less usual method is by dip linkage by dip-propagation between a newly formed fault in upper sedimentary cover and a pre-existing fault (e.g. Baudon and Cartwright, 2008b).

Pre-existing faults will have a likelihood of being reactivated if the fault orientation matches the orientation of the newly imposed extensional event (Richard and Krantz, 1991; Bellahsen and Daniel, 2005; Baudon and Cartwright, 2008b). With a small deviation in the extensional direction in the second phase, supra-faults can form with orientation rotation with depth to align with pre-existing faults at depth (e.g. Giba *et al.*, 2012; Nixon *et al.*, 2014). Further, the larger faults have enhanced possibility to be reactivated compared to smaller faults in a fault network (Kelly *et al.*, 1999; Peacock, 2002). Segmentation between pre-existing faults might also interfere with which faults get reactivated, where only a delimited fault segment might be reactivated (Kelly *et al.*, 1999; Baudon and Cartwright, 2008b). The amount of sedimentation might also interfere on reactivation, where a high level of post-rift sedimentation might lock up deeper faults instead of reactivating them. Small amounts of post-rift sedimentation, on the other hand, favours reactivation (Dubois *et al.*, 2002).

Pre-existing normal faults can be reverse-reactivated in an event of compressional forces, which might occur during a basin inversion (Sassi *et al.*, 1993; Sibson, 1995; Kelly *et al.*, 1999). Faults are optimal for reverse reactivation if the stress-direction are oriented perpendicular, and the fault dip is shallow (20-35 degrees'). If the rifted-margin faults are dipping with 60 degrees', they might reactivate as high-angle reverse-faults (Sibson, 1985; Letouzey *et al.*, 1990). An extreme overpressure might occur during a switch from extensional environment to compressional environment, as in basin inversion. This overpressure might be the solution for reactivation instead of formation of new faults with a favoured orientation (Sibson, 1995).

As previously mentioned, a fault network holds several different fault-types with corresponding displacement profiles. However, all these displacement profiles can deviate if they have been reactivated, by increasing/decreasing the displacement and keeping the same length (e.g. Kim *et al.*, 2001; Nixon *et al.*, 2014).

3 Geological setting

3.1 Australian North West Shelf

The study area is located on the Australian North West Shelf (ANWS), which forms part of the passive margin offshore of northwest Australia (Fig. 3.1). ANWS is characterised by four Paleozoic-Cenozoic basins, which together form the majority of the Westralian Superbasin (Bradshaw *et al.*, 1988; Etheridge and O'Brien, 1994; Hocking *et al.*, 1994), including the: Bonaparte Basin, Browse Basin, Roebuck Basin and Northern Carnarvon Basin; from NW to SE respectively (Fig. 3.1a). These basins show a continuous stratigraphy and structure which other basins in the area lack (Teichert, 1939, 1951; Bradshaw *et al.*, 1988; Hocking *et al.*, 1994). Whereas the base of the Westralian superbasin originates from a base of a sequence connected to fragmentation of Gondwana (Bradshaw *et al.*, 1988; Veevers, 1988; Hocking *et al.*, 1994). Furthermore, there are also more fragments underlying the basins, but these areas are poorly known (Veevers, 1988; Hocking *et al.*, 1994).

The ANWS originally formed during the continental break-up of Gondwana in the Devonian (Yeates *et al.*, 1987; O'Brien, 1993; Bailliel *et al.*, 1994; Petkovic *et al.*, 2000). The resulting failed rift in Devonian became overprinted by the major Permo-Carboniferous orthogonal rifting. Resulting in large NE-trending accommodation zones and NE-trending ridges in the Westralian Superbasin (Yeates *et al.*, 1987; Etheridge and O'Brien, 1994; Petkovic *et al.*, 2000). Etheridge and O'Brien suggest that the lithospheric crust beneath present day continental shelf was thinned from 40 km to somewhere between 5 and 20 kilometres.

The extensive extensional event resulted in a following stage with thermal sag in Permian and Triassic, in basin systems along the margin. In this thermal subsidence there was occurrence of reactivation of rift structures and differential uplift with corresponding erosion (Etheridge and O'Brien, 1994; Struckmeyer *et al.*, 1998). However, this event has been questioned about its existence by Chen *et al.* (2002). Simultaneously, a smaller extensional event (bedout movement) occur during a late part of the separation of Gondwanaland in Late Permian to Early Triassic. This extensional event can be found over most parts of southern ANWS as a NW/SE extension (Etheridge and O'Brien, 1994; Symonds *et al.,* 1994; Keep and Moss, 2000).

In Late Triassic, the thermal subsidence terminated due to a compressional event, which caused the development of a regional unconformity (O'Brien, 1993; Etheridge and O'Brien, 1994;

Struckmeyer *et al.*, 1998). Struckmeyer *et al*. (1998) suggest that this event shows similarities to several places where inversion has occurred. The compressional inversion could be due to intraplate stress that emerged due to a lot of active global tectonics at the time. This explanation can be strengthened by presence of the compressional event at the eastern coast of Australia (Struckmeyer *et al.*, 1998). The compressional direction has been interpreted to be roughly N-S for the whole West coast (O'Brien, 1993; Etheridge and O'Brien, 1994; Struckmeyer *et al.*, 1998). Even though the direction of deformation is N-S, the deformation in the separate basins will be individual, as the deformations are strongly affected by deeper laying structures (O'Brien, 1993; Etheridge and O'Brien, 1994; Struckmeyer *et al.*, 1998).

In Late Triassic/Early Jurassic, a new event with extension (Fitzroy movement) occur, it can be visualized as a new unconformity in seismic, eroding down in the Triassic successions (Symonds *et al.,* 1994; Borel and Stampfli, 2002; Kennard *et al.*, 2002; Longley *et al.*, 2002). This Fitzroy movement is linked with the opening of Palaeo-Tethys (Borel and Stampfli, 2002), and acted predominantly as a transpressional event, causing extensional and compressional structures (O'Brien 1993; Etheridge and O'Brien 1994; Symond *et al.,* 1994). After the Fitzroy movement, O'Brien, (1993) argue that a compressional event in Tithonian and Berriasian due to intracratonic stress, have a large play on the architecture of basins along the coast, changing the structural trend from northeast to east-northeast (O'Brien, 1993).

In Late Jurassic to Cenozoic the rifting ceased, with the beginning of seafloor spreading in Argo Abyssal Plain, when "Argoland" separated from northwestern Australia (Veevers *et al.,* 1991; Borel and Stampfli, 2002). Symonds *et al.,* (1994) suggests that the separation was a result of lower crust/upper mantle extension accompanied with regional heating. The resulting thermal subsidence phase together with eustasy and sediment supply, created accommodation space for sediments. Where in addition some areas got uplifted and exposed to erosion (Symonds *et al.,* 1994; Blevin *et al.*, 1997; Struckmeyer *et al.*, 1998). Although being within a regional sag-phase, was there still some degree of fault reactivation present during Late Jurassic and throughout Cretaceous (Struckmeyer *et al.,* 1998).

Miocene to Recent, ANWS basins gets reactivated due to a convergence of the Australian and Eurasian plates in the Paleogene/Neogene, causing Australia to collide with Timor (Bailliel *et al.*, 1994; Struckmeyer *et al.*, 1998; Harrowfield and Keep, 2005). The basin modifications made during the event vary greatly from basin to basin, creating both compressional and extensional features (Struckmeyer *et al.,* 1998; Keep and Moss, 2000; Keep *et al.,* 2002; Keep and Harrowfield, 2007).
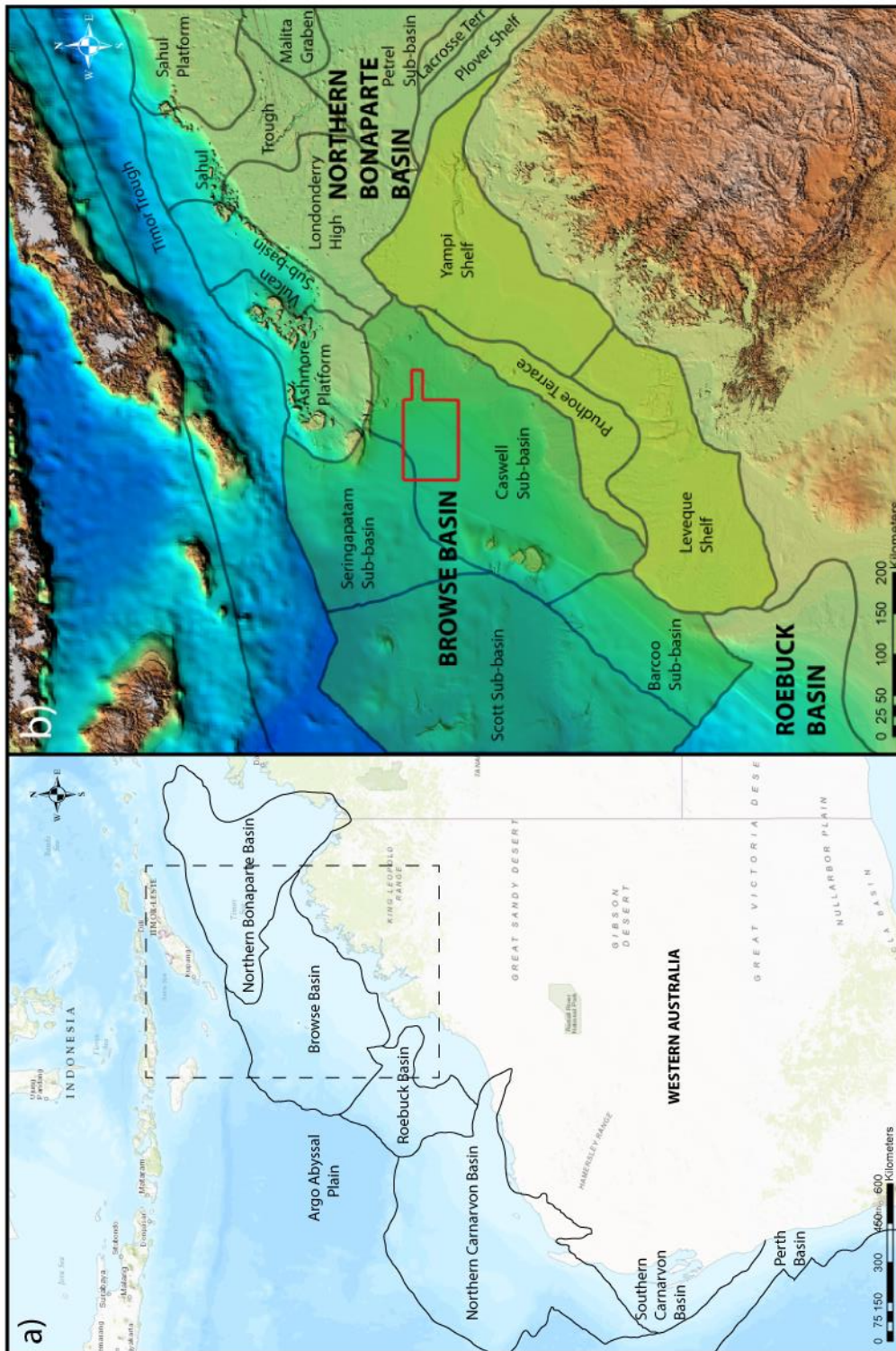
Figure. 3.1: **(a)** Overview map of the Western Australia and the belonging sedimentary basins. Black stippled square represents the position of figure **b**. **(b)** Bathymetry map with a close-up on Browse Basin and the surrounding area. The Sub-basins that make up Browse Basin is marked with green infill, and the belonging elevated parts has a yellowish infill. The interpreted seismic 3D-cube is marked with red lines, and is mainly located in Caswell Sub-basin. Borderlines from Hocking *et al.* (1994) and Keep *et al.* (2007).

3.2 Browse Basin geology

3.2.1 Structural framework

The focus of this study is the Browse Basin in the southern Timor Sea (Fig. 3.1b). The Browse Basin can be sub-divided into Caswell-, Seringapatam-, Scott- and Barcoo Sub-basins (Willis, 1988; Elliott, 1990; Hocking *et al.,* 1994; Longley *et al.,* 2002).

NW-trending basement ridges as the Londonderry Arch and the Dillon Ridge, are part of structures separating Permian to Mesozoic succession in the Browse basin from Bonaparte basin and Vulcan Sub-basin. (Bradshaw *et al.*, 1988; O'Brien, 1993; Etheridge and O'Brien, 1994). Although, the overall boundary separating Browse from Bonaparte is still quite flexible. To the south of Browse basin, the boundary is given by a Jurassic-Cretaceous sequence on the Leveque Shelf, bounded to the west by a shallow basement. Landwards the basin is without an onshore part, which is different compared to the other basins part of the Westralian Superbasin. It is opposed to the stable cratonic Kimberley basin (Bradshaw *et al.*, 1988; Hocking *et al.,* 1994).

Larger Paleozoic faults in the area include NE-trending Caswell-, Brewster- and Bassett Fault (Fig. 3.2) (Struckmeyer *et al.*, 1998; Harrowfield and Keep, 2005). Struckmeyer *et al.* (1998) propose that the Brewster Fault is soft linked to the other two faults by relay ramps.

The Regional tectonism of Browse Basin feature six main deformation phases. Where they can be separated into two repeating cycles. Existing of an (1) extensional event in Late Carboniferous to Early Permian, (2) thermal subsidence in Late Permian to Late Triassic and (3) reactivation in Late Triassic to Early Jurassic. Then a repeating cycle with an (4) extensional event in Early to Middle Jurassic, (5) Thermal subsidence in Callovian to Miocene and (6) Reactivation in Late Middle Miocene to Recent (Blevin *et al.*, 1998; Struckmeyer *et al.*, 1998). Where the first event of extension was the most important, when it comes to development of structures that influenced and controlled the more recent changes (Etheridge and O'Brien, 1994; Struckmeyer *et al*., 1998).
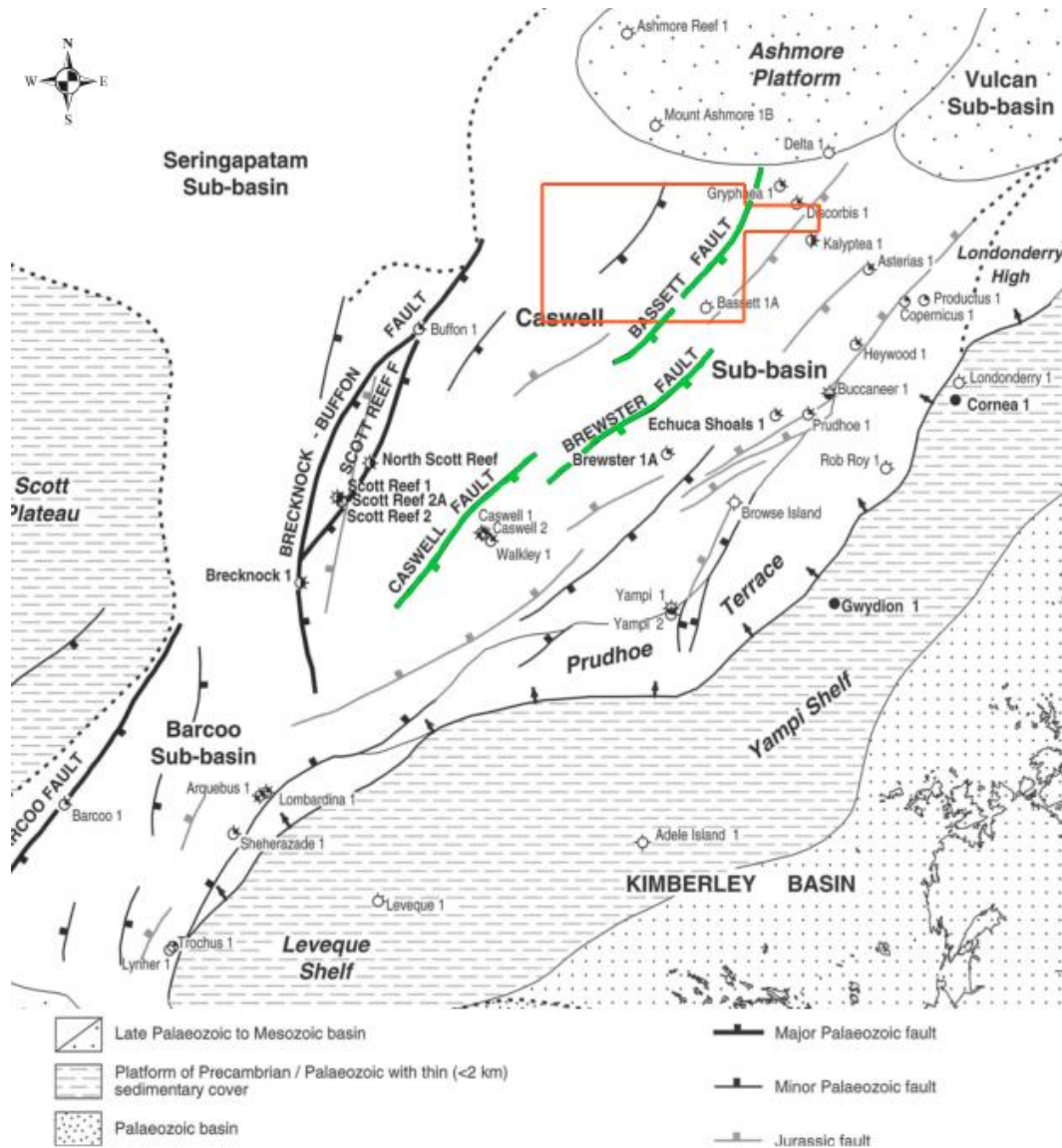
Figure. 3.2: Structural map of the Browse Basin (mainly Caswell Sub-basin). Displaying the larger faults. The seismic cube is outlined in orange. The three larger Paleozoic faults; Caswell, Brewster and Bassett are marked with green. Redrawn from Struckmeyer *et al.* (1998).

1. Carboniferous-Early Permian Extension

At this event, Browse Basin formed as an intracratonic basin with orthogonal extension and a resulting zone of NE-trending normal faults (Bradshaw *et al.*, 1988; Lavering and Pain, 1991; Struckmeyer *et al.*, 1998). Whereas Browse Basin had extension localised in the upper part, did basins north of Browse Basin have extension localised in the lower crust (O'Brien, 1993; Symonds *et al.*, 1994).

2. Late Permian-Late Triassic Thermal Subsidence

The thermal sag phase was a regional event over the ANWS (Etheridge and O'Brien, 1994). In the Browse Basin this phase had reduced tectonic subsidence rates, typical of thermal relaxation after a large rifting event (Struckmeyer *et al.*, 1998). Struckmeyer *et al*., (1998) suggests that the previous extension phase continue into Permian, located in the lower crust.

3. Late Triassic-Early Jurassic Basin Reactivation

This was a major compressional event, possible to correlate with the Fitzroy Movement in Canning- and Bonaparte Basin (Etheridge and O'Brien, 1994). The major faults in the basin controlled the induced reactivation, on the thermal sediments succession and the underlying synrift sediments (Etheridge and O'Brien, 1994; Struckmeyer *et al.*, 1998). This reactivation phase also resulted in several large anticlines and synclines (Willis, 1988; Struckmeyer *et al.*, 1998). With sediment deposition mostly restricted to the deepest synclines in this period (Blevin *et al.*, 1998; Struckmeyer *et al.*, 1998).

4. Jurassic Extension

The stress produced by the Jurassic extension was relieved by the formation of several smaller faults, oriented in half grabens with a trend SW-NE. They often die out within the Triassic unit, with a few of them linking with larger Paleozoic faults underneath. These faults are most present in the northeastern part of Caswell Sub-basin. (O'Brien, 1993; Etheridge and O'Brien, 1994; Blevin *et al.*, 1998; Struckmeyer *et al.*, 1998).

5. Late Jurassic to Miocene Thermal Subsidence

This event is recognised with volcanic activity (Symonds *et al.,* 1994), and erosion on high blocks (Blevin *et al.,* 1997; Struckmeyer *et al.,* 1998). The accommodation in the period was created by localised reactivation, thermal sag, changes in sea level and sediment supply (Blevin *et al.*, 1997; Struckmeyer *et al.*, 1998). Within this episode the tectonic activity was mostly restricted to reactivation of older faults (Blevin *et al.*, 1997, 1998; Struckmeyer *et al.*, 1998). Particularly in the Late Jurassic to Early Cretaceous in response to the end of seafloor spreading in Argo Abyssal Plain. Thus, some fault growth is evident in northern parts of the basin. With Smaller amounts of reactivation proceeding into late Cretaceous, especially in Turonian (Blevin *et al.*, 1997; Struckmeyer *et al.*, 1998).

6. Miocene to Recent Basin Reactivation

The convergence of the Australian and Eurasian plate resulted in anticlinals in Barcoo Sub-basin (Campbell *et al.,* 1984; Struckmeyer *et al.,* 1998; Keep and Moss, 2000; Keep *et al.,*

2000). However, in Caswell Sub-basin the event resulted in small-scale extensional faults. The faulting was more extensive in Caswell Sub-basin than in any of the other Sub-basins inside Browse Basin (Blevin *et al.,* 1997; Struckmeyer *et al.,* 1998). The cause for the extensional faults to form, hold several theories in combination. Including an elastic plate flexure resulting from the low strained oblique collision (Shuster *et al.,* 1998; Keep *et al.,* 2002; Harrowfield *et al.,* 2003; Harrowfield and Keep, 2005; Keep *et al.,* 2007; Keep and Harrowfield, 2008), early orogeny phase with resulting isostatic uplift (Harrowfield *et al.,* 2003; Harrowfield and Keep, 2005; Keep *et al.,* 2007) and thin-skinned gravitational collapse of pre-tectonic sedimentary cover (Harrowfield *et al.,* 2003; Keep *et al.,* 2007; Keep and Harrowfield, 2008).

The event resulted in formation of smaller Miocene extensional faults, ENE- to E-trending, with displacements less than 300 meters (O'Brien *et al.,* 1999a, b). There is some deeper effect with cases of dilational reactivation of Paleozoic faults (Struckmeyer *et al.*, 1998). These Paleozoic faults control the location of the Neogene faulting. Producing faults with the same deformation trend and associated antithetic faults (Keep and Moss, 2000; Keep *et al.,* 2000). The Neogene faults are oriented obliquely above the Paleozoic faults (Struckmeyer *et al.,* 1998; Keep and Harrowfield, 2008). Where in most cases the faults being independent of the deeper laying faults, except some cases of linkage (Struckmeyer *et al.*, 1998; Harrowfield and Keep, 2005).

3.2.2 Stratigraphic framework
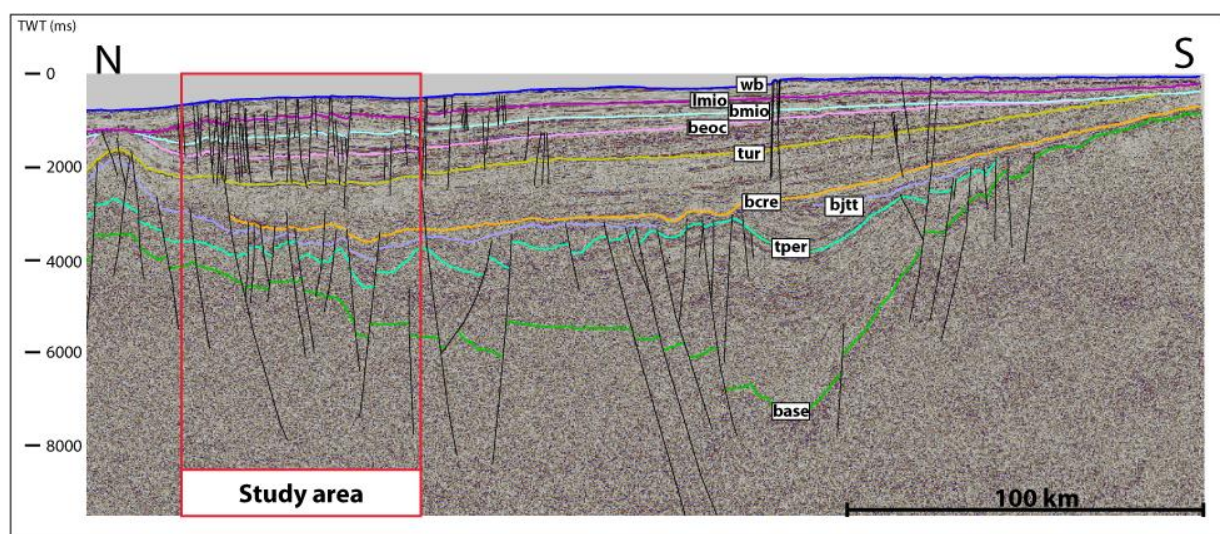
Figure 3.3: Regional 2D-seismic line 130-13, with interpretations. Acronyms: wb= waterbed, lmio= Lower Miocene, bmio= Base Miocene, beoc= Base Eocene, tur= Turonian, bcre= Base Cretaceous, bjtt= Base Jurassic/ Top Triassic, tper= Top Permian, base= Basement. The study area is squared out in red.

19

The Browse Basin contains Paleozoic to Cenozoic sediments forming a succession between 17 and 20 kilometres at its thickest in the Central Caswell Sub-basin (Hocking *et al.,* 1994; Blevin *et al.*, 1997). The oldest sediments are Carboniferous in age, originating from fluvio/deltaic environment, and Permian sediments of marine origin. As seen on figure. 3.3, this interval of deposition can be very thick due to syn-depositional faulting (Blevin *et al*., 1997, 1998). However, in some areas, Permian sediments directly onlap onto Precambrian basement (Stephenson and Cadman, 1994; Blevin *et al.*, 1998). The Early Permian deposits include claystones, siltstones and limestones (Stephenson and Cadman, 1994; Blevin *et al.*, 1998). On top, are the Late Permian Hyland Bay carbonates, (Fig. 3.4) with a major unconformity above, between Permian and Triassic rocks over most parts of the basin following the basin subsidence (Stephenson and Cadman, 1994; Bailey *et al.,* 2005). Overlaying the Permian, are Triassic basal limestones grading upward to an interval with highstand black shales, interbedded with siltstones and volcaniclastics (Stephenson and Cadman 1994; Blevin *et al.,* 1997, 1998).

At the end of Triassic, onset of the Jurassic extension resulted in termination of deposition (O'Brien, 1993; Stephenson and Cadman, 1994), and an accompanying Base Jurassic erosional surface in some areas of Browse Basin (Fig. 3.4) (Blevin *et al.,* 1998). The Early Jurassic successions deposited on top of the erosional surface contain shales interpreted to origin from highstand, marine and prodelta (Stephenson and Cadman, 1994; Blevin *et al.*, 1998). With overlaying Sedimentary deposits originating from fluvio/deltaic systems covering most parts of the basin, which were deposited in inversion synclines and extensional grabens (Blevin *et al.*, 1997, 1998).

The Upper Jurassic successions consist of a supersequence with amalgamated transgressive-regressive sequences, above a protruding unconformity. Above, the Base Cretaceous has eroded down into the Jurassic highstand facies (Fig. 3.4), creating a well-displayed reflector. Hence, evidence of quite large changes in facies with a large sea-level fall. Base Cretaceous lies as an unconformity at most places in the basin, except from some of the deeper basin parts where it might be comfortable (Blevin *et al.,* 1998). In Valangian there was a tectonically enhanced sea-level fall, followed by a sea-level rise with resulting high sea-level in the basin. The sea-level peaked and dropped down in Turonian, and formed an significant erosional contact (Fig. 3.4) (Blevin *et al.*, 1997, 1998). From Valangian to Late Cretaceous the sedimentary facies were mostly low stand slope fans, distal turbidites and transgressive shoreface shelf sands, deposited in a depositional area formed like a westward dipping ramp (Blevin *et al.*, 1998).

In the Early Paleogene to Oligocene, the sedimentary sequence comprises mostly of quartzose sand with origin from fluvial, shoreline and delta deposits. From Late Oligocene to Middle Miocene there is mostly homogenous sand from an outbuilding shelf (Blevin *et al.,* 1997). Beforehand Middle Miocene, the collision between Timor and Australia commences in the Early Miocene (Keep *et al.,* 2002). Subsequently in Mid Miocene, the collision creates a major structural event producing a tectonically-controlled unconformity (Blevin *et al.,* 1997; Keep *et al.,* 2002). Finally during the Mid to Late Miocene, a major flooding event resulted in the deposition of marine carbonates and reef facies (Blevin *et al.*, 1997). Since the Miocene, has the Browse Basin experienced mostly marine conditions, except a short period during glacial maxima in Pleistocene (Stephenson and Cadman, 1994). In addition, during the Miocene reactivation, there is also some evidence of salt withdrawal structures in the northernmost of Caswell Sub-basin (Blevin *et al.*, 1997).

To conclude, the major stratigraphic divisions and seismic horizons marking key basin formation events, includes the:

1. ***The basement horizon (base)*** – the lowermost horizon that represents the top of pre-Cambrian crystalline basement (Willis, 1988; Etheridge and O'brien, 1994).

2. ***Top Permian horizon (tper)*** - which is a representative horizon after the Extension Phase 1 event. (Etheridge and O'brien, 1994; Struckmeyer *et al.,* 1998).

3. ***Base Jurassic horizon (bjtt)*** - an unconformity following intrarift Triassic deposits, and marking the onset of Jurassic Extension Phase 2 (O'Brien, 1993; Etheridge and O'Brien, 1994; Blevin *et al.*, 1998; Struckmeyer *et al.*, 1998).

4. ***Base Cretaceous horizon (bcre)-*** an unconformity resulting from marine regression in the beginning of the last thermal sag phase following the Jurassic extension (Blevin *et al.*, 1997, 1998).

5. ***Turonian seismic horizon (tur)*** - an unconformity resulting from marine regression in the middle part of the last thermal sag phase (Blevin *et al.*, 1997, 1998).

6. ***Base Miocene horizon (bmio)*** - mark the start of the last and ongoing inversion/reactivation (Keep *et al.,* 2002).

In this study the focus is placed to the Base Jurassic horizon and the Base Miocene horizon, holding two separate fault populations. The Base Jurassic horizon with faulting as a result from extensional phase 2, and the Base Miocene horizon with faulting as a result from the Neogene reactivation.
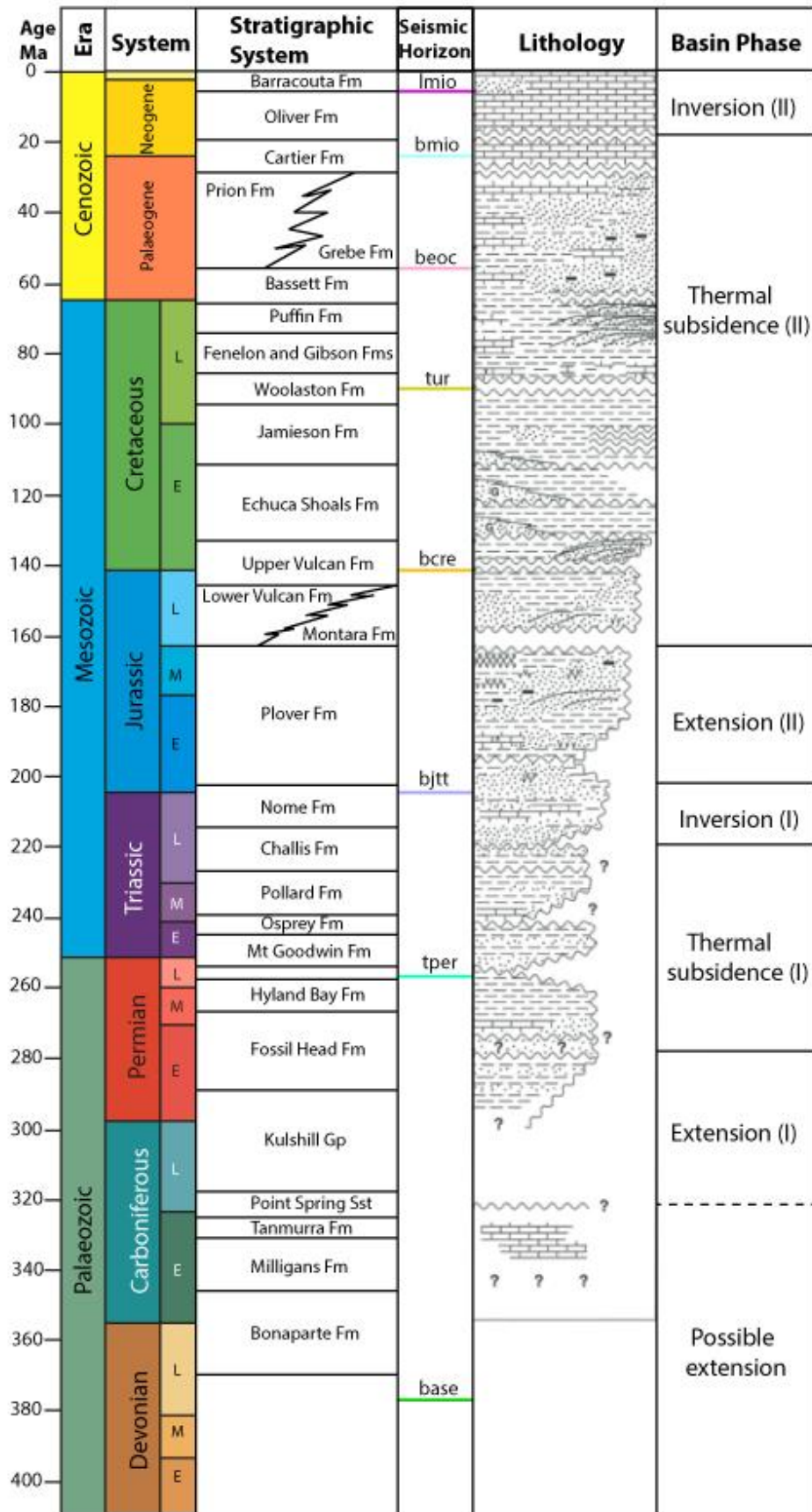
Figure. 3.4: The Browse Basin sediment sequence stratigraphy with stratigraphic systems, interpreted horizons, lithology and basin phases. Modified from Blevin *et al*. (1998)

4 Data and methods

4.1 Seismic data

A number of seismic reflection datasets, both 2-D and 3-D, were integrated and used to interpret the structure and stratigraphy of an area in the northern Browse Basin (Table 4.1). The primary dataset used was the North Browse TQ3D 3-D seismic reflection data, acquired by the *M/V Geco-Beta* using a dual source airgun array in 1998 and 1999. The data are 52-fold containing frequencies between 3 and 180 Hz and cover an offshore area of ~6250 km^2 in the northern Caswell Sub-Basin. The 3-D migrated volume comprises inlines bearing N270˚E and cross-lines bearing N000˚E, with line spacings of 18.75 m and 12.5 m, respectively. In addition, the 3-D seismic volume was integrated with 2-D seismic reflection lines collected by the *RV Rig Seismic* during several campaigns by the Australian Geological Survey Organisation (AGSO), including the Browse Basin High-Resolution survey (AGSO Survey 175; 1996) and the Browse Basin survey (AGSO Survey 119 and 130; 1993 and 1994) (Figs. 4.1 and 4.2).
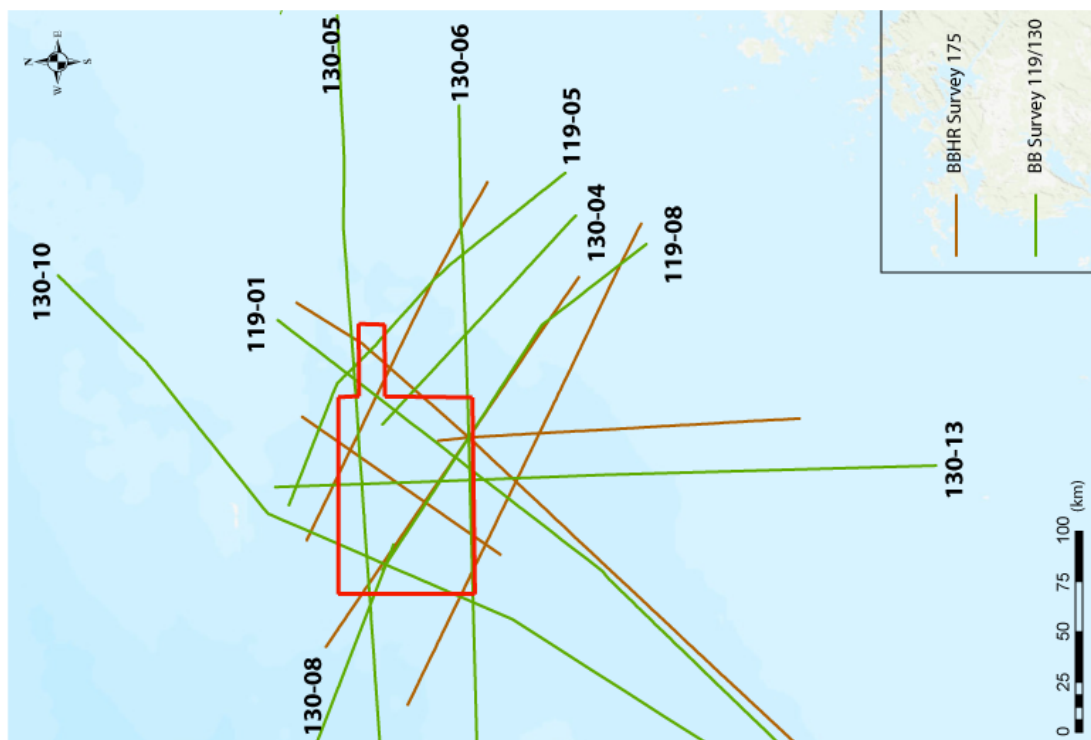
Figure. 4.1: Area marked with red represent the North Browse TQ 3D seismic. Brown lines represent BBHR 2D-seismic lines and green lines represent the BBS 2D-lines, which cross through the 3D seismic. The BBS-lines are labelled with the belonging names.

The 2-D seismic reflection data were used to help correlate and map existing regional horizon interpretations throughout the 3-D seismic volume. Furthermore, the AGSO 2D seismic reaches a depth of -16000 ms (TWT), while the TQ3D 3-D seismic go down to -7000 ms (TWT). For that reason, the regional 2D-seismic provide better constraints on some of the deeper structures. The seismic data in this survey have not been depth converted, therefore are all seismic data, cross-sections, horizon surfaces and time-thickness maps are presented with their vertical axis in two-way time (TWT).

Survey	Seismic	Vessel + (year)	Depth TWT	Source	Publications
BBHR	2-D	R/V Rig Seismic (1996)	5.5 s	Airgun	Blevin *et al*., 1997, 1998; Struckmeyer *et al*., 1998
BBS	2-D	R/V Rig Seismic (1993-94)	16 s	Airgun	Symonds *et al*., 1994
North Browse-TQ3D	3-D	M-V Geco-Beta (1998-99)	7 s	Airgun	Belde *et al*., 2015

Table 4.1: Details of the seismic reflection datasets used in the survey.
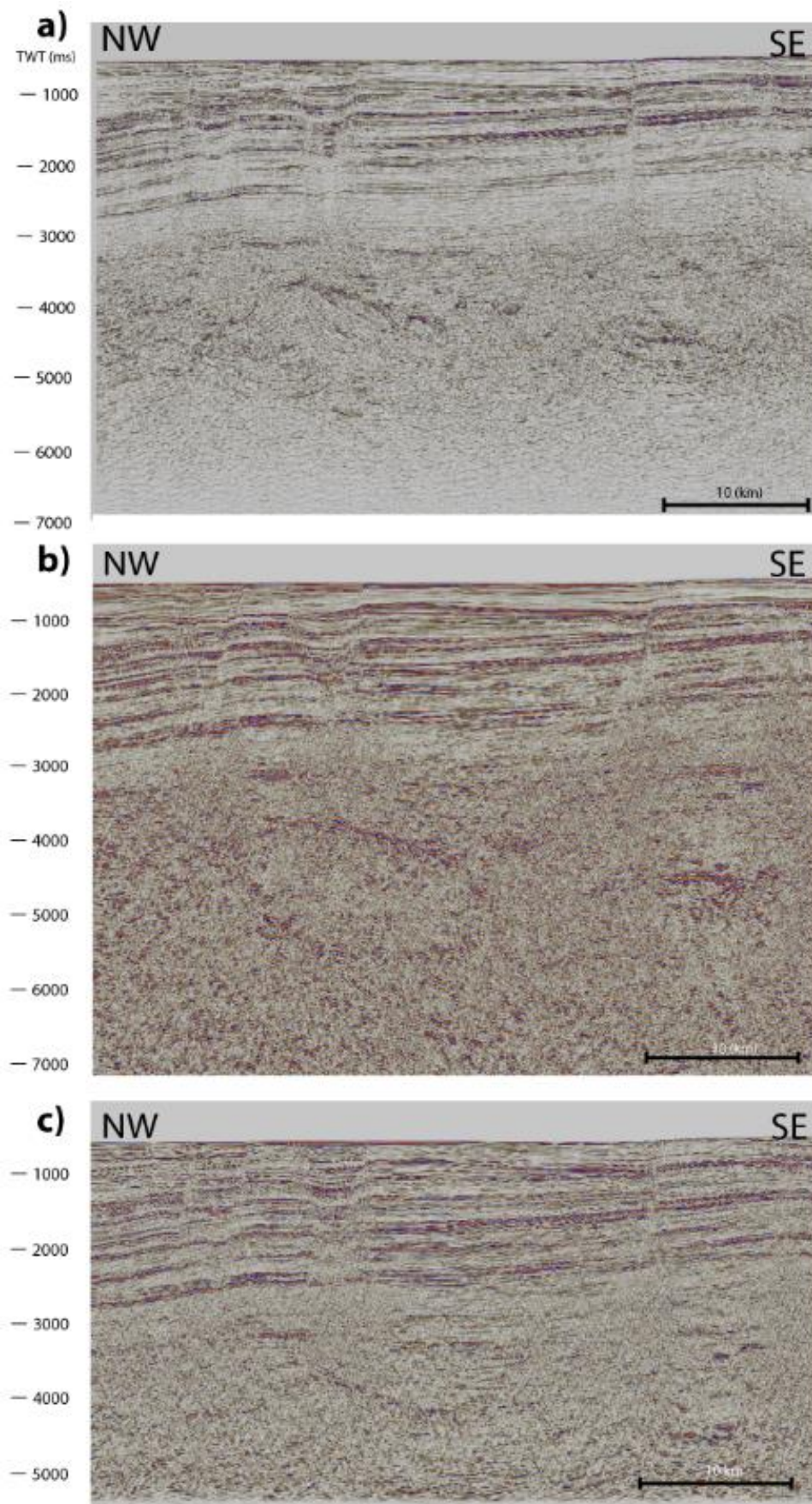
Figure. 4.2: Seismic lines from the three different surveys at approximately the same location, with orientation NW-SE. **(a)** TQ3D arbitrary line. **(b)** BBS-line 119-08. **(c)** BBHR-line 11 (located on top of 119-08 in fig. 3.1).

25
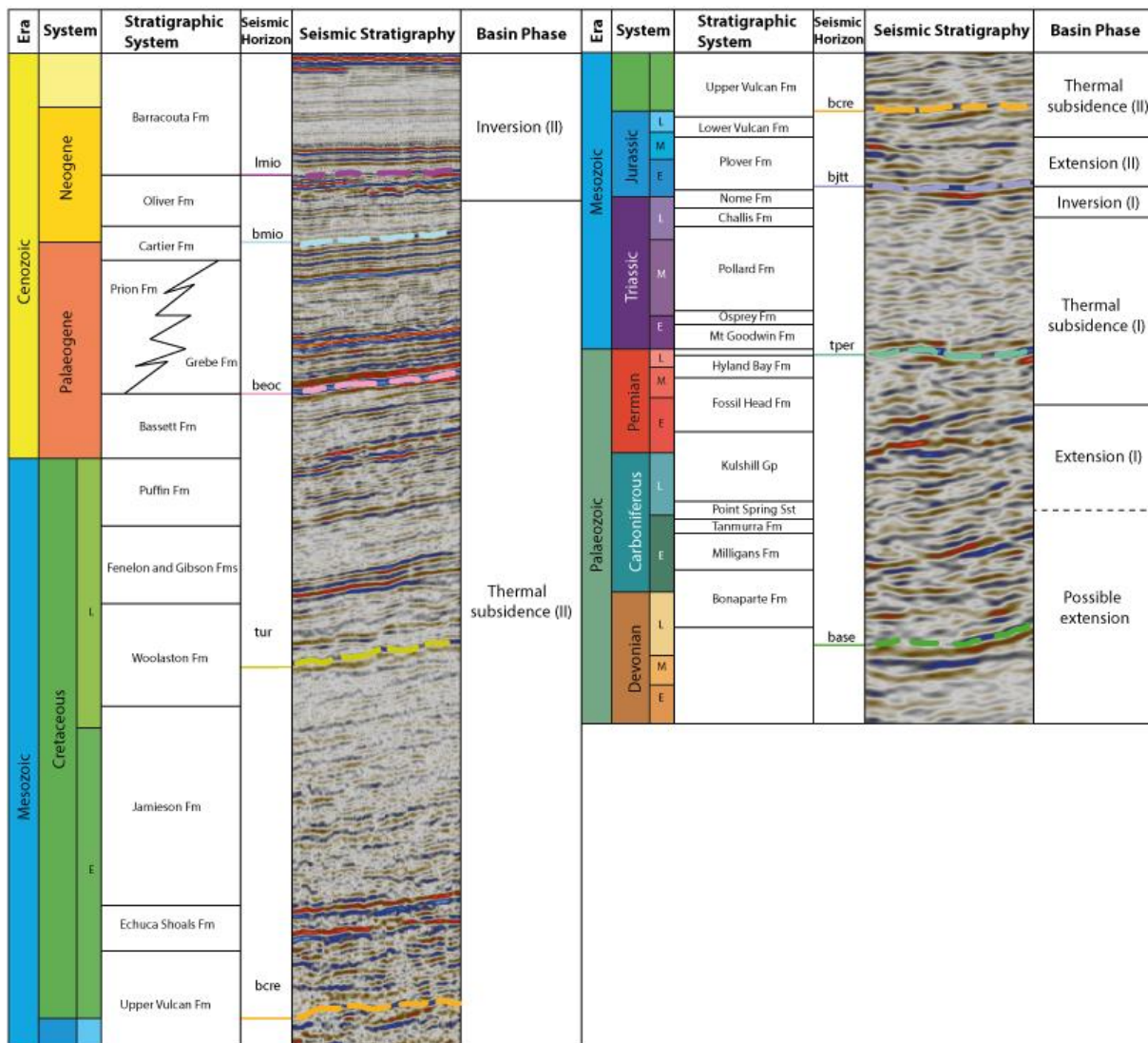
Figure 4.3: Seismic stratigraphy column including stratigraphic system, seismic horizons and basin phase. All columns are modified to fit the original seismic column, to display sediment thickness of every period. Modified figure from Blevin *et al*. (1998).

4.2 Seismic interpretation

The seismic interpretation was done using Petrel, a seismic interpretation and modelling software developed by Schlumberger. Several horizons were interpreted with the help of ties to the regional 2D seismic data (Fig. 4.4). These interpreted regional 2D-lines are striking through the volume at different locations and variating orientations (Fig. 4.1), which provide a good basis for the interpretation. By interpreting inlines and crosslines in combination with arbitrary lines throughout the volume, creates a raw horizon interpretation grid (See Appendix A for process).

Horizons above Turonian were interpreted on every 128th inline/crossline, and every 64th (800 meters) crossline in faulted areas. While for horizons below Turonian, interpretation was done on every 16th to 64th inline, while crosslines was interpreted with a variety of every 64th to every 256th crossline. Furthermore, horizons were interpreted on several arbitrary lines oriented perpendicular to the orientation of the pre-existing faults.
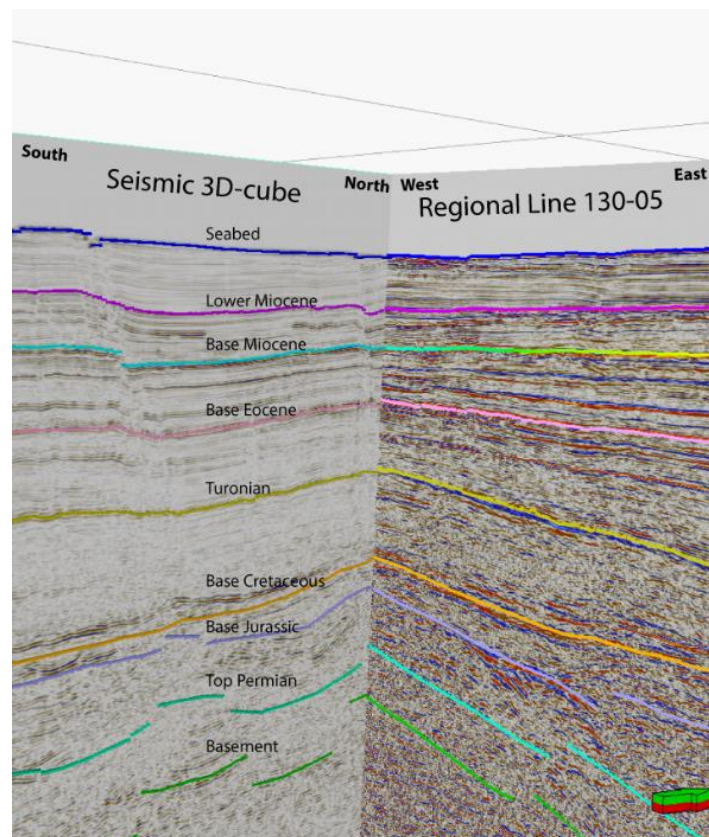
Figure. 4.4: Displaying the correlation of seismic horizons at an intersection between an x-line in the 3D-cube and the regional line 130-05 (Fig. 4.1). Lines with approximately same colour represent the same horizon.

The interpreted horizons are listed in the figure in stratigraphic order in fig. 4.5, with the corresponding reflector qualities. The three horizons within the Cenozoic (Lower Miocene, Base Miocene and Base Eocene) do all follow coherent reflectors with high negative amplitude reflectors. That occurs in reflector packages, which are well displayed with RMS amplitude attribute (Fig. 4.6e) and Envelope attribute (Fig. 4.6f). Below the Cenozoic section, the reflectors occur as single reflectors rather than reflector packages. With a medium to high amplitude, continuous reflector Turonian unconformity. For horizons below Turonian, the reflectors are more chaotic, with a decrease in lateral continuity and reflector amplitude with depth. The Base Cretaceous follow a continuous reflector with medium to high amplitude, which is truncated in the northernmost part by the Valangian Unconformity. Deeper down, Base

Jurassic has a medium amplitude reflector with variations in continuity. The reflector package can be traced over the entire study area. Further down, Top Permian and the basement have discontinuous reflectors with low to medium amplitude. For such reflectors with discontinuity and low amplitudes, aid was found in the use of the structural smoothing attribute (Fig. 4.6b) and the envelope attribute (Fig. 4.6f).

Reflector/age	Phase	Characteristics	Example
Seabed	Positive amplitude (peak)	High amplitude, continous	
Late Miocene	Negative amplitude (trough)	High amplitude, continous	
Base Miocene	Negative amplitude (trough)	High amplitude, continous	
Base Eocene	Negative amplitude (trough)	High amplitude, continous	
Turonian	Negative amplitude (trough)	Medium to high amplitude, continous	
Base cretaceous	Negative amplitude (trough)	Medium to high amplitude, various continouity	
Base Jurassic	Negative amplitude (trough)	Medium amplitude, various continouity	
Top Permian	Negative amplitude (trough)	Low to medium amplitude, discontinous	
Basement	Negative amplitude (trough)	Low amplitude, discontinous	
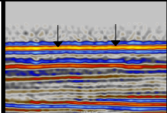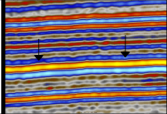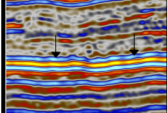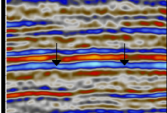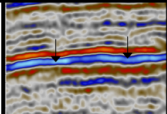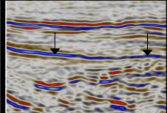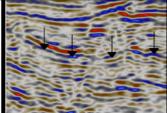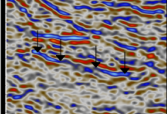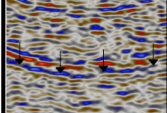
Figure. 4.5: Reflector description for the interpreted horizons.

Faults in the upper section were interpreted on arbitrary lines and every 64th crossline. As well as on seismic variance/coherency time slices that allowed connection of faults in map view and helped correlate fault sticks of individual faults between arbitrary lines and crosslines. This upper section has a seismic resolution of faults exhibiting throws greater than 10 meters. Below

the Turonian horizon, faults were interpreted on several arbitrary lines oriented perpendicular on fault strike, and every 128th crossline. At this depth, it is more difficult to interpret due to less seismic resolution. They were mapped with the help of filters as well as volume attributes and adjustments to the belonging parameters (Filters: Black/grey/white and Red/white/black. Volume attributes: Structural smoothing, RMS amplitude, Envelope and Variance (Edge method)) (Figs. 4.6 and 4.7). The seismic resolution for fault detection at this depth are faults exhibiting a greater throw than 70 meters.
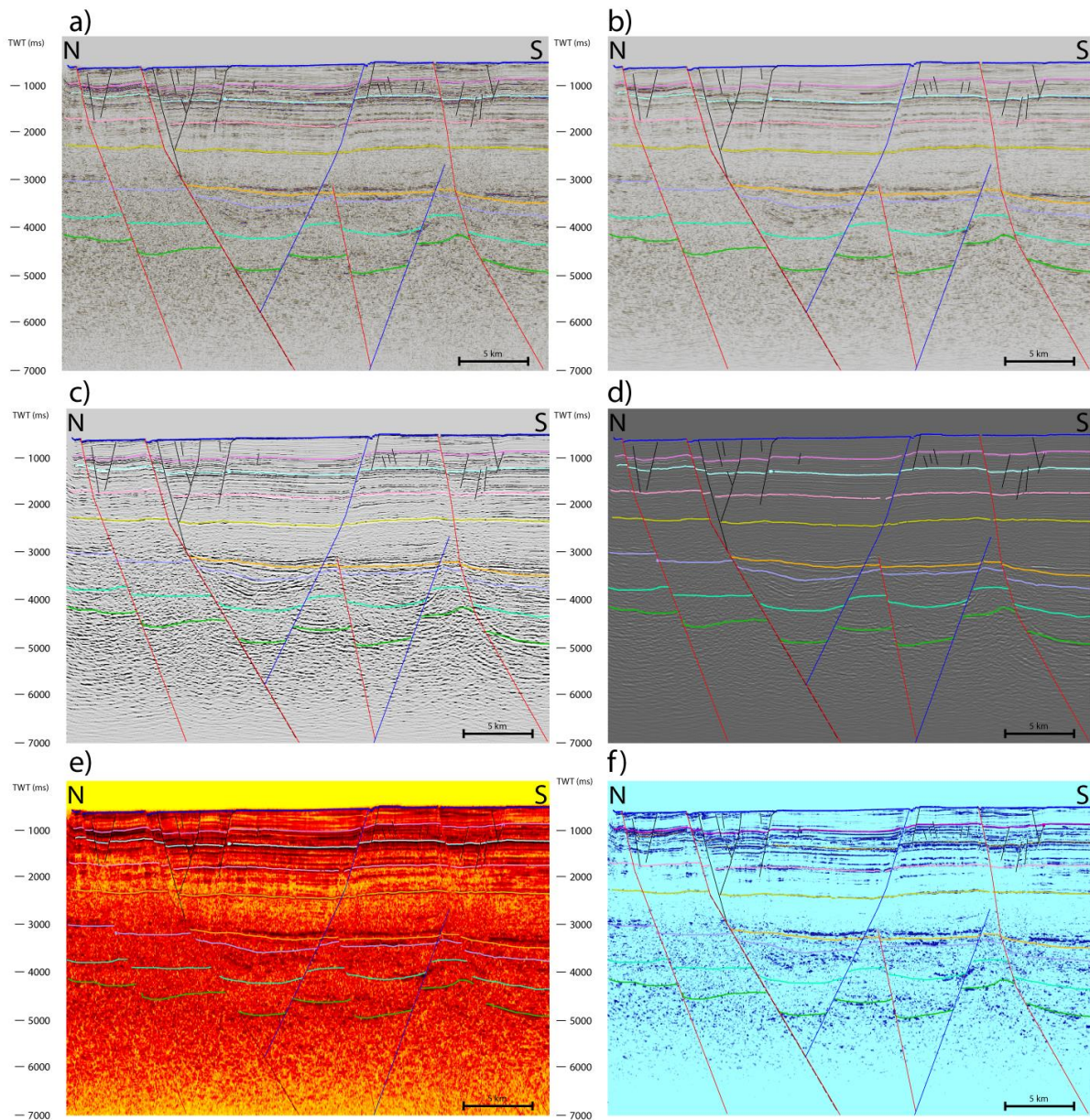
Figure 4.6: Interpreted seismic with applied filters and attributes. See Fig. 5.4 for horizon description. **(a)** Original realized seismic. **(b)** Structural smoothing. **(c)** Structural smoothing with black/grey/white filter. **(d)** Structural smoothing with red/white/black filter. **(e)** RMS Amplitude attribute. **(f)** Envelope attribute.
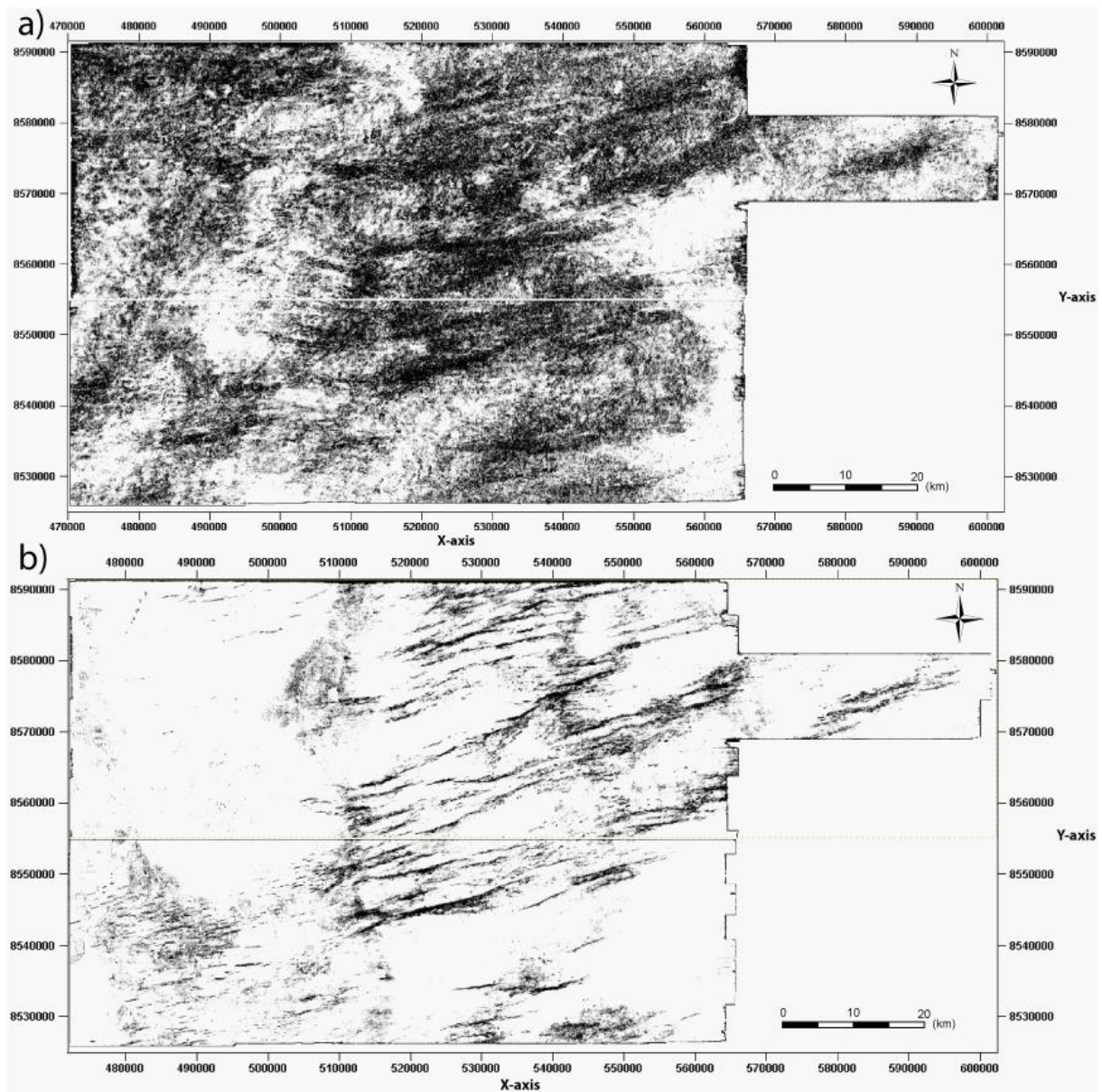
Figure 4.7: Variance attributes on time slice, the darker areas are where seismic reflectors are cut or interrupted. **(a)** Variance map from – 3000 ms TWT, which in average corresponds to a level just above the Base Cretaceous horizon. Some of the darker areas form lines that fit well to faults visible in the interpretation window. **(b)** Variance map from -1400 ms TWT, which in corresponds to a level just above/below the Base Miocene horizon. Faults are well defined as thin black lines.

4.3 Fault modelling

Two 3-D fault models were created in Petrel (see Appendix B for the process), one for the upper part (seabed – Base Eocene) and one for the lower part (Turonian – basement). The faults within these two intervals were made into a pillar grid, with pillars spaced with 500 meters and geometry as vertical, linear, listric or 5 point. The fault planes are connected in 3D-based spatial proximity. Furthermore, are the fault planes cut by the top and bottom horizons, which in this

analysis are seabed and Base Eocene for fault model 1 and Turonian and basement for fault model 2. Next step is Pillar gridding where three skeletons (lower, middle and upper) are created to the faults. When the pillar gridding is done, horizons can be incorporated into the model. When applying the horizons, cut-off values for hanging- and footwall can be set. The values can be set differently for the different horizons and for each of the faults.

The two chosen horizons for fault analysis are Base Miocene and Base Jurassic. Base Miocene was chosen because it is located at the position where the Neogene faulting have accumulated highest throw values. Base Jurassic was chosen because it has the best traceable reflector of the horizons that are faulted by all the interpreted pre-existing faults. For the ability to calculate attributes such as throw and dip direction, cut-offs were integrated on hang/foot-wall. For the Base Miocene horizon cut-off values were set to 100 meters on either side of the fault plane, because of no fault growth. Whereas for Base Jurassic the fault growth is present, so the cut off values was set to 1000 meters in the hanging wall and 500 meters in the footwall. With completed fault models, the next step was to extract throw data for all faults on the two horizons. With the throw data comes (x, y, z) coordinates and fault number for numerous calculated points along the fault/horizon interference. The throw data gets converted to meters by incorporating interval velocities, 4.550 km/s for Base Jurassic and 3.550 km/s for Base Miocene. These velocities were collected from Struckmeyer *et al*. (1998). They gathered them by using MacRay[tm], an interactive software package that allows raypaths and travel times to be calculated and compared with actual travel times. The model was later constrained by gravity modelling, and by integration with seismic reflection data and onshore geology (Struckmeyer *et al*., 1998).

4.4 Quantitative fault analysis

4.4.1 Fault activity

Active normal faults create accommodation space for sediments above the hanging wall. The activity of faults will therefore strongly influence sediment thickness through time (Dawers and Underhill, 2000). Sediment thickness maps give a great understanding of the deformation history, by indicating time periods when faults were active. (Rouby *et al*., 2002). Syn-deposition faulting creates thickening sediment packages towards active fault planes. On the contrary, post-deposition faulting creates thinning or constant thickness on sediment packages towards

the fault plane (Ocamb, 1961; Dawers and Underhill, 2000). For the reason to investigate depocentre development and the distribution of sediments through time, time-thickness maps were generated showing true vertical thickness in time between two seismic horizons. This was done for four different stratigraphic intervals to determine syn-sedimentary fault growth and activity of major faults during different deformation phases.

4.4.2 Fault network mapping

After the fault modelling, the faults contain values of location and throw at several points along the intersection of the fault and horizon. These values can be exported to a format readable by Microsoft Excel. Fault data for each of the faults must be opened separately and merged into one big file for the Base Miocene faulting and one for the Base Jurassic faulting.

These two excel files were then opened in ArcGIS, where the data was opened as point data. Implied segments in between the points and calculated an average throw value from both end points on the segments. This makes it possible to show the point data as fault maps, weighted by different attributes (throw, dip-direction, group).

4.4.3 Orientation and Throw Analysis

Traditional methods in fault and network analysis include the usage of fault segment orientation, length, displacement and spacing. These methods allow you to characterise and investigate scaling, geometries, kinematics and interactions. I´ve displayed the information if seven ways:

1) Weighted Rose Diagrams – Orientation rose diagrams was created by a module in ArcGIS, which calculates length weighted and throw weighted orientations diagrams.

2) Frequency-size distributions – Strain analysis of the fault population by either the fault length or the fault throw. The population can fit either a power law distribution, log normal SD (standard deviation), normal SD, negative exponential or a cumulative curve. The best-fitted plot is chosen based on which plot that have points resembling a straight line (Meyer *et al*., 2002).

3) Max throw vs. length plots – Logarithmic plots with fault length plotted against the maximum throw, gives an indication of the ratio between the two. Illustrates the trend between the two for the whole population if any are present. If it follows a trend, a plotted line will go through the points perfectly.

4) Throw vs. length plots – The throw-length plots was made in a combination of ArcGIS and excel, for fault data at the Base Miocene and Base Jurassic horizon. The throw-length plots created for single faults was made by plotting throw values for each segment against half the segment length. Adding this length for each plotted point along the fault, before normalising all the values by dividing all the throw values on the maximum throw and the length values along the fault on the total fault length. By normalising the throw-length plots, the faults are applicable for comparison regardless of fault size.

The cumulative throw-length plots for the groups was calculated in ArcGIS, both by using a module and manually. Sampled throw values along lines reaching all faults inside the group. The lines were spaced by 1000-meters with an orientation N-S (approximately perpendicular to the strike). The calculation was then moved to Excel for graph management.

5) Throw vs. depth profiles – The throw-depth plots was conducted manual, by collecting time difference with depth (ms TWT) between footwall and hanging wall, for each consecutive interpreted horizon along the fault plane. The time difference is further converted to meters by applying the corresponding velocity in the respective layer. Further, creating the profile by plotting the resulting throw values in meters against the depth (in ms TWT) at footwall horizons.

6) Density Plot - For the density plot, the Kernel Density plot in ArcGIS was used. Kernel line analysis is a non-parametric statistical method to calculate the magnitude per unit area from polylines. Its inputs of interest are at what search radius to calculate density and output cell size for the raster dataset. The Search radius was set to 3 km, and the output cell size was set to 100 m^3.

7) Spatial Heterogeneity Analysis - Cumulative plots of frequency and throw along line transects can be used to calculate the spatial heterogeneity of faulting and strain. Cumulative values are plotted against the distance along the transect line at each sampled fault. Where a steep gradient suggests a rapid increase in throw or frequency, and a gentle gradient suggests the opposite (Fig. 4.8) (Putz-Perrier and Sanderson 2008a, b).

The cumulative distributions are compared against a uniform distribution line to calculate the heterogeneity. The heterogeneity parameter is given by this equation:

$$V = |D^+| + |D^-|$$

Where the parameters D^+ is the largest deviation above and D^- is the largest deviation below the uniform distribution. To get the cumulative frequency and throw over different lengths the

quantity V must be normalised, which is done by dividing it by the cumulative total. This results in a V-value between 0 and 1, where 0 represents a homogenous distribution and 1 indicates a heterogeneous distribution (Putz-Perrier and Sanderson, 2008a, b).
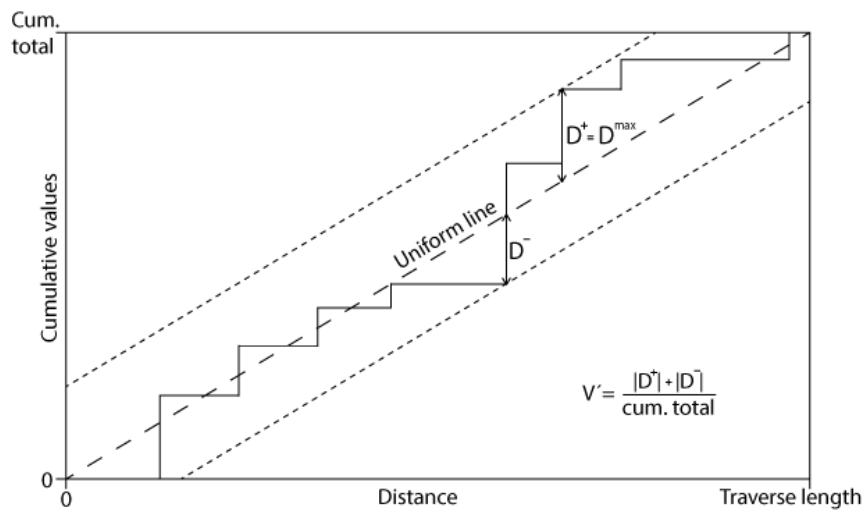
Figure 4.8: Illustration of a cumulative plot, including the uniform line, $|D^+|$ and $|D^-|$. As well as the formula for V´. Redrawn from Putz-perrier and Sanderson, (2008b)

34

5 Results – Primary structures and thickness characteristics

This chapter describes and displays the interpreted horizons and major rift faults, with the use of a series of cross-sections, horizon maps and time-thickness maps, to constrain the fault activity for the study area. The focus has been towards the major deeper rift faults, mainly located below the Base Cretaceous horizon, although some do continue and offset Turonian and Miocene horizons (Fig. Cross-Sections).

5.1 Main rift faults and basement structure

The basement horizon shows an overall shallowing trend to the N at structural highs varying from -4400 ms TWT to less than -4200 ms TWT. More detailed it indicates a profound structural grain orientated WSW-ENE, forming graben and horst complexes. These are bound by major rift faults that are regularly spaced at ~5 km (Fig. 5.1), dipping approximately to the N (MF3, 6, 9, 10, 11, 13, 14, 15 and 16) and S (MF1, 2, 4, 5, 7, 8 and 12). These major rift faults set up the highest basement elevations (-4000 ms TWT), located in their footwalls, as well as structural lows down to -5400 ms TWT. An exception from the larger graben/horst complex, are the closely spaced graben between MF8 and MF9 in the easternmost part. Two large depocentres stand out, one in the centre between MF7 and MF10/MF11, and another to the south in the hanging wall of MF12.

The Top Permian horizon (Fig. 5.2a) has the shallowest areas at footwalls in the northeast (-3400 ms TWT), and deepest point in structural lows in the south (-4800 ms TWT). This horizon has an expression similar to the basement horizon, with major structures congruent to the (basement) horst and graben complexes.

The highest elevation of the Base Jurassic horizon is located in the northeast corner of the study area (-2800 ms TWT) (Fig. 5.2b), and the horizon exhibits an overall deepening trend towards the southwest (down to -4200 ms TWT). The southwest part of the study area comprises continuous depressed areas, which are located in footwalls and are found crossing through faults. However, the major faults are still visible and exhibit large enough displacement to shape the architecture of the horizon. Meanwhile, the larger faults have an apparent trend of clockwise fault strike rotation, ranging from the eastern part of the horizon, to the western part of the

horizon. Furthermore, there are no faults developed with the same magnitude as the major faults offsetting this horizon.
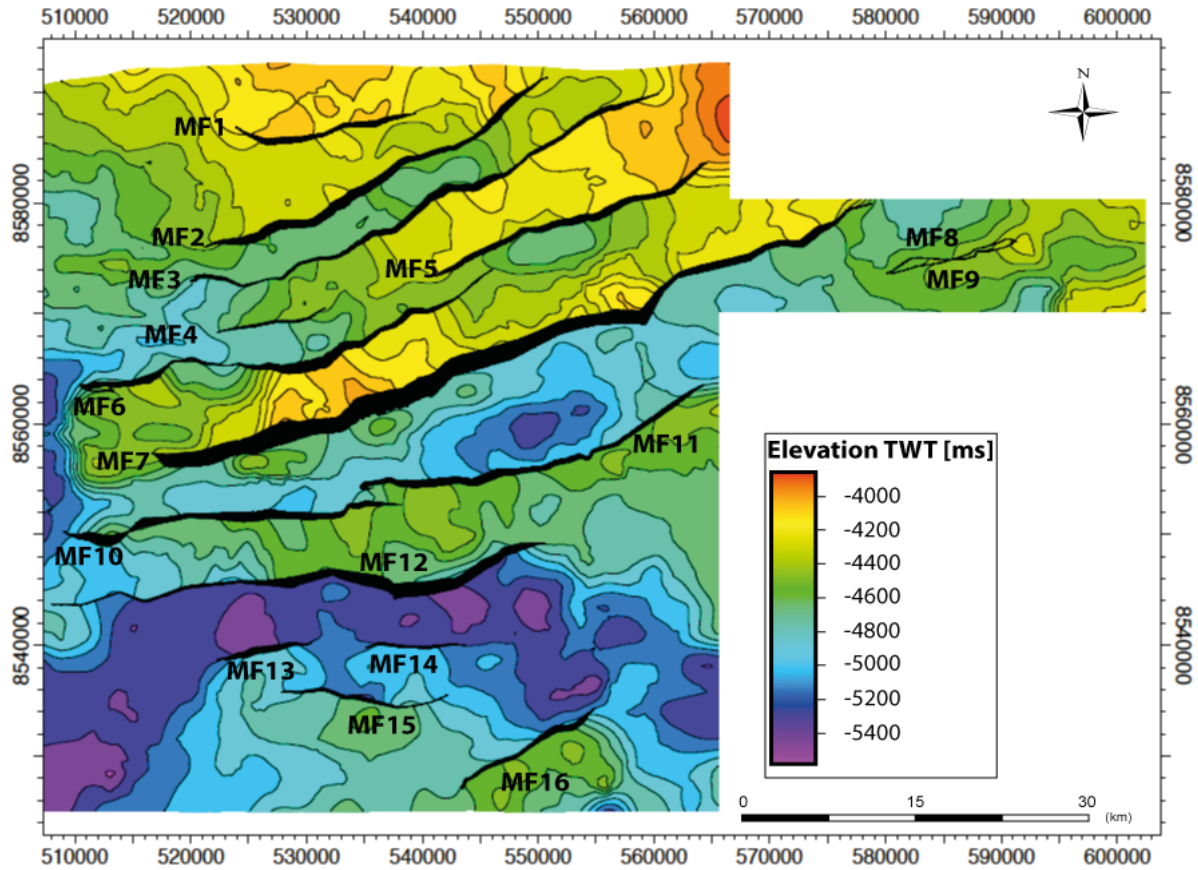
Figure. 5.1: Basement horizon colour coded based on elevation values (ms TWT). The major rift faults are cut out in black and labelled with acronyms MF(1-16).

The Base Cretaceous horizon has a continuous low elevated area at -3800 ms TWT, from northwest down to southeast. In the southern parts of the depressed area, only smaller parts of the hanging walls of major faults are under structural control. The Base Cretaceous horizon is the uppermost of the interpreted horizons, where the largest major rift faults still show presence as whole fault lengths (Fig. 5.2c). These do exhibit some structural control on the eastern part, while the western part is sub-horizontal, except a structural high in the centre to the south. Especially MF6 and MF7 in the centre of the horizon exhibit pronounced displacement, that together form a 1-2 kilometre thick horst.
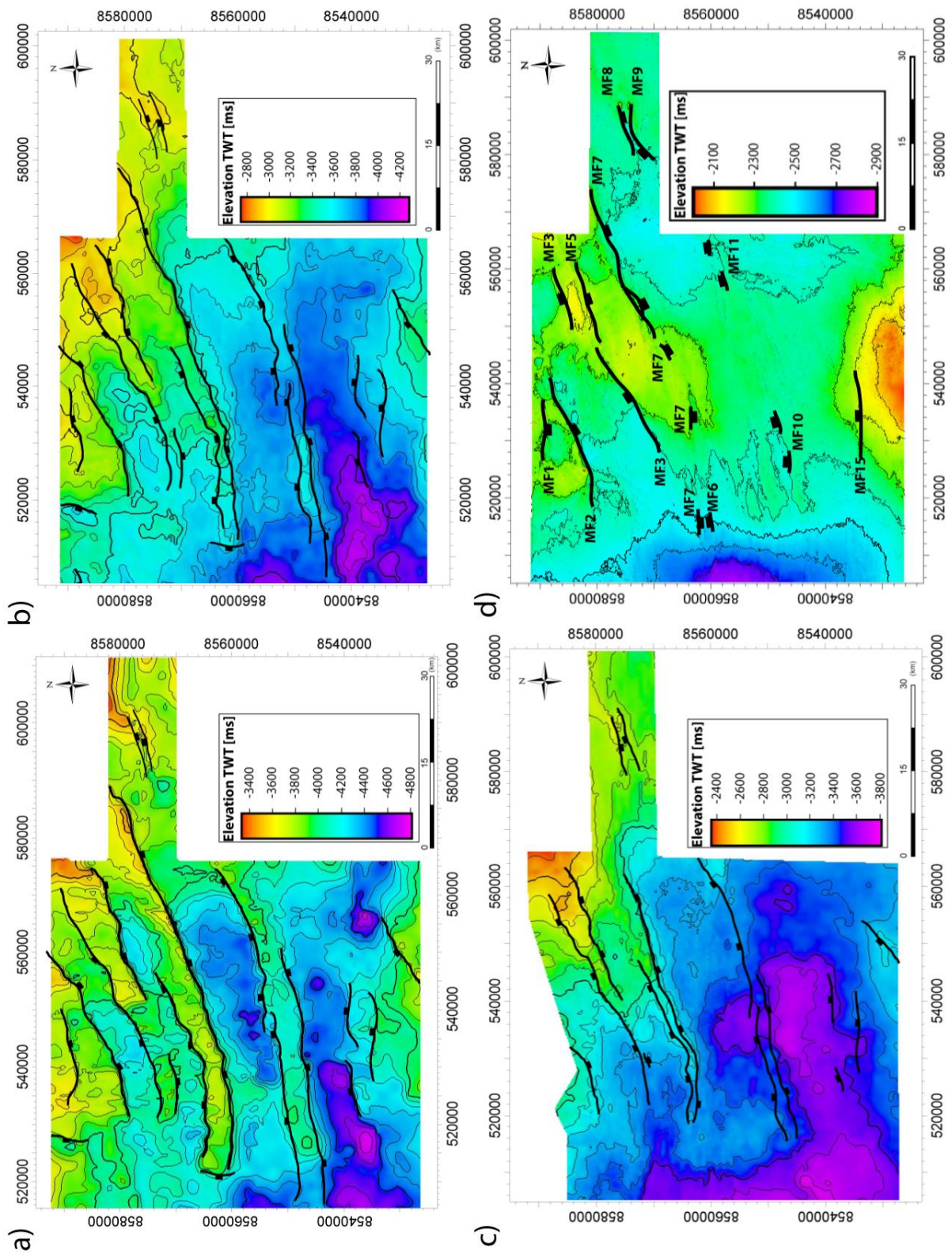
Figure. 5.2: Horizons colour coded based on elevation values (ms TWT). Normal-faults are marked as black lines, with black boxes located on the hanging walls. **(a)** The Top Permian horizon. **(b)** The Base Jurassic/Top Triassic horizon. **(c)** The Base Cretaceous horizon. **(d)** Turonian horizon map, only major rift faults are labelled with belonging acronyms.

The Turonian horizon has the deepest area in a basin to the west (-2900 ms TWT) (Fig. 5.2d). Whereas the persistent deep basin at the previous horizon maps, south of MF12, is now part of an N-S-striking ridge highest elevated in the south (-2100 ms TWT). Further, is the horizon under less structural control than the other horizons and the present faults exhibit much less displacement than on any of the underlying horizons. However, some of the major faults labelled on the basement horizon are offsetting this horizon, with a slight strike-rotation, and as non-continuous segments. MF3, MF7, MF10 and MF11 are interfering, as separate segments in more than one place. Moreover, because the Turonian horizon is at a depth located between the major faults cutting Base Cretaceous and the Neogene faulting (Fig. Cross-Sections), are faults marked on this horizon, geometrically connected from the basement up to the Neogene.

5.2 Neogene Faulting

The Base Miocene horizon (Fig. 5.3) has an overall shallowing trend from west to east, with elevation differences up to 800 ms TWT. The highest elevated areas occur at the bottom southeast and upper northeast corner of the largest square. The Neogene faulting is extensive especially in the field above the basement faulting in the eastern area. Clustering above the pre-existing faulting in bands with an orientation closely matching the major faults below. Whereas in areas with no obvious basement fabrics, are faults at the Base Miocene horizon mainly not present, except some small faults in the western part. Also generally low amounts of faulting in the deepest areas at -1700 ms TWT.
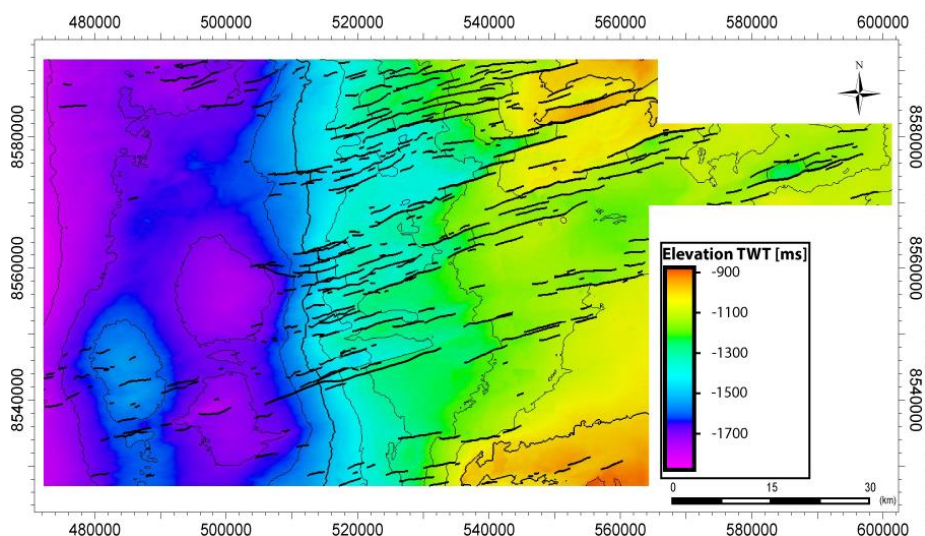
Figure. 5.3: The Base Miocene horizon with faults cutting the surface marked in black. Horizon elevation is displayed in colours according to scale.

5.3 Evidence of fault activity

5.3.1 Paleozoic

The time-thickness map between the basement horizon and the Top Permian horizon ranges from 300 ms to 1200 ms TWT (Fig. 5.7a), with thicker deposits generally located within hanging walls of major faults. However, MF1 and MF5 have thin time-thickness in the hanging walls, suggesting little activity in this period (e.g. Cross-sections). Major fault 2 and MF3 together form a graben with thicker deposits localised in seemingly three basins. Between MF6 and MF4 form a graben in the centre of the study, with especially thick deposits (up to 1000 ms TWT) in the western part of MF6. Major fault 7 is the largest fault in the area, and together with MF10 and MF11 forms two grabens, where the Paleozoic-thickness is up to 800 ms TWT.
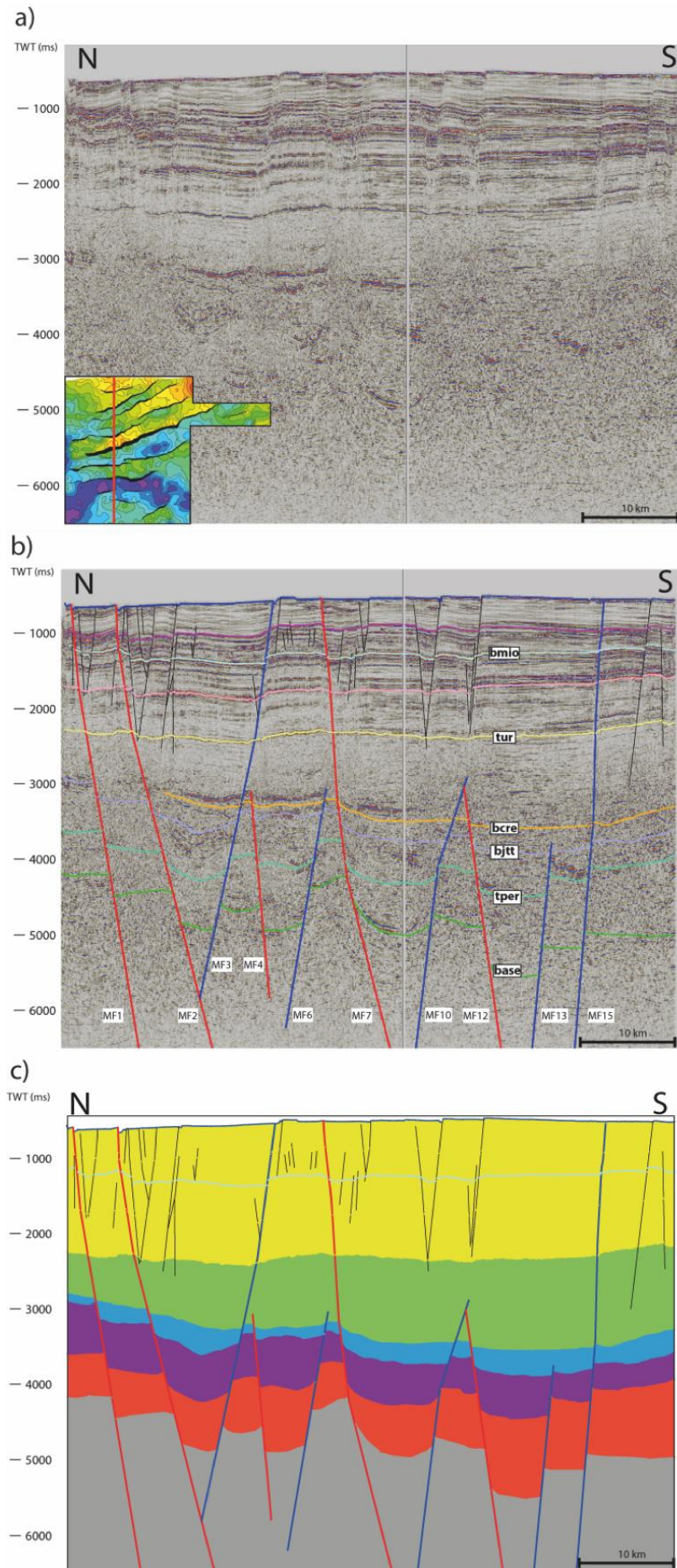
Figure. 5.4: Seismic line orientated N-S in the western part of the study area with most exhibited faulting. **(a)** the seismic cross-section, with the location marked by a red line on the basement horizon in the lower left corner. **(b)** Cross-section with interpreted horizons and faults. Horizons and faults used in results are marked with acronyms. S-dipping major faults are marked as red, and N-dipping as blue. Neogene faults are marked with black. **(c)** Time-periods are filled in with official geological timescale colours appropriate for the time-periods. Basement (grey), Permian (red), Triassic (purple), Jurassic (blue), Cretaceous (green), Cenozoic (yellow). The Cretaceous succession stops at Turonian due to lack of Base Paleocene horizon.

Figure. 5.5: Seismic line number two orientated N-S in the middle of the study area with most exhibited faulting. **(a)** the seismic cross-section, with the location marked by a red line on the basement horizon in the lower left corner. **(b)** Cross-section with interpreted horizons and faults. Horizons and faults used in results are marked with acronyms. S-dipping major faults are marked as red, and N-dipping as blue. Neogene faults are marked with black. **(c)** Time-periods are filled in with official geological timescale colours appropriate for the time-periods. Basement (grey), Permian (red), Triassic (purple), Jurassic (blue), Cretaceous (green), Cenozoic (yellow). The Cretaceous succession stops at Turonian due to the lack of Base Paleocene horizon.
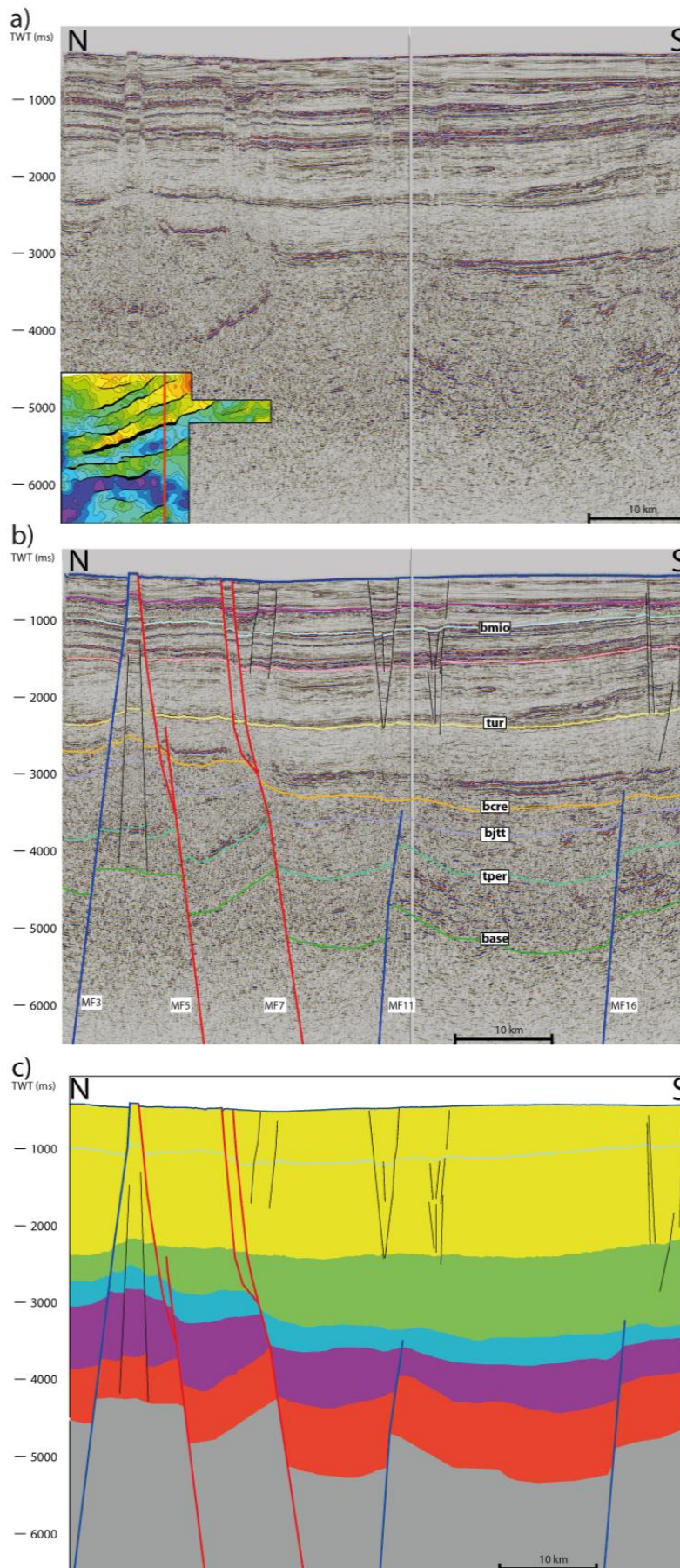
Figure. 5.6: Seismic line number three orientated N-S in the eastern part of the study area with most exhibited faulting. **(a)** the seismic cross-section, with the location marked by a red line on the basement horizon in the lower left corner. **(b)** Cross-section with interpreted horizons and faults. Horizons and faults used in results are marked with acronyms. S-dipping major faults are marked as red, and N-dipping as blue. Neogene faults are marked with black. **(c)** Time-periods are filled in with official geological timescale colours appropriate for the time-periods. Basement (grey), Permian (red), Triassic (purple), Jurassic (blue), Cretaceous (green), Cenozoic (yellow). The Cretaceous succession stops at Turonian due to lack of Base Paleocene horizon.

The easternmost segment of the MF7 forms a smaller half-graben with sediment thicknesses up to 1000 ms TWT. In the southern part of the study, the hanging wall of MF12 is very thick (up to 1200 ms TWT) particularly to the eastern and western parts of the fault. As well as some degree of thickening in graben formed with MF13 and MF14 (up to 800 ms TWT). In the south of the study area, MF15 and MF16 both have thicker sediments in their hanging walls (1100 ms TWT), compared to their footwalls (up to 700 ms TWT). All the mentioned thicknesses are thickening in the hanging wall toward fault planes (e.g. Fig. 5.6c).

5.3.2 Mesozoic

5.3.2.1 Triassic

The time-thickness map between top Permian and Base Jurassic has thickness variations between 200 ms and 1000 ms TWT (Fig. 5.7b). Major fault 1, which was not active during the Paleozoic shows more evidence of activity in the Triassic. Thickening west-east in hanging wall along the segment (up to 1000 ms TWT thick). Major fault 2 and MF3 show much of the same thickness trend as in Paleozoic. Major fault 5 goes from being inactive in Permian to be the most active fault in the Triassic with sediment thickening up to 1000 ms TWT in its hanging wall (Fig. 5.6). South of MF5, the graben between MF4 and MF6 has thin thicknesses (up to 600 ms TWT) that make it seem inactive. However, MF6 has a thickening-trend in areas outside the graben (up to 800 ms TWT). Major fault 7 show much of the same tectonic trends as before with thicknesses reaching up to 800 ms TWT, in the easternmost part of its hanging wall and in the graben between it and MF11. Moreover, the thickness is less in the graben between MF7 and MF10 (700 ms TWT at most). To the south, MF12 has two areas with thickest sediments in the hanging wall towards the centre of the segment (700 ms TWT). These two regions correspond to the location of the hanging walls to the smaller faults MF13 and MF14. Southward in the study area, MF15 has nearly no thickness contrast in footwall (500 ms TWT) to the hanging wall (400 ms TWT). In the southernmost part of the study, MF16 has sediments that thicken toward the eastern part of the segment (up to 900 ms TWT).

5.3.2.2 Jurassic

The time-thickness map for Jurassic is thinner compared to the others, with a minimum of 0 ms TWT and maximum at 650 ms TWT (Fig. 5.7c). MF1 is not visible on this map due to an erosion of the Base Cretaceous horizon in that section. As for the previous time-thickness maps, the thickest areas are less restricted to the hanging walls of major faults.
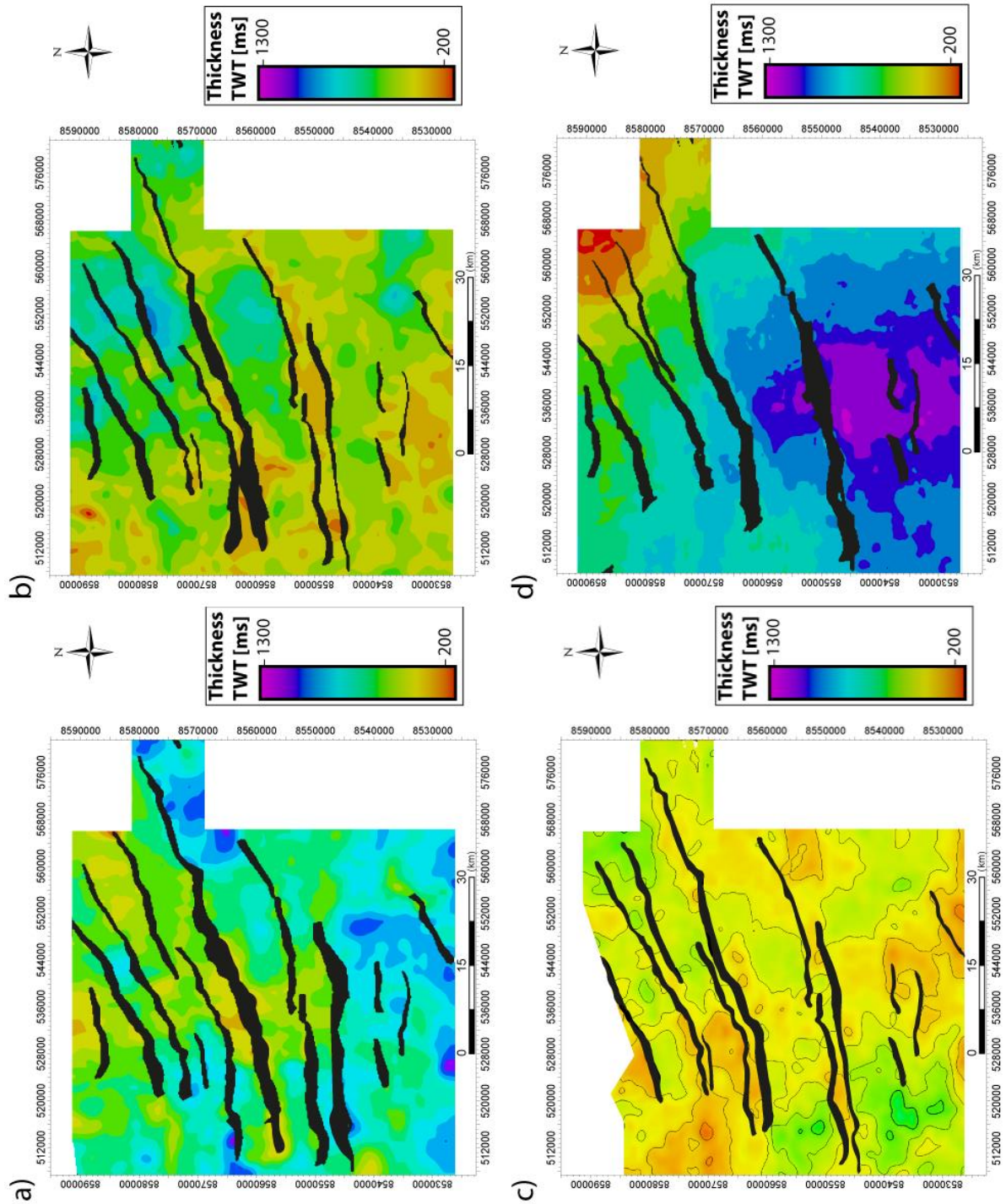
Figure. 5.7: Time-thickness maps for four time-intervals, with thicknesses displayed in colours according to scale in TWT (ms). MF8 and MF9 are so closely spaced that it's not possible to depict much from the isochore maps, and are therefore removed from the maps. **(a)** Permian, **(b)** Triassic, **(c)** Jurassic, **(d)** Interval between the Turonian horizon and the Base Cretaceous horizon. For the eroded part of the Base Cretaceous horizon is the horizon extrapolated.

The northernmost part of the study area reaches a thickness up to 600 ms TWT and is unaffected by the presence of MF3 and MF5. From what is visible, MF2 have 400 ms TWT thicker sediments in the hanging wall compared to the footwall, indicating some activity. The graben

between MF4 and MF6 (200 ms TWT) have no thickness contrast compared to their footwalls (200 ms TWT), and the segment edges to MF6 do not affect the thickness either. Major fault 7 across the centre of the study area, still show a thickening-trend in three basins in the hanging wall, with notably thicker sediments (up to 600 ms TWT) in the western part of the graben between it and MF10. The area in the graben Between MF7 and MF11 do not display any thickness changes, except a small area with a thickness difference (up to 200 ms TWT) on the western part of the hanging wall to MF11 compared to its footwall. There are two areas with thicknesses up to 600 ms (TWT) in the southwest of the study, in the hanging wall to MF10 and in the graben between the hanging wall to MF12 and MF13. With the two areas separated by a thinner line (200 ms TWT) in the MF10 and MF12 footwall. Thus, MF12 displaying some activity in the western part of the segment. In the south, have three of the N-dipping faults (MF14, 15 and 16) the same thickness in footwalls (200 ms TWT) compared to in hanging walls (200 ms TWT). Therefore more or less inactive in Jurassic.

5.3.2.3 *Cretaceous*

The time-thickness map for the time-interval between the Base Cretaceous horizon and the Turonian horizon (Fig. 5.7d), display very thick sediments (up to 1300 ms TWT) in the southern part of the study area. Especially thickening inwards to the centre in the graben between MF7 and MF10/MF11. Thus, there are no longer thickening deposits in three distinct basins along in the hanging wall to MF7. In the eastern part of the MF7 segment, it set up the basin structure with thicker thicknesses, by faulting down the Base Cretaceous horizon (Fig. 5.6). The 1000 ms TWT thick sediments continue as a band to the south of MF10 and MF11, in the hanging wall to MF12 and further south (through MF13, 14 and 15). This general southward thickening-trend is nearly unaffected by faulting, therefore are the thickening more likely to be controlled by thermal subsidence. However, there are slight offsets in hanging walls towards the corresponding fault planes at some of the faults, indicating that some major faults in addition to MF7 were active in this period.

5.3.3 Cenozoic

The Base Miocene horizon is in the last bit of the thermal subsidence phase, and just before/at the start of the final basin reactivation event, which provided extensional tension in parts of Browse Basin. Hence, this makes the Base Miocene horizon representative for the faulting related to the basin reactivation (Fig. 5.3). These Neogene faults appear as clusters of conjugating faults where the major rift faults have reactivated up or just above terminating

major rift faults (Fig. Cross-sections). There is seemingly a trend of antithetic faults in the hanging wall of reactivated major rift faults, and most of them are located in the time-interval between the Base Eocene and the Seabed, with a few faults originating and terminating below.
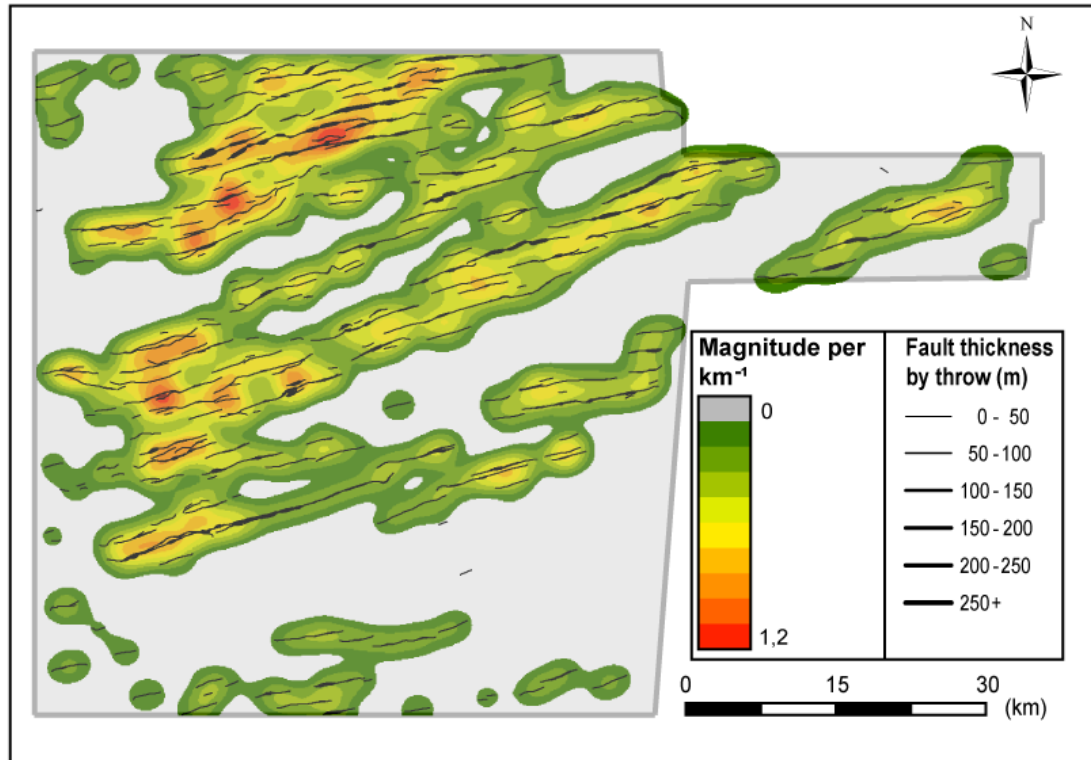
Figure. 5.8: Density plot of faulting at the Base Miocene horizon. Fault throw is labelled by the thickness of the fault segments. Density is displayed according to colour scale.

The intensity of Neogene faulting is well displayed with the use of a density plot (Fig. 5.8). The faulting follow bands of higher density, which aligns well with the deeper lying major faults. It is possible that the density-blob around MF8 and MF9 in the east of the study area is a part of a larger blob, but cut to the west by the edge of the cube. An exception to the bands is the high intensity located above MF1/MF2 and particularly at the western segment-tip to MF2, where the density is much broader. There is also high intensity at the western end of the MF6/MF7 segment. Making up an overall tendency of higher density-values on the western parts of the continuous density bands.

6 Results – Fault network analysis

This chapter outlines an analysis of the fault network based on the orientation, frequency, length of the faults and the throw distribution along faults. The main focus has been towards Paleozoic-Mesozoic rift faults at the Base Jurassic horizon, and Neogene faults at the Base Miocene horizon, both separately and in coherence with each other.

6.1 Organization of faulting

Faults cutting the Base Jurassic horizon have mostly ~N/S dipping faults, somewhat equally 5 kilometres spaced (Fig. 6.1a), except for the southern area where four faults (MF13, 14, 15, 16), all dip towards the N. The faults affecting the Base Miocene horizon follow conjugating en-echelon fault bands trending sub-parallel to faults cutting the Base Jurassic and striking ENE-WSW (Fig. 6.1b). Along these fault bands, individual faults dip towards the N along the southern edge of the band and dip S along the northern edge of the band. The northernmost part of the study area Base Miocene, faulting is more chaotic regarding orientations and dip directions, even though it is still possible to see a trend of S dipping faults following the orientation of MF1 and MF2 with a slight strike-rotation. In the northernmost part of the study area are all faults cutting the Base Miocene horizon located in the western part of the hanging wall and footwall of MF1 and MF2, building up a physical link between faulting above MF1 and MF2.
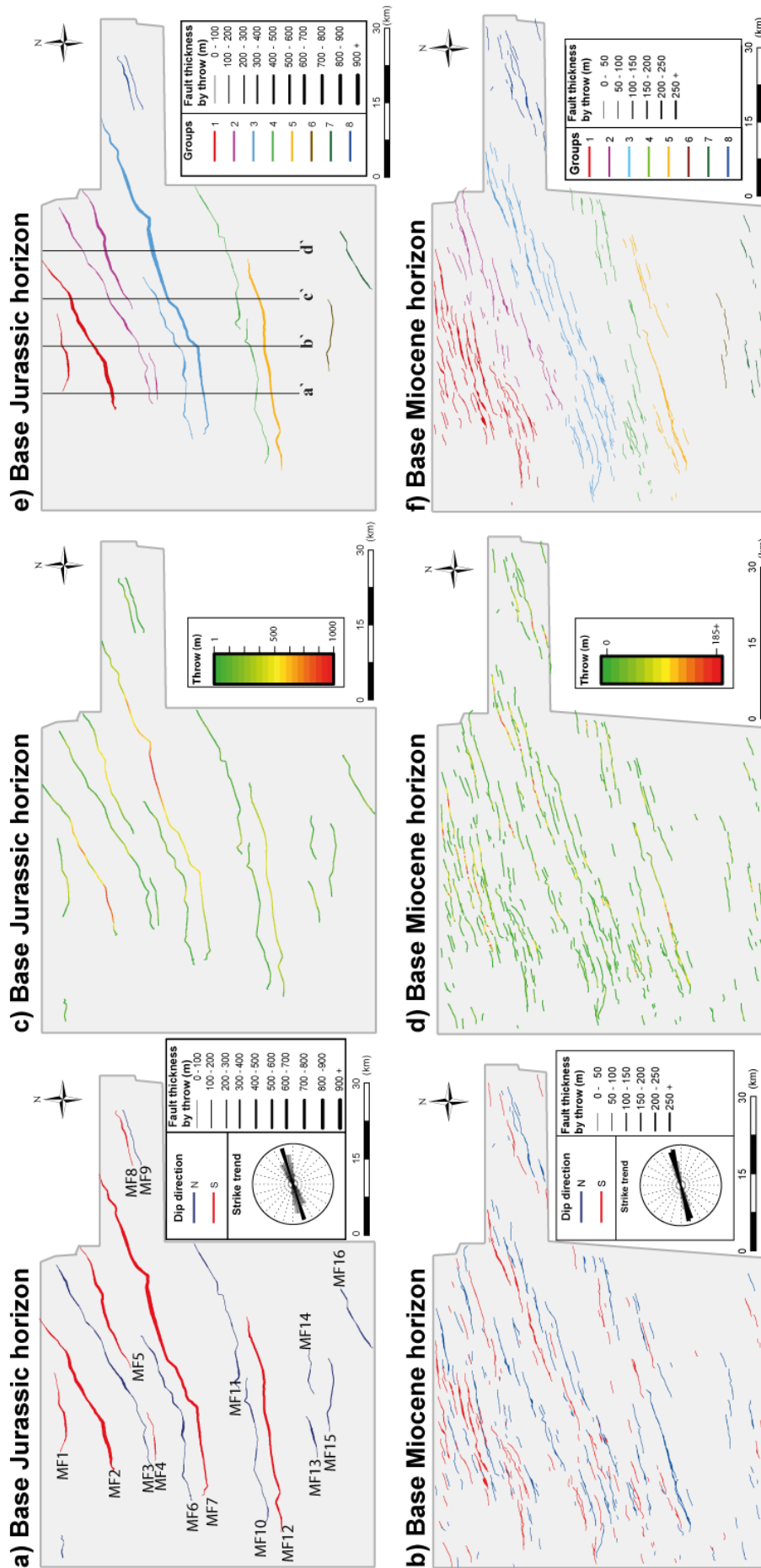
Figure. 6.1: (a) Fault orientation Base Jurassic horizon, with dip directions marked as blue or red. The main average strike is displayed in black on a rose diagram. **(b)** Fault orientation Base Miocene horizon, with dip directions marked as blue or red. The thickness of the fault planes indicate the throw values. The main average strike is displayed in black on a rose diagram. **(c)** Throw map Base Jurassic horizon; throw is displayed with coloured fault planes according to scale. **(d)** Throw map Base Miocene horizon; throw is displayed with coloured fault planes according to legend. Colours distinguish the cluster groups according to the Base Jurassic horizon. Fault thickness represents the throw values. **(e)** Cluster group map of faulting at the Base Jurassic horizon. Colours distinguish the cluster groups according to legend. Fault thickness represents the throw values. Black lines marked with a`-d` is the sampling lines for the cumulative plots (Fig. 6.5). **(f)** Cluster group map of faulting at the Base Miocene horizon. Colours distinguish the cluster groups according to legend. Fault thickness represents the throw values.

The small difference in fault strike between the Base Jurassic horizon and the Base Miocene horizon is well displayed in rose diagrams (Fig. 6.2). These rose diagrams display average fault strikes by showing bin-size groups, which group faults within intervals of five degrees'. Faults cutting the Base Jurassic horizon have a mean strike of 62.45° (Fig. 6.2c) and the mean strike of faults cutting the Base Miocene horizon is 70.78° (Fig. 6.2a). When LxT weighted, faults cutting the Base Jurassic horizon have a mean strike of 66.95° (Fig. 6.2d) and the mean strike of faults cutting the Base Miocene horizon faults is 72.32° (Fig. 6.2b). In addition, faults cutting the Base Jurassic horizon have a dominant bin on 70-75 degrees' and 75-80 degrees' as second largest. The faults cutting the Base Miocene horizon is slightly different with a dominant bin on 75-80 degrees' and 70-75 degrees' as the second largest. Rose diagrams at both horizons show persistently the same largest bin-groups at both the regular and the weighted rose diagram.

Although there is an overall eight degrees' rotation in the strike of the faults between the two horizons, there are individually large variations at the Base Jurassic horizon. Giving a large spread in the rose-diagram (Fig. 6.2c). The most significant difference in orientation being between MF15 and MF16 (Fig. 6.1a), where the difference is greater than 45 degrees'. Despite individual variations in strike on the Base Jurassic horizon, there is an overall clockwise rotation from the eastern part to the western part of the study area along the major fault segments.
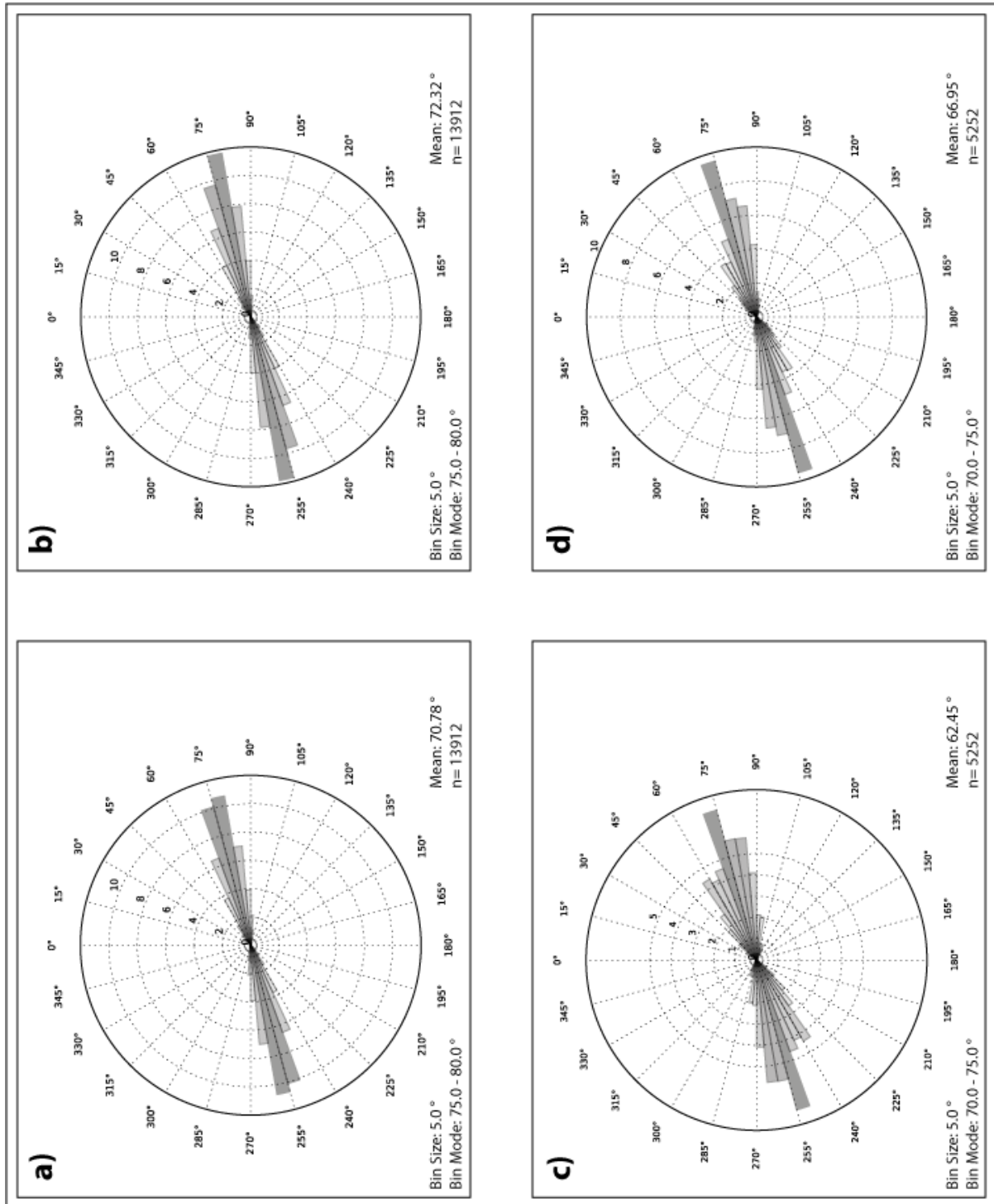
Figure. 6.2: Rose diagrams with fault orientations. **(a)** Orientation faulting Base Miocene. **(b)** Length x Throw weighted orientation faulting Base Miocene. **(c)** Orientation faulting Base Jurassic. **(d)** Length x Throw weighted orientation faulting Base Jurassic.

50

6.2 Distribution of throw

On the Base Jurassic horizon most of the major faults exhibit maximum throw values around 500 meters, with MF2 and MF7 as exceptions reaching 1000 meters at most (Fig. 6.1c).

The throw values for faults cutting the Base Miocene horizon varies from a couple of meters to 295 meters. The faults that exhibit highest throw values are seemingly in same zones (Fig. 6.1d).

All maximum throw values for Neogene faults cutting the Base Miocene horizon and major rift faults cutting the Base Jurassic horizon, are plotted against their belonging fault lengths in a logarithmic plot (Fig. 6.3). Ideally, a straight line would match all the points, but that is very rarely the case. Majority of the two fault-sets fit within two orders of magnitude, from L/Tmax=10 to L/Tmax=1000. Where most of the faults in the two fault-sets plot close to L/Tmax=100, suggesting that they are related to each other. At the fault length of approximately 800 meters, there are faults with throw values that vary from a couple of meters to nearly hundred meters. This effect is due to a sampling error from the interpretation since fault interpretation are on every 64th crossline, which equal interpretation with a spacing of 800 meters. This problem with faults aligning on a vertical line is noticeable at higher length values as well.
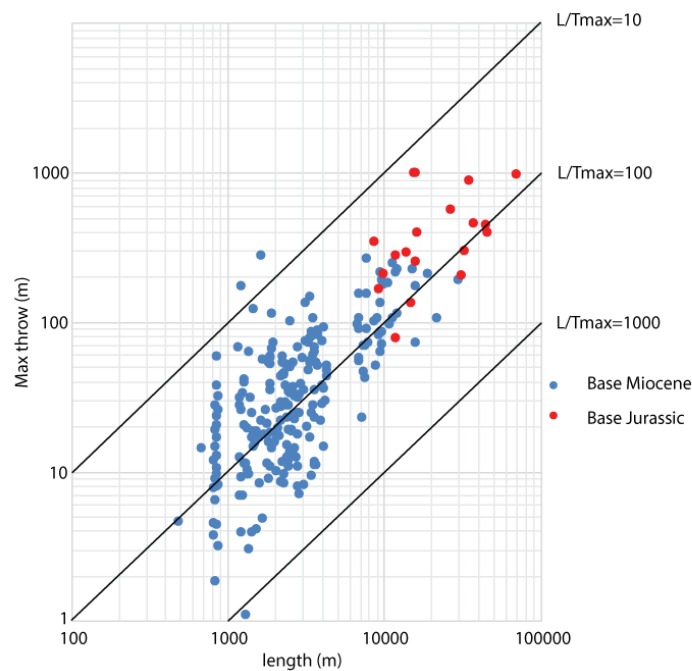
Figure. 6.3: Maximum throw (y-axis) plotted against fault length (x-axis) for the Base Jurassic horizon faults as red dots, and the Base Miocene horizon faults as blue dots.

Frequency-size analysis of the Neogene faults displays frequency-size distributions for both length and throw (Fig. 6.4). The faults plot nicely along a straight line in the negative exponential for both parameters. While for the Power-law plots, the faults resemble a geometry closer to a curved line than a straight line. This straight line signifies that there are less large faults within the population, hence more moderate and smaller faults, with belonging low throw values. Due to the fault population being mainly layer bound and restricted to only the Paleogene and Neogene strata (e.g. Fig. Cross-sections)
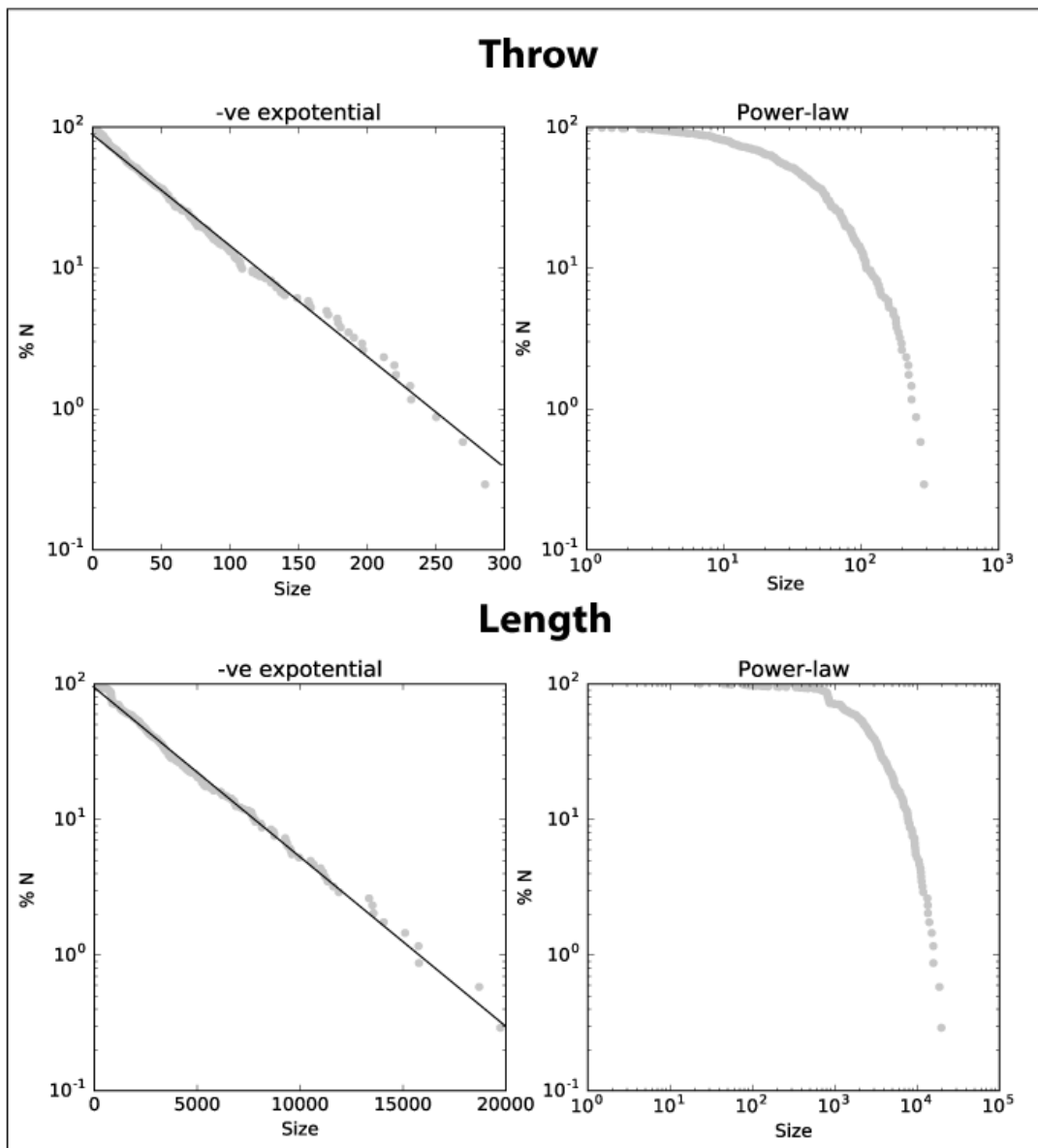
Figure. 6.4: Logarithmic plot featuring negative exponential and power-law for throw values and length-values collected for Neogene faults at the Base Miocene horizon.

6.3 Spatial heterogeneity analysis

The Neogene faults have been divided into cluster groups that reflect their kinematic interference to faults at the Base Jurassic horizon (figs. 6.1e and 6.1f). The cluster groups are numbered 1-8, and the few faults that are not regarded to be a part of these eight cluster groups are not included for further analysis. The cluster groups vary in size from a few faults to tens of faults, of which cluster groups 1 and 3 are the ones with the largest magnitude. Both these two cluster groups hold a major fault with throw values reaching 1000 meters (Fig. 6.1c).

In order to display variations in frequency and throw values throughout the Neogene fault population a spatial heterogeneity analysis was performed (Fig. 6.5). The analysis features four S-N sampling lines (a`, b`, c` and d`) through the major cluster groups (1-5) with a 10 km W-E spacing (Fig. 6.1e).

At the western end of the fault network (sampling line a` in Fig.6.1e), the V_f-value for throw and frequency are 0.46 and 0.19, respectively (Fig. 6.5a). The highest throw values are mostly located at the edges, especially within cluster group 1, which contains more than double the number of faults than any of the other cluster groups. However, the highest throw values are located mainly on two faults. This is also the case on the opposite side of the sampling line within cluster group 5, where two faults together inhibit 200 meters throw. In cluster group 4 the number of faults is the same as in cluster group 5, but exhibit only half the cumulative throw. In cluster group 3, the frequency increases compared to cluster group 4, but the throw values decrease to significantly smaller values. Hence, the throw values flatten out in the middle, before they slightly increase within a few faults in cluster group 2. Giving an overall homogenous frequency distribution and high throw values within both the two cluster groups at the edges, which decrease towards the middle. Cluster group 1 is vast and contains over half of the frequencies, displaying a nearly straight line, and half of cumulative throw values. In addition, sampling line a` has the highest accumulated throw values and frequencies out of the four sampled lines.

At sampling line b` (Fig. 6.1e) the V_f-value for the throw is 0.42 and the frequency is 0.36 (Fig. 6.5b). In the southern part of the sampling line, cluster groups 5 and 4 contain one fault each, and both these cluster groups have a significant decrease in the throw from the previous sampling line. In the middle, cluster group 3 has an increase in cumulative throw with values above 150 meters produced by two faults in a narrower cluster group. Further north at cluster

group 2, four faults display moderate throw values that sum up to approximately 100 meters. At the edge, cluster group 1 contains eight faults with a total throw of 400 meters of which, 200 m are concentrated on a single fault. Overall, sampling line b` displays a rapid increase in throw and frequency at cluster group 3 and especially in cluster group 1. Cluster group 4 has low values for both, possibly because the sampling line is located at the interaction point between two faults within the cluster group. Compared to sampling line a`, have sampling line b` exhibits homogenous frequency, whereas throw values are similar.

At sampling line c` (Fig. 6.1e), the V_f value for throw and frequency is 0.38 and 0.24, respectively (Fig. 6.5c). In the southern part of the sampling line, cluster group 5 and cluster group 4 consist of two faults each, where cluster group 5 exhibits close to zero throw and cluster group 4 a total throw of 100 meters. In the centre of the sampling line, cluster group 3 contain the highest frequency sampled along the line, but only a maximum of 50 meters throw for a single fault. Further north, cluster group 2 consists of three faults, where one fault exhibits nearly 200 meters throw. Cluster group 1 at the northern edge of the sampling line still possess five faults, where the highest throw values are seemingly located within three faults. In general, a large proportion of the throw values are located within cluster groups 4, 2 and 1, whereas the frequency values are more equally distributed within the cluster groups and the only significant gap without faults is between cluster groups 4 and 3. Overall, frequency is more homogenous than throw.

For sampling line d` (Fig. 6.1e), V_f values for throw and frequency are 0.39 and 0.27, respectively (Fig. 6.5d). Cluster groups 5 and 1 both exhibit low frequency- and throw values on the outer edges of the sampling line. With an increase in both spectres at cluster group 2 and 4 and highest throw values exhibited by two faults within cluster group 3, the total throw distributed along sampling line d` is considerably lower than for the other three lines, even though the frequency is just a fraction lower. The total throw values for the other lines are above 700 meters, whereas for this line it is below 200 meters.
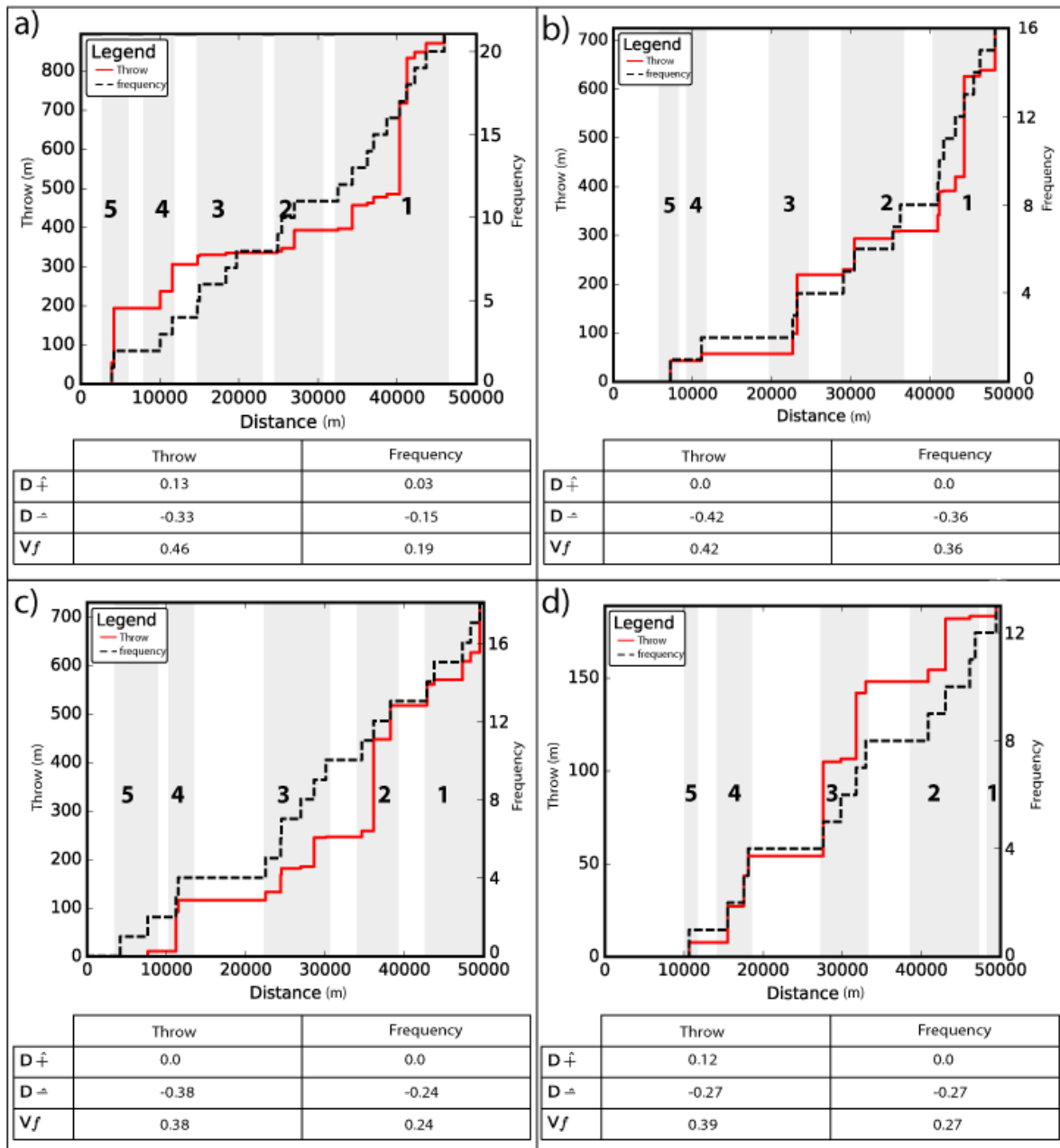
Figure. 6.5: Cumulative plots along four different sampling lines, sampling S-N. The throw is displayed with a continuous red line with scale on the left-hand side. Frequency is displayed with a stippled black line with a scale on the right-hand side. The light grey area with labelling numbers display which cluster group the values belong in. A table at the bottom of each plot displays positive deviation, negative deviation and heterogeneity parameter, for throw and frequency. Localisation of the sampled lines is displayed in Fig. 6.1e. **(a)** Sampling line a`. **(b)** Sampling line b`. **(c)** Sampling line c`. **(d)** Sampling line d`.

Overall, all V_f values are consistently below 0.5 for both throw and frequency, therefore the Neogene fault network is closer to being homogeneous than heterogeneous. Furthermore, the throw is more heterogeneous than the frequency in all four sampling lines, with high throw values accumulated within few faults in all sampling lines. In addition, the V_f throw values are consistent within all four sampling lines, ranging from 0.38 to 0.46. V_f frequency values vary

more, ranging between 0.19 and 0.36. Cluster group 5 has high throw values located within one fault at the westernmost sampling line (a`), whereas for the rest of the lines frequency and throw decreases from west to east. Cluster group 4 contains on average two faults and has total throw values exceeding 100 meters at the first and third sampling line (a` and c`). Cluster group 3 shows a trend of high frequency values opposite to high throw values where the largest throw values are located within a few number of faults at the second and fourth sampling line (b` and d`). Cluster group 2 shows a slight trend of increasing throw towards the east within the three first sampling lines (a`, b` and c`). Cluster group 1 is the largest cluster group in the west, with regards to both frequency and throw but becomes less dominant towards the east.

6.4 Relationship between cumulative fault throw and fault frequency

As well as cumulative plots oriented S-N the fault network analysis includes throw and frequency analysis for cluster groups 2, 3 and 4 oriented W-E along the cluster groups. The diagrams (Figs. 6.6, 6.7 and 6.8) are cumulated values sampled N-S with a spacing of 1000 meters from W to E. The values include normalised average throw/frequency, throw and frequency for faults affecting the Base Miocene horizon, and throw for major faults affecting the Base Jurassic horizon. The fault values from the Base Miocene horizon are presented as both raw data and as 3-point average.

Cluster group 2 (Fig. 6.6) displays an interaction of three major rift faults that form three distinct throw highs (at the 7, 18 and 38 km mark), where the eastern top has a total of more than 850 meters throw. This eastern throw-top equals to more than twice the amount of the second largest top in the centre. The frequency-plot for Neogene faults form a wavy bell-curve with three tops in the centre (at the 11, 20 and 28 km mark). This frequency bell-curve is not affected by the high throw accumulation from the major rift faults, except slightly higher overall frequency value in the eastern part of the plot compared to the western part of the plot. The frequency-plot has three distinct tops in the centre, one of which coincides with tops in the throw profile, and a non-matching tops out on the eastern flank of the plot (at the 35 km mark). Both these two throw-tops match roughly to the largest tops within the Base Jurassic horizon throw-profile. All the three throw-highs within the Base Jurassic horizon match well with the placing of the largest circles in the throw/frequency diagram. The largest circles (at the 35 km mark) matches
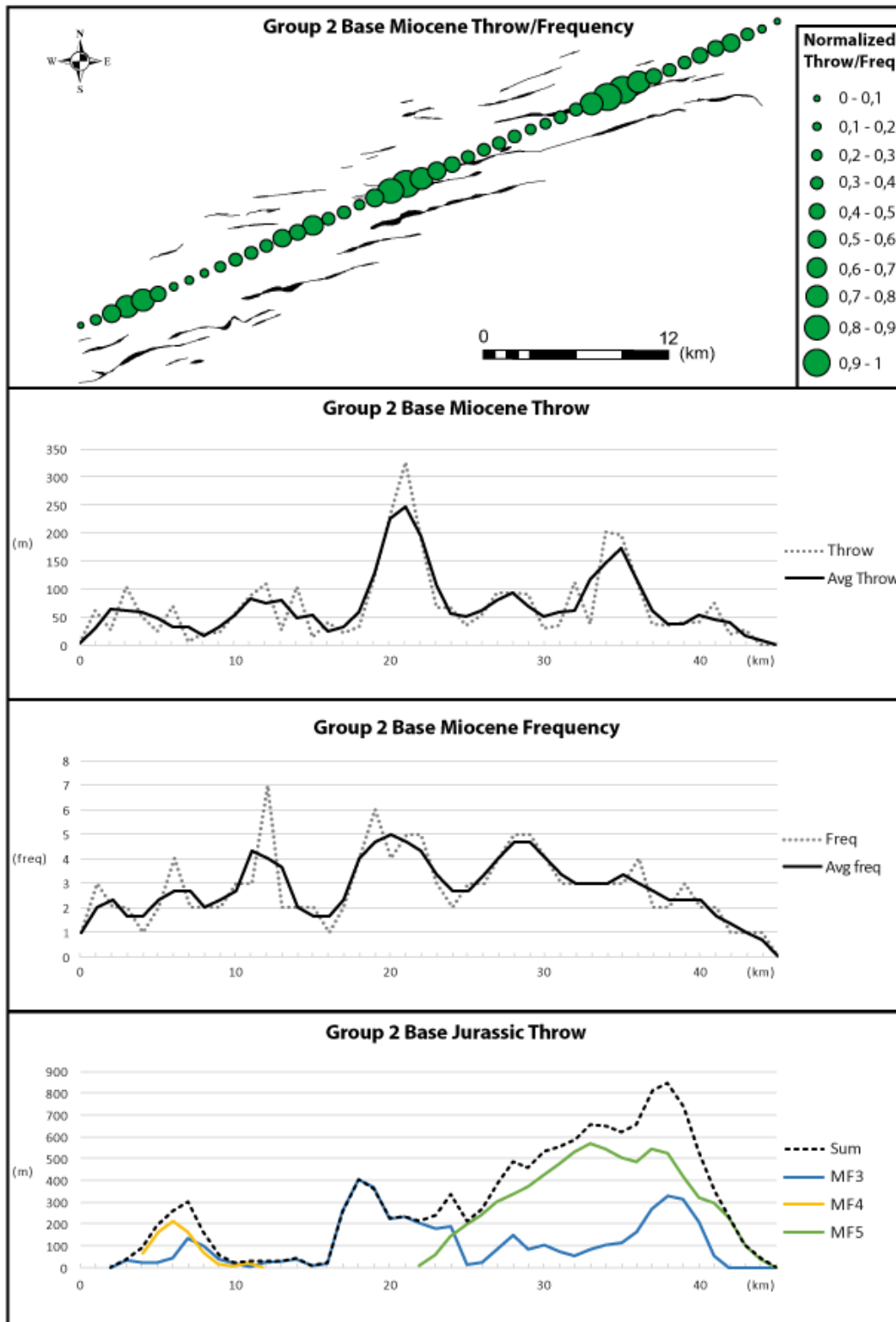
Figure. 6.6: All profiles are oriented West-East, and are aligned after same scales, with same sampling spacing. **Cluster group 2 Base Miocene Throw/Frequency** is displayed as green circles with sizes according to scale. The Neogene faults within the cluster group are displayed underneath. **Cluster group 2 Base Miocene** have cumulative throw as stippled, and three-points weighted average as a solid black line. **Cluster group 2 Base Miocene Frequency** have cumulative frequency as stippled, and three-points weighted average as a solid black line. **Cluster group 2 Base Jurassic Throw** have summarised throw as a stippled line, and MF's as solid coloured lines according to scale.

57

approximately to the highest point at the Base Jurassic horizon throw-profile and the Base Miocene horizon second highest throw-peak. Indicating an overall trend where the localisation of higher throw values within major rift faults at the Base Jurassic horizon match areas with fewer faults containing high throw values at the Base Miocene horizon.

Cluster group 3 (Fig. 6.7) is larger in magnitude than cluster group 2, and is related to MF6 and the more substantial MF7. These two major rift faults combine to form a wavy bell-curve, with the highest throw value located approximately in the centre (at the 51 km mark) with 1000 meters throw. The Base Miocene horizon frequency-curve has a similar shape as the major rift faults in the eastern part but has a frequency-high that stand out in the western part of the plot (at the 12 km mark). This frequency-top is located at the opposite end of the cumulative throw-top for the Base Miocene horizon (at the 60 km mark), giving highest frequency at the Base Miocene horizon towards the west, and the highest cumulative throw to the east for both Base Miocene horizon faults and Base Jurassic horizon faults. Interestingly, the greatest non-averaged cumulative throw value at the Base Miocene horizon match with the second highest cumulative throw value at the Base Jurassic horizon (at the 25 km mark). The throw/frequency-plot match the Base Jurassic horizon throw values quite well, with the largest circles located in the eastern part of the plot (around the 60 km mark). Also, tiny circles in the western part of the plot where major rift faults at the Base Jurassic horizon are not present (at the 0-12 km mark). Resulting in an overall trend similar to cluster group 2, where largest throw values at the Base Jurassic horizon match up with high throw values within a few faults at the Base Miocene horizon.
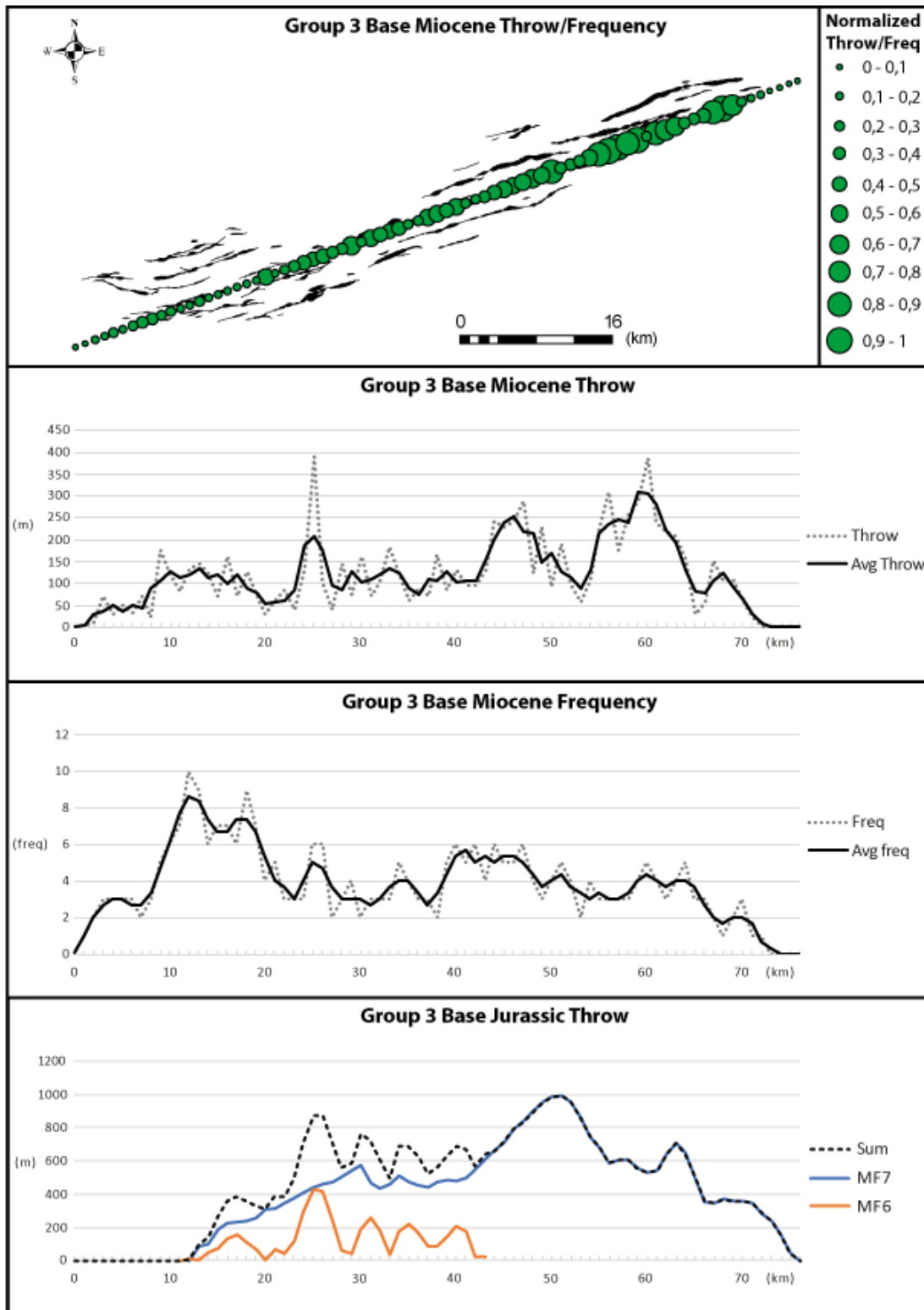
Figure. 6.7: All profiles are oriented West-East, and are aligned after same scales, with same sampling spacing. **Cluster group 3 Base Miocene Throw/Frequency** is displayed as green circles with sizes according to scale. The Neogene faults within the cluster group are displayed underneath. **Cluster group 3 Base Miocene** have cumulative throw as stippled, and three-points weighted average as a solid black line. **Cluster group 3 Base Miocene Frequency** have cumulative frequency as stippled, and three-points weighted average as a solid black line. **Cluster group 3 Base Jurassic Throw** have summarised throw as a stippled line, and MF's as solid coloured lines according to scale.

In cluster group 4 (Fig. 6.8) both MF10 and MF11 have highest throw values close to where they interact (at the 37 km mark) and a couple of smaller throw-peaks away from the centre. On the contrary, the Base Miocene horizon frequency-profile has its highest peaks at the outer edges to the major rift faults at the Base Jurassic horizons (at the 15 km and the 62 km mark). In addition, frequency values are very low at the point where MF10 and MF11 overlap. This is also the case for the Base Miocene horizon cumulative throw values, but also, this plot has a peak correlating with the highest throw-peak at MF11 (between the 41 and 43 km mark). Disregarding this throw-peak results in a cumulative throw-profile for the Base Miocene horizon of a similar shape to the frequency plot for Base Miocene horizon, with highs on the outer edges of the profiles. The Base Miocene horizon throw/frequency-plot displays high values in the centre of the plot that correlate with the centre throw-peak at the Base Miocene horizon and the highest throw-peak at the Base Jurassic horizon. Also, around the 20 km mark there is a cluster of larger throw/frequency-circles that correspond to the centre of MF10. Moreover, in the easternmost part of the throw/frequency-profile there is a sequence (20 km long) that has high values in the centre and decreasing values toward either side. At the western side of this sequence (the 45 km mark) the profile reaches zero due to no faults present. This is just 2 km west of where MF11 has a pronounced through in throw at the Base Jurassic horizon.

In general, the relationship between the two horizons for all three cluster groups are individual for each cluster group. However, there is a fit between the Base Miocene horizon of highest cumulative throw and the largest green circles from the throw/frequency-plot. Indicating high throw values where small amounts of faulting is visible. As well as several matches between high cumulative throw values at the Base Miocene horizon and high throw values at the Base Jurassic horizon.
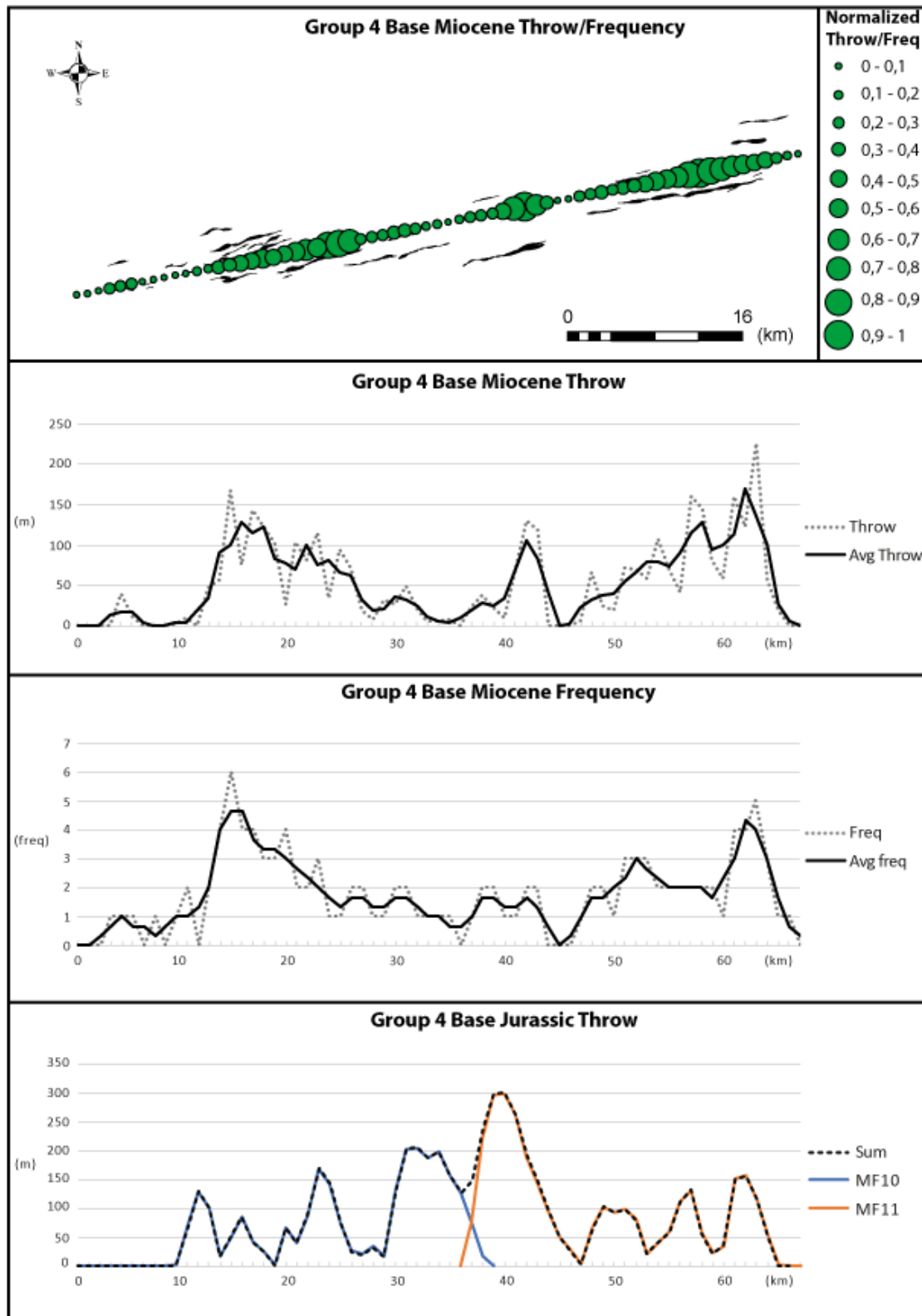
Figure. 6.8: All profiles are oriented West-East, and are aligned after same scales, with same sampling spacing. **Cluster group 4 Base Miocene Throw/Frequency** is displayed as green circles with sizes according to scale. The Neogene faults within the cluster group are displayed underneath. **Cluster group 4 Base Miocene** have cumulative throw as stippled, and three-points weighted average as a solid black line. **Cluster group 4 Base Miocene Frequency** have cumulative frequency as stippled, and three-points weighted average as a solid black line. **Cluster group 4 Base Jurassic Throw** have summarised throw as a stippled line, and MF's as solid coloured lines according to scale.

7 Results – Interaction between Paleozoic-Mesozoic rift faults and Neogene faults

This chapter will address the different throw-length and throw-depth profiles present in the Neogene fault population, along with 3D-models displaying connected segments in fault. Additionally, this chapter aims to elucidate the manner in which way major rift faults influence, interfere and control these profiles by connecting to segments of Neogene faults.

7.1 Throw distribution profiles

The throw distribution profiles of the interpreted major rift faults generally conform to a bell-shaped throw-length plot, with MF5 being the prime example (Fig. 6.6). Such bell-shaped distribution illustrates/highlights the largest throws being centred around the middle of the fault span. There are notable exceptions, however, such as MF11 that has its highest throw values focused in the western part of the fault (Fig. 6.8). Similar to the major rift faults, the Neogene faulting within the fault network comprises several different fault types with distinctive Tmax/length-profiles. These profiles can be classified as isolated/individual faults, single tip restricted faults, faults with two connected segments, and faults with more than two connected segments. The different profiles are grouped/classified according to where the highest throw are recorded along the strike of the fault (Fig. 7.1): west-asymmetrical (west), symmetrical (Centre/Equal) and east-asymmetrical (east).

Twenty-four individual faults with the distinctive bell-shaped throw distribution were identified in the fault network (Fig. 7.1a). The faults have an average length of 1313 meters, and an average maximum throw of 36 meters. For the asymmetrically distributed individual faults, the count reaches 38 for west-asymmetrical, and 31 for east-asymmetrical faults (Fig. 7.1b). The west-asymmetrical faults have an average length of 1430 meters and an average maximum throw of 38 meters. Whilst the east-asymmetrical faults and have an average length of 1430 meters and an average maximum throw of 36 meters. The west-asymmetrical faults are on average longer than the other two individual fault classifications but do not exhibit a higher maximum throw average.

The majority of Neogene faults within the fault network are geometrically connected segments. Where the faults set up by two fault segments, are separated regarding which of the two

segments that distribution the highest throw. The west-asymmetrical faults (Fig. 7.1c) are represented by 28 faults, with average lengths of 1835 meters and average maximum throws of 27 meters. The equal distribution is only represented by five faults, with a longer average length of 2013 meters and the smallest average maximum throw out of the three with 16.5 meters. The east-asymmetrical faults number 30 faults, and exhibit the longest average length at 2128 meters, and the highest average maximum throw at 35 meters.

Faults with more than two geometrically connected segments make up the majority of faults within the fault network. These faults are grouped in the same fashion as the faults consisting of two segments (Fig. 7.1d). The symmetrically distributed faults represent the largest group, counting 69 faults. These faults have the longest average length at 6846 meters and have a maximum throw of 78 meters. The west-asymmetrical faults are represented by 37 faults, with the shortest average fault length at 5911 meters and the largest average maximum throw of 87 meters out of the three groups. The east-asymmetrical is the smallest group out of the three, represented by 29 faults. It comprises the lowest average fault length, and maximum throw at 4697 meters, and 59 meters respectively.
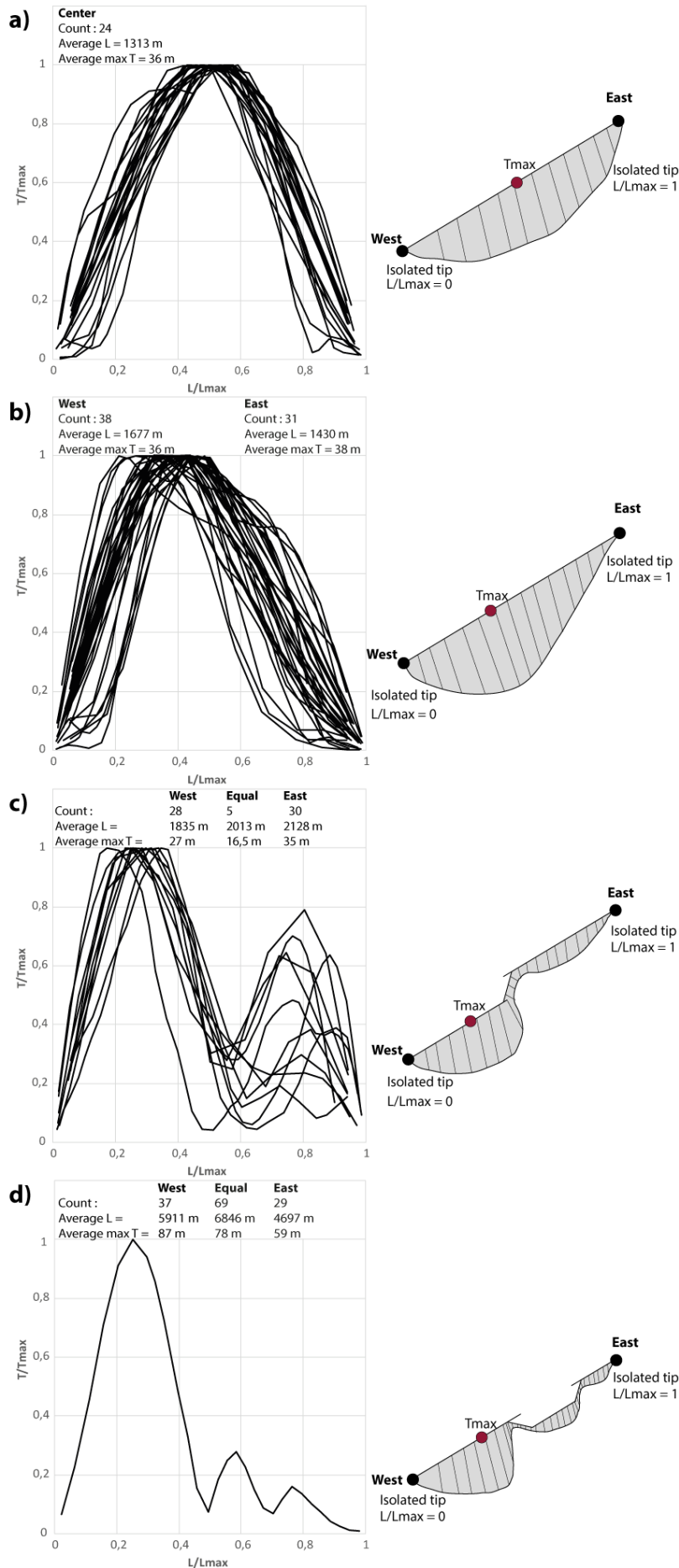
Figure. 7.1: Normalized fault throw plotted against normalized cumulative fault length. With resulting vergence profiles, including count, average fault length and average fault throw, labelled at the top of each profile. Associated schematic 3D-drawing on the right-hand side. (**a**) Single-tip restricted profiles, with vergence towards the W. (**b**) Individual/isolated bell-shaped profiles. (**c**) Fault profiles comprising two segments, with higher throw values towards the W. (**d**) Fault profiles comprising three segments, with higher throw values towards the W.

7.2 Linkage between reactivated rift faults and individual Neogene faults

The three different fault throw-length profile groups (symmetrical, east-asymmetrical and west-asymmetrical) are presented in map-view. These maps help illustrate significant trends in throw distribution profiles in cluster groups at the Base Miocene horizon (Fig. 6.1f). Furthermore, these groups are used in conjunction with maps scoring areas in which Neogene faults connect to major rift faults at depth (Figs. 7.2, 7.3 and 7.4). These composite maps help ascertain whether a correlation exists between connected segments, and the expression of corresponding fault throw-length distribution profiles. Such composite maps have been generated for a limited selection of fault-pairings including: MF3/MF5 (cluster group 2), MF7/MF6 (cluster group 3) and MF8/MF9 (cluster group 8). Additionally, throw-depth profiles have been made for MF3, MF5, MF6 and MF7, mainly calculated at the three cross-sections displayed in results section 4.3, in areas where they link up with Neogene faults (Fig. 7.5).

MF5 only connects in the central parts of the symmetrical fault on the downside of where **a** is marked (Fig. 7.2). Meanwhile, MF3 splays upwards to connect with parts of the en-echelon Neogene faulting on the upper side of the MF5 connected fault. It connects with two faults at the position **a**, and takes a "jump" south, stepping over MF5 and following a stepwise connection with faults at position **b** through **e**. These connections influence the systematic distribution of west-asymmetrical Neogene faults, as the western part of each fault is connected to MF3. Thus, MF3 affects the throw in places where it links up with Neogene faults. There is, however, one notable exception to this influence. The longer, symmetrical fault at position a, which is connected to MF3 in western part, has its highest throw values centred around the mid-point of the fault.

The throw-depth profile belonging to MF5 shows a normally distributed bell-curve with the highest throw at the Base Miocene horizon and decreasing values toward the seabed horizon and the Turonian horizon. The lower section displays a tilted gradient, which steepens after the Base Jurassic horizon, and connects with the Cenozoic bell-curve at the Turonian horizon (Fig. 7.5d). The throw-depth profiles for MF3 exhibit three very different profiles. At location **a,** where MF3 connects with the larger Neogene fault (Fig. 7.5c), the profile shows a small decrease in throw from the Base Eocene horizon to the Turonian horizon. The gradient further down is quite steep until it reaches the Top Permian horizon, where the inclination decreases. Further southwest, the profile changes character, and exhibits a throw-depth distribution similar

to that of the MF5 distributions. The profile shows a bell-curve at the top of the Cenozoic time-interval, and a steeper inclination below the Turonian horizon (Fig. 7.5b). Whereas the profile at the western end, where MF3 is geometrically connected to Neogene faulting, is a bit different (Fig. 7.5a). The bell-curve distribution is still present in the upper parts, but throw values at the Base Cretaceous horizon are closer to the values recorded at the Base Eocene horizon. In addition, the Base Jurassic horizon is nearly at being at the same depth, creating a nearly flat segment between the Base Cretaceous horizon and the Base Jurassic horizon. Below the Base Jurassic horizon, the gradient steepens down toward the basement horizon.
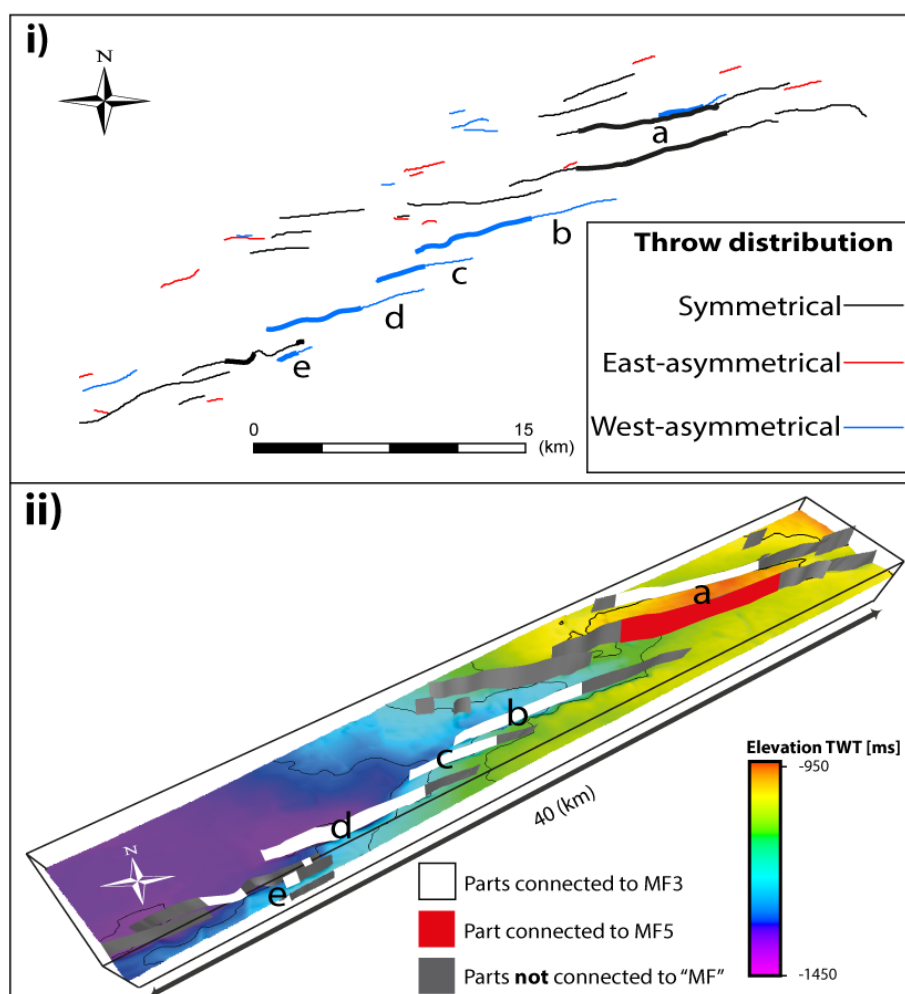
Figure. 7.2: Neogene faults related to MF3 and MF5. Faults located at locations **a-e** are all connected to MF3 or MF5 as upward splays. **(i)** Map view of Neogene faults in cluster group 2. Throw/length profiles are coloured accordingly: east-asymmetrical as red lines, symmetrical as black lines and west-asymmetrical as blue lines. Thicker lines display part(s) of the faults connected to MF3/MF5. **(ii)** 3D-view of the Base Miocene horizon with elevation according to colour scale. Part(s) of Neogene faults connected to MF3 have white fault planes, the part of the Neogene fault connected to MF5 has a red fault plane and parts of Neogene faults not connected to MF3/MF5 have grey fault planes.

The Neogene faults of cluster group 3 are connected to varying degrees with the predating major rift faults of MF6 and MF7. This cluster group shows signs of more extensive faulting compared to the faults of cluster group 2, and has evidence of fault clustering around the southwestern periphery (Fig. 7.3). However, it does exhibit similar characteristics to the Neogene faults connected to MF3, with a stepwise "jump" of MF7-connected en-echelon faults towards the northeast from **c** to **g** (Fig. 7.3ii). The cluster group is also connected to MF7 at **a**, and to MF6 in **b**, with these intersections being located WNW of the faults at **c**. The faults at **a** and **b** represent additional fault sets in the southwest tip of the cluster group, as an addition to the continuous en-echelon bands.

Matching the throw/length distribution profiles to connected parts of faults is not as intuitive as was the case for cluster group 2. Faults at **a** and **b** are intersected in the centre parts and have corresponding symmetrical throw/length profiles. One exception exists, as an east-asymmetrical smaller fault found near **b** with its eastern part connected to MF6. Both larger faults at location **c** and **g** have west-asymmetrical throw/length distribution profiles, and are both mostly connected at depth at the western part of their respective faults. Whereas the three larger faults at locations **d**, **e** and **f**, all have symmetrical throw/length distribution profiles independent of their connections to MF7.

The throw-depth profile of MF6 displays a smaller bell-curve in the upper section, which terminates in the Turonian horizon (Fig. 7.5e). Below the Turonian horizon, the throw values increase modestly towards the Base Jurassic horizon. From the Base Jurassic horizon and into the Top Permian horizon, the throw increases rapidly, before slowing down from the Top Permian horizon and down into the basement horizon. MF7 on the other hand, has a very consistent plot throughout. It comprises a smaller bell-curve in the Neogene, and a straight inclined line from the Base Cretaceous/Turonian horizon and into the basement horizon (Figs. 7.5f, 7.5g and 7.5h).
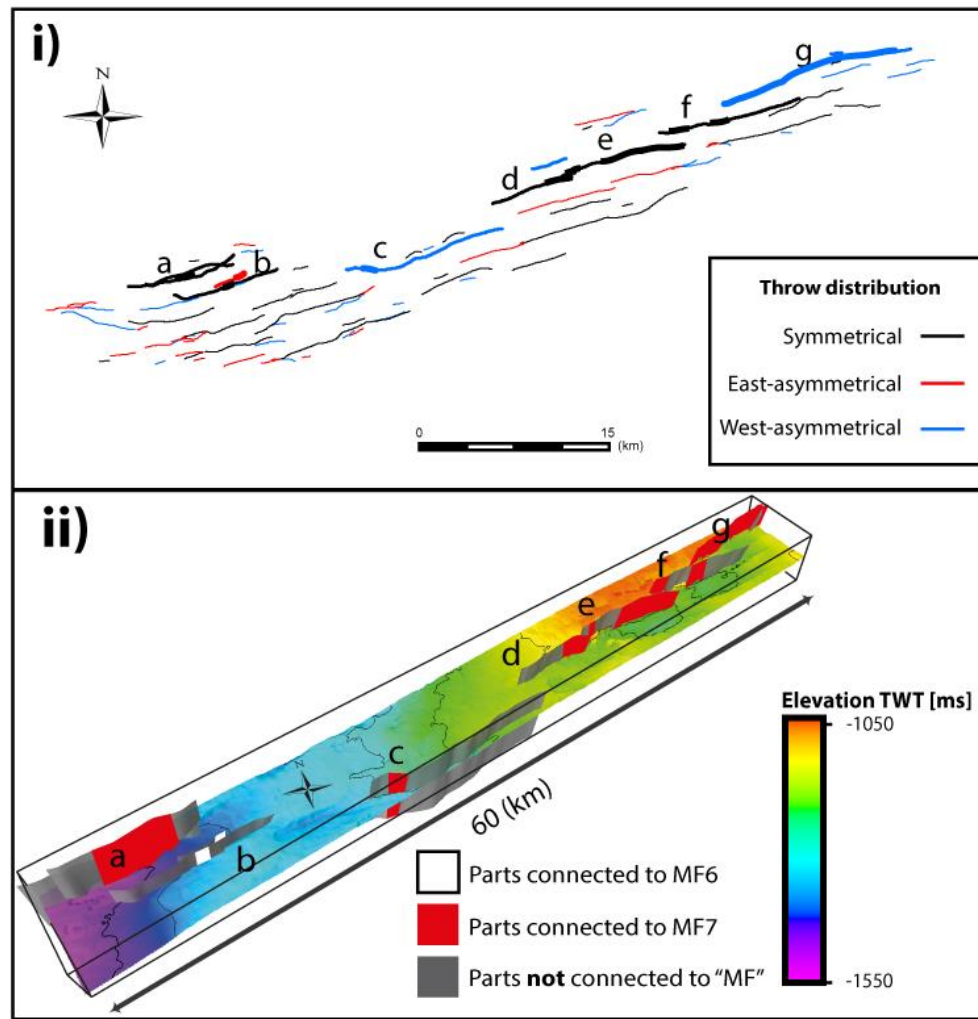
Figure. 7.3: Neogene faults related to MF6 and MF7. Faults located at locations **a-g** are all connected to MF6 or MF7 as upward splays. **(i)** Map view of Neogene faults in cluster group 3. Throw/length profiles are coloured accordingly: east-asymmetrical as red lines, symmetrical as black lines and west-asymmetrical as blue lines. Thicker lines display part(s) of the faults connected to MF6/MF7. **(ii)** 3D-view of the Base Miocene horizon with elevation according to colour scale. Part of Neogene faults connected to MF6 has white fault planes, part(s) of Neogene faults connected to MF7 have red fault planes and parts of Neogene faults not connected to MF6/MF7 have grey fault planes.

In the easternmost part of the interpreted 3D-seismic cube is the faulting related to MF8 and MF9. The faulting in this area forms smaller graben structures between two conjugate fault-sets (Fig. 7.4). These conjugate fault sets each intersects different major rift faults. The S-dipping fault-set interacts with MF8, whilst the N-dipping fault-set interacts with MF9 (Fig. 7.4ii).

The throw/length distribution profiles are consistent with whichever part of the faults are connected to major underlying faults; regardless of which rift fault the Neogene cluster group interacts with (Fig. 7.4i). Neogene faults that are not in direct connection to major rift faults generally display asymmetric throw-distributions towards the centre of faulting.
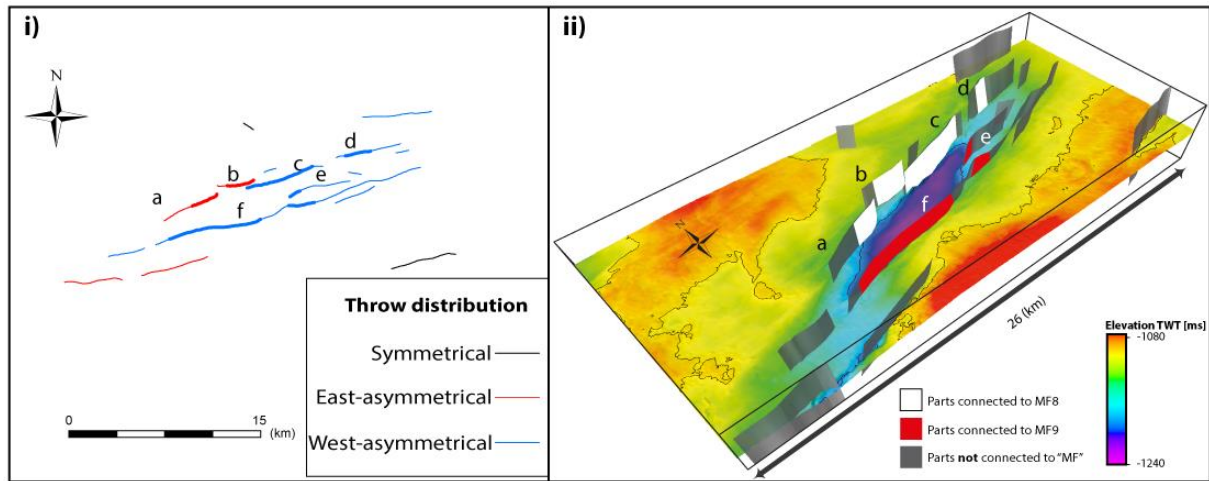
Figure. 7.4: Neogene faults related to MF8 and MF9. Faults located at locations **a-e** are all connected to MF8 or MF9 as upward splays. **(i)** Map view of Neogene faults in cluster group 8. Throw/length profiles are coloured accordingly: east-asymmetrical as red lines, symmetrical as black lines and west-asymmetrical as blue lines. Thicker lines display part(s) of the faults connected to MF8/MF9. **(ii)** 3D-view of the Base Miocene horizon with elevation according to colour scale. Part of Neogene faults connected to MF8 have white fault planes, part(s) of Neogene faults connected to MF9 have red fault planes and parts of Neogene faults not connected to MF8/MF9 have grey fault planes.
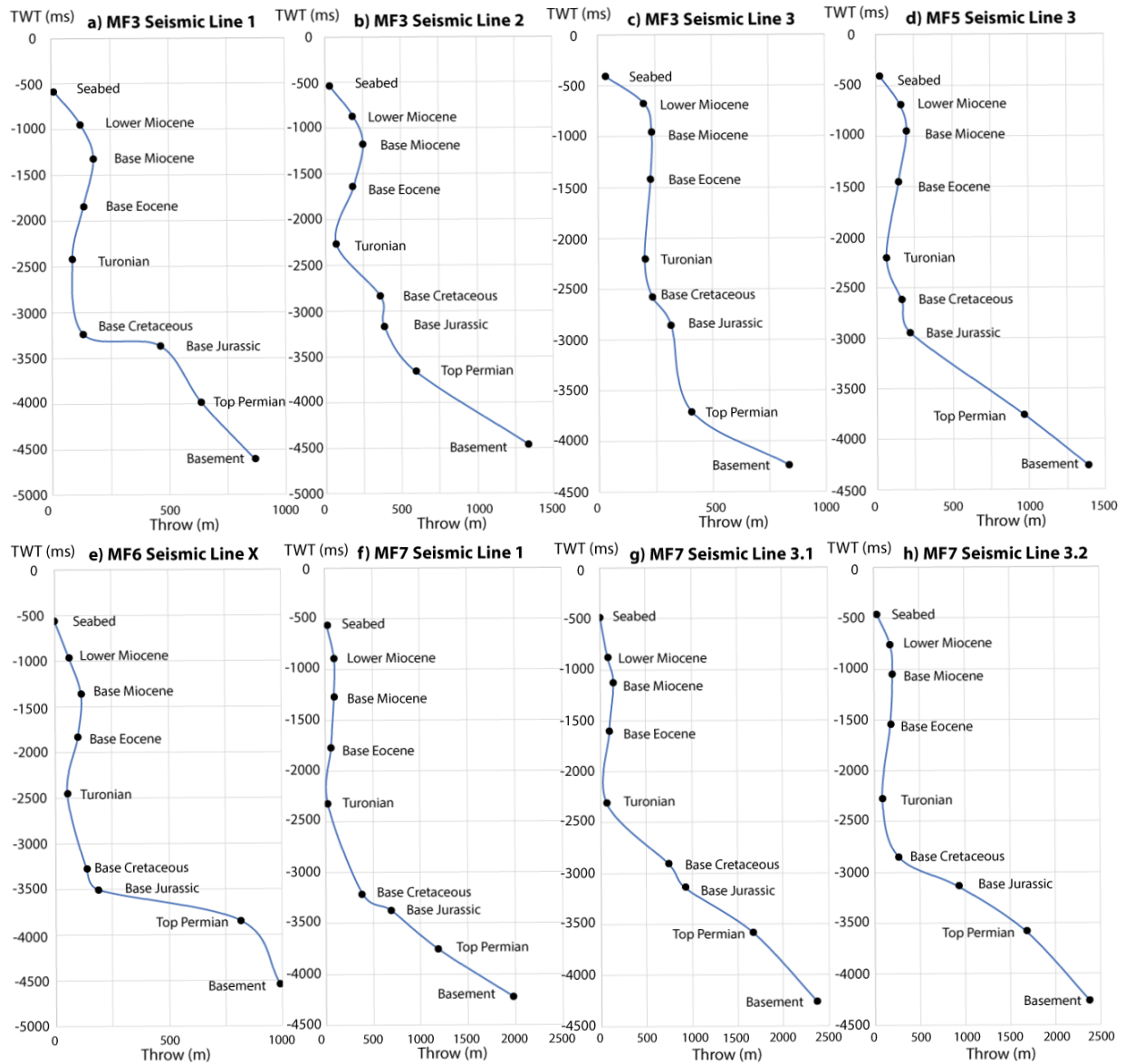
Figure. 7.5: Graph showing fault throw (m) with depth in TWT (ms). **(a):** MF3 fault plane connected to a Neogene fault plane from seismic line 1 (Fig. 5.4). **(b):** MF3 fault plane connected to a Neogene fault plane from seismic line 2 (Fig. 5.5). **(c):** MF3 fault plane connected to a Neogene fault plane from seismic line 3 (Fig. 5.6). **(d):** MF5 fault plane connected to a Neogene fault plane from seismic line 3 (Fig. 5.6). **(e):** MF6 fault plane connected to a Neogene fault plane from seismic line oriented perpendicular to location a (Fig. 7.3). **(f):** MF7 fault plane connected to a Neogene fault plane from seismic line 1 (Fig. 5.4). **(g):** MF7 fault plane connected to the easternmost Neogene fault plane from seismic line 3 (Fig. 5.6). **(h):** MF7 fault plane connected to the westernmost Neogene fault plane from seismic line 3 (Fig. 5.6).

8 Discussion

The results of chapters 5, 6 and 7 are presented to give a detailed structural analysis of the two fault populations in the fault network and interactions/connections between them, mainly focused at the Base Jurassic horizon and the Base Miocene horizon. For the area represented by the two seismic cubes in the Caswell Sub-basin. This chapter will start off with what interactions are present between the two sub-parallel phases of fault network before comparing and contrasting with examples where the two phases of fault network are oblique to one another (8.1). Next, I discuss the distribution of strain with a particular focus on controlling factors of strain localisation during the development of the Neogene fault network (8.2). Furthermore, I discuss the characteristics of the reactivation of the major rift-phase faults (8.3). Finally, the implications of these results for the regional geology are explored (8.4).

8.1 Geometry and interaction between two faulting phases with similar orientation

More than one generation of faults can form in a fault network when an area is exposed to more than one stress regime, where the initially developed fault population can actively influence later developed fault populations by creating local stress perturbations and weakness zones. In my study area, there are two generations of faulting interacting both kinematically and geometrically, with major underlying rift faults (with an overall orientation of ~60 degrees' (Fig. 6.2c)) influencing the development of later Neogene faulting (with an overall orientation of ~70 degrees' (Fig. 6.2a)). This is characterised by similar population characteristics, such as fault trends and overlapping distributions for maximum length vs maximum throw (Fig. 6.4). Furthermore, the spatial arrangement of the Neogene normal faults forms en-echelon faults that clusters above the planes of the larger underlying faults (Fig. 8.3). These Neogene faults are often oriented in bands of faulting consisting of faults with matching dip-directions to the major fault in its footwall, and a band of conjugate faults with opposite dips in its hanging wall (Figs. 6.1a and b). The fault populations are kinematically coherent with cumulative throw-peaks for the Neogene faults that match throw-peaks exhibited by major faults in multiple areas (Figs. 6.6, 6.7 and 6.8). Often there is a hard link forming between the two populations at the throw-peaks, which is visible in several areas within the fault network (e.g. Fig. Cross-sections). At these connected zones, the major underlying faults splay upwards with a rotation through the

Early Cretaceous sequence to dip-link with the Neogene faulting (Fig. 8.1). The fault planes of the partially connected Neogene faults continue laterally in one or both directions.

Such kinematic and geometric linkage between two fault populations described in my study is also observed in the Gulf of Suez, Egypt, investigated by Jackson and Rotevatn (2013). Where two fault populations with same overall orientation, are positioned at two different elevations, with a larger fault below and a cluster of multiple faults in coherence above. These two fault populations have initially developed with only kinematic interaction, with a salt layer separating a larger underlying fault from several smaller faults in the upper layer. During the later deformation history segments of faults from the two fault populations has hard linked. Resulting in a fault plane that has characteristics very much similar to fault planes within my study, with one through-going fault plane at depth that is hard-linked to smaller geometrically independent faults above. Another area that displays similar kinematics and geometries between two fault populations is northeast of the study area at the Sahul Platform in the Bonaparte Basin. Frankowicz and McClay (2010) investigated this area and discovered the same characteristics between two fault populations as is in the Caswell Sub-basin. This includes two fault populations at differing elevations, with a slight difference in orientation, creating connections by upward splaying and en-echelon faulting in the upper fault population. The only difference to this study is the presence of more than two fault populations, however, the interactions between them are much the same.

Fault interactions within the two fault populations in the study area are in big contrast to interactions experienced in networks with two obliquely oriented extensional phases. Such fault networks are demonstrated and investigated in analogue models by Henza *et al.* (2010, 2011), at Milne Point by Nixon *et al.* (2014) and at Horda Platform by Duffy *et al.* (2015) to mention a few. These networks can have different fault populations that interact, just as within this fault network, but with more complex interactions whereby second-phase faulting can form cross-cutting and abutting relationships with first-phase faulting. As a result, second-phase faulting commonly exhibits inhibited fault propagation, which is in contrast to my study area that features freely propagating faults that overlap, forming elongated fault systems with en-echelon oriented faults, relay ramps and segment linkage (Figs. 7.1 and 8.3).
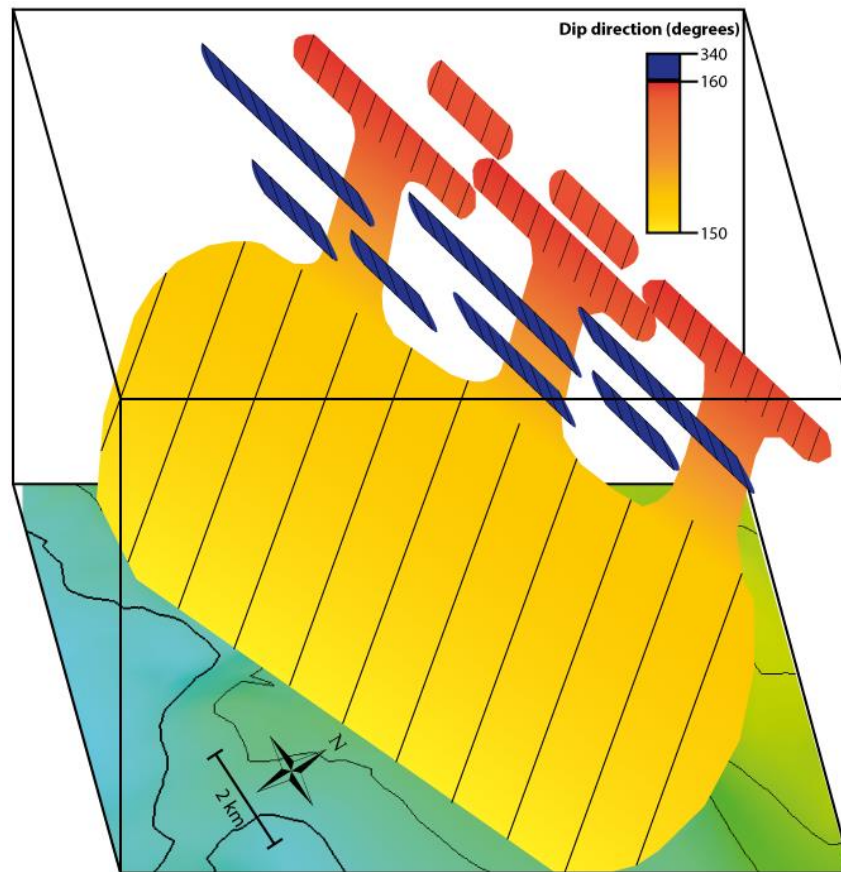
Figure. 8.1: Schematic 3D-sketch of a major rift fault plane (yellow) with a rotation in fault orientation through the dip-linkage with the en-echelon Neogene faulting (red), conjugated fault set in the hanging wall of the major rift fault (blue). Orientations are according to colour scale.

8.2 Strain Localisation

Fault networks can have an overall spatial distribution in faulting and throw that is either heterogeneous or homogeneous, with respectively randomly or equally spaced faults and throws. In my study, the Neogene fault population is present mostly within SW-NE-trending cluster groups (Fig. 6.1f), spatially above major rift faults (Fig. 6.1e). These clustering groups are particularly noticeable in the density plot (Fig. 5.8), which generates bulls-eyes with higher intensity following the trend of the major rift faults. However, overall the Neogene fault population is distributed across the study area, resulting in a homogeneous distribution in the spatial heterogeneity plots for both throw and fault frequency (Fig. 6.5). This is in agreement with the size-frequency distribution plots (Fig. 6.3), which show a negative exponential size distribution that further suggests a more distributed fault population (Gross *et al*., 1997; Soliva and Schulz, 2008). Ultimately, this indicates that the fault population has a more narrow range

in fault sizes than a power-law distribution indicating absence of dominant large faults within the population.

The major rift faults show a variation in throw along strike of the fault, with bell-shaped diagrams and asymmetrical shapes. Most of the peaks in throw along major rift faults are reflected as peaks in the cumulative throw profiles of the Neogene fault groups (Figs. 6.6, 6.7 and 6.8). These cumulative throw-peaks within the Neogene faulting have a trend of being located in areas with lower fault frequencies. This suggests localisation of strain within a small section of faults above the zone where the major rift fault display high throw values. In contrast, zones with smaller throw values in the lower fault population have associated small throw values distributed on several faults in the Neogene section. This corresponds somewhat to Baudon and Cartwright, (2008b), where an underlying fault population in the offshore Brazil had high throw values at similar locations as the overlying fault population. However, these faults were connected, and whether the faults became connected due to the high throw values or whether they accumulated the high throw values due to connection is unknown. In either case, the pre-existing structures have influenced the distribution of throw and faulting in the overlying fault population resulting in strain localisation.

By comparing this fault network to a fault network with obliquely oriented fault populations, it is easier to get a grasp of the fault distribution. For instance, the fault network at East Pennines Coalfield UK has homogeneously distributed faulting among two fault populations, orientated NW and NE. Within each population strain is localised, but independent of the other fault population (Bailey *et al*., 2005). In contrast the Neogene fault population in my study is organised in clusters above the major rift faults that are therefore localising the deformation (Fig. 8.3). This has previously been proposed by Etheridge *et al*. (1991), that the Neogene faulting in Browse Basin has localised along pre-existing zones of weakness, which have later been stated in papers by Harrowfield *et al*. (2003) and Keep *et al*. (2007).

8.3 Reactivation

The time-thickness maps display syn-rift activity through Paleozoic and Mesozoic (Fig. 5.7), with varying degrees of activity on all the major faults. Hence, some of the faults display continuous activity at all mapped time-intervals (e.g. MF7 and MF12), while a few are tectonic silent in parts of the mapped time-intervals (e.g. MF3 and MF15). Permian (Fig. 5.7a) and

Triassic (Fig. 5.7b) show clear thickening packages in hanging walls maintaining larger variations in thickness contrasts between the hanging wall and footwall. These growth packages can be seen thickening in the hanging wall towards fault planes, with variations in thickening on each fault in each time-span (Fig. Cross-sections). Jurassic (Fig. 5.7c) and Early Cretaceous (Fig. 5.7d) display the same, only to a less extent, generating some smaller variations in thickness contrasts between the hanging-wall and footwall. Implying that most major rift faults have been partly active in all following time-spans after initiation in the Carboniferous/Permian, with variations in magnitude to different time-periods. The major faults have also been reactivated in the Neogene, resulting in interaction between the two fault populations.

There are two known mechanisms causing connection between two fault populations at different elevations. Either by reactivating the deeper lying fault-set or by dip-propagation of the upper fault set (Baudon and Cartwright, 2008b). From the throw-depth profiles in figure 7.5, it is possible to make some assumptions on the growth, interaction and reactivation pattern between the two fault populations. Hongxing and Anderson (2007) have interpreted throw-depth profiles, and reason that a growth fault will have a profile with an inclined straight line that decreases with time, which changes to a vertical line when not active. A composite fault will have highest throw values at the nucleation point, and decreasing values downwards in the post-depositional sequence and upwards in the syn-depositional sequence, creating a bell-curve (e.g. Baudon and Cartwright, 2008a). All profiles in my study possess an overall straight inclined line below the Base Cretaceous/Base Jurassic horizon, separated from a bell-curve in the Cenozoic seismic-interval by a throw minimum at the Turonian horizon. This suggests that the major rift faults developed as growth faults with variations in activity into the Jurassic/Cretaceous, and up to the Turonian horizon in some examples (Figs. 7.5 b, d, f and g). Thus, instances of continuous growth to Turonian (e.g. Figs. 7.5f and g) and growth with breaks in activity (e.g. Figs. 7.5b and d). Moreover, the connected Neogene faults initiated as independent faults before linking at depth with the reactivated pre-existing faults, as every plot have some degree of decrease in throw from the Base Miocene horizon to the Turonian horizon (Fig. 7.5). This is similar to profiles collected from Suez Rift, Egypt, presented by Jackson and Rotevatn (2013) and from the Egersund Basin, Norwegian North Sea, presented by Tvedt *et al*. (2013). Where two fault populations nucleated in isolation from each other, producing profiles with throw minimum where the two fault populations connect. In my study MF5 is an excellent example showing that only connecting rift faults propagates beyond the Turonian horizon. As it splays into two fault planes through the Base Jurassic horizon, where only the splay that

connects to a Neogene fault penetrates the Turonian horizon (Figs. 5.6 and 7.5d). Furthermore, the throw-depth profiles possess explicit individual differences for each plot, with especially noticeable variations in throw at the Turonian horizon. For instance, MF3 in cross-section 2 (Fig. 5.5) has two throw-peaks barely connected, separated by throw minima at the Turonian horizon (Fig. 7.5b). Whereas for MF3 in cross-section 3 (Fig. 5.6), the two throw-peaks are scarcely separable by a slightly smaller throw at the Turonian horizon, forming a nearly vertical line (Fig. 7.5c). A likely solution is that as the two fault populations connect, their overall throw-depth profile equilibrates with time (Fig. 8.2). This equilibrating effect has reached different stages on each of the faults, where MF3 possesses a throw-profile that is more equilibrated than the others (Fig. 7.5c). I suggest from what is already discussed that there is a combination of both connection mechanisms in all investigated examples. Thus, the two fault populations developed in kinematical connection and linked during the imposed extensional regime in Miocene, by reactivation of major rift faults accompanied by downward propagation of Neogene faults (Fig. 8.3). However, there are possible variations in favoured mechanism, displayed in the throw-depth plots. For instance has MF7, which is the largest interpreted fault in the seismic cube, throw-profiles suggesting nearly continuous growth up to the Turonian horizon before connecting with Neogene faulting (Figs. 7.5f and g). Whereas MF3, has profiles suggesting a more substantial fault growth during the Neogene and episodes of reactivation on the major rift fault (Figs. 7.5a, b and c).
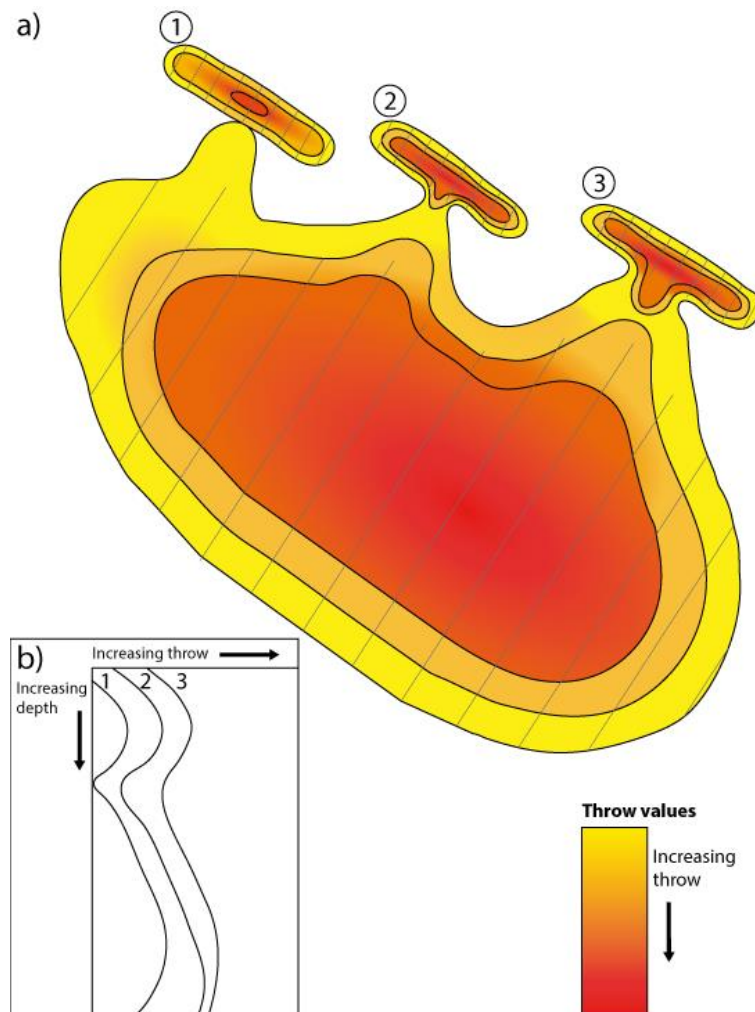
Figure. 8.2: Displaying how a throw-depth plot equilibrates with increasing degree of hard-linkage between the two fault populations. **(a)** Schematic 3D-plot of a fault plane to a major rift fault, with three fault planes to Neogene faults located above in a varying degree of interaction. 1. The two fault populations are barely hard-linked. 2 and 3. Have increasing degree of geometric connection between the two fault populations. **(b)** Belonging Throw-depth plot to the three fault interactions numbered in (a).

Baudon and Cartwright (2008b) from offshore Brazil and Frankowicz and McClay (2010) from the Bonaparte Basin show evidence that reactivation of underlying faults can occur at separate segments instead of whole fault planes. They state four main factors for targeted faulting, preferential orientation, higher throw values, segmentation of the pre-existing population and basal tip-line geometry assciated with a detachment. Within my study, there seems to be a connection between the orientation and high throws and the reactivation of major rift faults. At places where the major rift faults have throw values exceeding 500 meters at the Base Jurassic horizon (Fig. 6.1c), they appear to connect with segments of Neogene faults through the Turonian horizon (Fig. 5.2d). This is the case for MF2, MF5 and MF7, which all have fault planes accumulating more than 500 meters throw. These high throws are more likely to be a

contributing factor to the linkage, rather than a result of the linkage. Because of the fitting trend between the Base Jurassic horizon, the Top Permian horizon and the basement horizon in the throw-depth profile (Fig. 7.5). Same case is for the high throw values visible in the connected Neogene faults, based on the fact that these faults have a symmetric bell-curve with throw maximum at the Base Miocene horizon in the throw-depth plot that extends down to the Turonian horizon (Fig. 7.5).

The link between the two populations is reflected in the greater throw values where the Neogene faults are partially connected to reactivated faults at depth (e.g. Figs. 7.2, 7.3 and 7.4). There also appears to be a kinematic link between reactivation of major rift faults and Neogene faults with asymmetric throw-length profiles. Hence, faults at the Base Miocene horizon have highest throws in the segments where faults are connected at depth to older major rift faults producing asymmetric throw profiles (e.g. Figs. 7.2, 7.3 and 7.4). However, there are a few exceptions to this trend, with symmetrical throw-length plots independent of connection with a major rift fault. For group 3, the larger symmetrical fault at location **a** (Fig. 7.2) is the only fault showing a throw-length plot independent of the connection and has a throw-depth profile that is far more equilibrated compared to the other profiles (Fig. 7.5c). A possible explanation is that the Neogene fault has continued to propagate horizontally after connection and equilibrate the throw-length plot towards a symmetrical shape, and therefore do not own an asymmetrical shape towards the connection point.

8.4 Implications for the Regional Geology

The structures below the Neogene sequences within the Caswell Sub-basin is commercially less known than adjacent sub-basins. Previous interpretations of structures and stratigraphy for Mesozoic and Paleozoic structures in the Caswell Sub-basin have been based on the use of 2D-seismic data (Table. 4.1), with Symonds *et al*. (1994) using BBS and Struckemeyer *et al*. (1998) using BBHR. Struckmeyer *et al*. (1998) propose that the deeper architecture in the Caswell Sub-basin is dominated by three large NE-trending Paleozoic faults: Bassett-, Brewster- and Caswell Faults. The Paleozoic fault map (Fig. 3.2) proposed by Struckmeyer *et al*. (1998) has been the basis for later research that focuses on faulting within the Neogene (e.g. Keep *et al*., 2007; Keep and Harrowfield, 2008), where the interaction between the two fault populations is referred to as oblique. Based on the proposed Paleozoic fault map the Bassett Fault originally crossed through the eastern part of the 3-D survey area in this study, however, my results show a number

of faults trending closer to ENE, rather than NE. Hence, the Bassett Fault may be a resulting interpretation from tying incorrect fault planes together, since they only had 2D-seismic with a broad line spacing (Fig. 4.1). My results question the existence of the Bassett fault, as well as the overall orientation proposed for Paleozoic faulting in this part of the Caswell Sub-basin. The new overall orientation for Paleozoic-Mesozoic faulting gives a new understanding on how the basement structures actively constrain the faulting within the Neogene sequence.

To the south in the Browse Basin, in the Barcoo Sub-basin the structures are quite different to my study, however, the structures are under strong influence by reactivated extensional faults oriented NE, in strata below (Keep and Moss, 2000; Keep *et al*., 2000). Locations with greater similarities in geometry are present in sub-basins within the Northern Bonaparte Basin rather than within the Browse Basin. Struckmeyer *et al*. (1998) draw parallels between one of these basins (Vulcan Sub-basin) and the northern part of the Caswell Sub-basin, regarding normal-fault populations within the Neogene sequence. These two sub-basins have a similar architecture with en-echelon faulting above reactivated pre-existing faulting (Woods, 1992). However, the orientation for the two fault populations in Vulcan Sub-basin is NE-SW (Meyer *et al*., 2002), which is a small anti-clockwise rotation compared to the fault populations in this study. Meyer *et al*. (2002) experience fast establishment of faults with an orientation sub-parallel to pre-existing Mesozoic faults and argue that the rapid formation could be due to reactivation of these underlying faults. The Neogene faults develop with a progressively concentrated extension on larger faults, which is similar to the fault population in the Caswell, sub-basin, with Neogene faults progressively accommodating extension and connecting to underlying faults in the same spatial location. In the Sahul Platform of the Bonaparte Basin Frankowicz and McClay (2010) suggest an overall orientation for Jurassic-Cretaceous faulting to be between E-W and ENE-WSW, with en-echelon NE-trending Neogene faults above generated by reactivation of the underlying fault population. These are all elements that fit well with observations concluded from this thesis. Hence, the imposed stress-fields must have been similar for the Caswell Sub-basin and the northwestern part of Sahul Platform. It is important to take into account that the fault network in the Bonaparte Basin is much more complex, with more than two fault populations with variations in orientation. However, the seismic data used in this survey do not have high enough resolution to depict possible smaller faulting with a different orientation below the Base Cretaceous horizon. Overall, the examples provided here emphasises the importance of pre-existing structures during formation of Cenozoic structures in the Browse Basin and the Bonaparte Basin.

Regarding the fault activity interpreted from time-thickness maps, the study area is located on the margin of the basin and therefore does not fit the overall phases of deformation in the main part of the Browse Basin. For example, the first thermal subsidence phase from Late Permian into Late Triassic proposed by Struckmeyer *et al.* (1998). My presented time-thickness map for the Triassic shows syn-rifting on several faults, and very little evidence of sag (Fig. 5.7b). The time-thickness map from Early Cretaceous show larger degrees of thermal sag with a general thickening towards the S, but the major faults do additionally exhibit some activity (Fig. 5.7d). This southward thickening trend is not visible on any of the other time-thickness maps (Fig. 5.7). Therefore the structural evolution framework from Struckmeyer *et al.* (1998) and Blevin *et al.* (1997, 1998) is possibly more accurate for the central parts of the Browse Basin, and that thermal sag is more basinward accompanied with faulting in the edges (e.g. this study area).

The fault model presented in this thesis (Fig. 8.3) presents a wider spectre of larger basement faults (Fig. 5.1) than presented in fault maps by Symonds *et al.* (1994) and Struckmeyer *et al.* (1998). Furthermore, the reactivation of the major rift faults and the kinematic/geometric link between the two fault populations are possibly more extensive than originally thought. As a continuous fault plane might act as a pathway for hydrocarbons, the results presented in this study are of importance to petroleum exploration of the NW Australian shelf, where fault reactivation and geometric fault connections between two fault phases are profound. Reactivation of major rift faults and corresponding vertical dip-linkage to faulting within the Neogene time-section can cause a significant effect on fault sealing characteristics and trap integrity, resulting in possible remigration of hydrocarbons (Hooper, 1991; Wiprut and Zoback, 2000; Gartrell *et al.*, 2006) and alteration of spill-points during events of reactivation (Horstad and Larter, 1998). For example, in the Laminaria High in the Bonaparte Basin Langhi *et al.* (2000) identify upward migrations of hydrocarbons where sub-faults reactivate at several stages and a few faults connect with Neogene supra fault population.
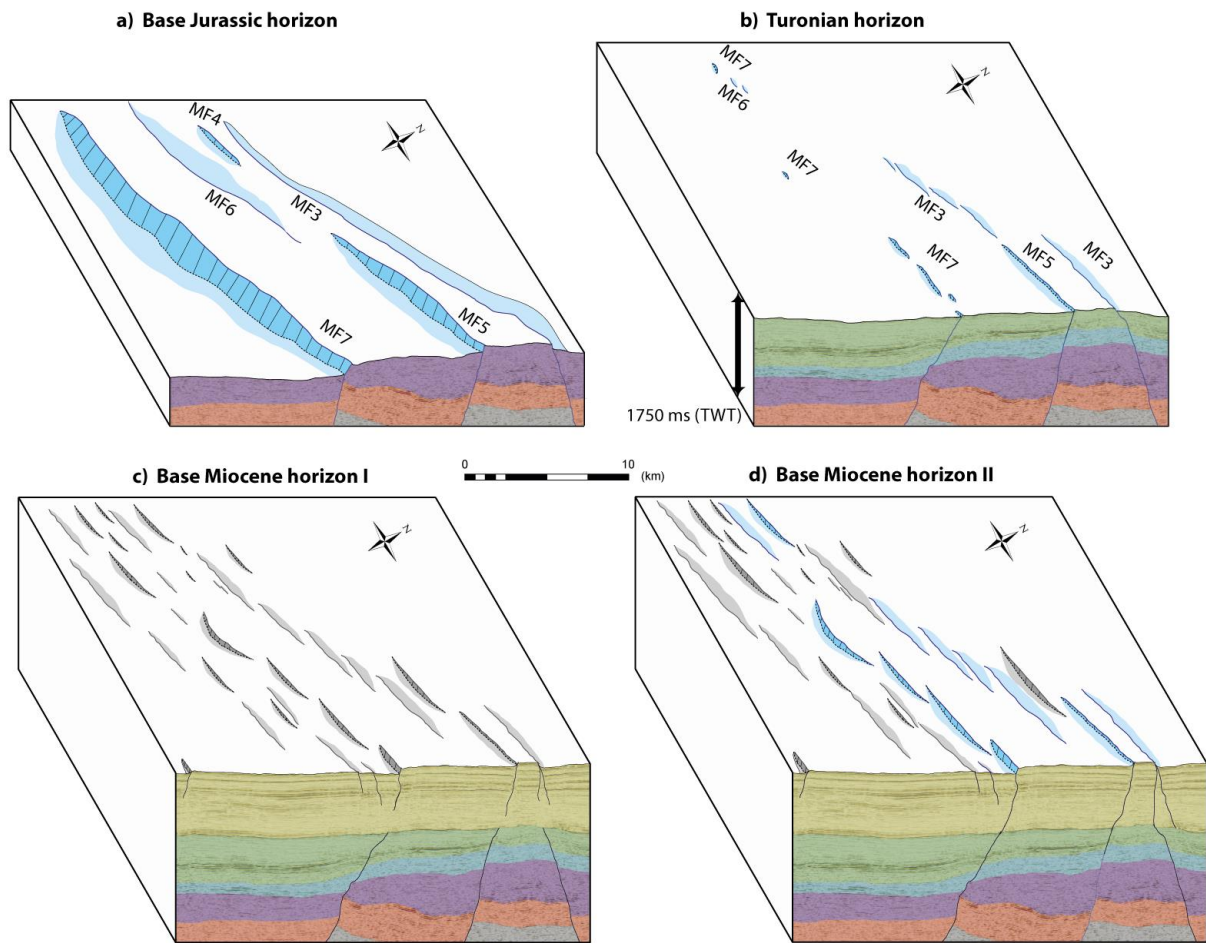
Figure. 8.3: Schematic model displaying cluster group 2 and 3, with eventually geometric connections between major faults at the Base Jurassic horizon and faults located at the Base Miocene horizon, through the Turonian horizon. Additionally, the fault evolution at the Base Miocene horizon. Faults with a geometric connection through the three horizons are marked with blue, whereas grey faults are geometric isolated faults. **(a)** Major faults cutting the Base Jurassic horizon labelled with acronyms. **(b)** Major faults cutting the Turonian horizon. Segments connected to what major fault is labelled with acronyms on the Turonian horizon. **(c)** The first step of fault development at the Base Miocene horizon, with solitary kinematical linkage between the two fault populations. **(d)** The Base Miocene horizon at present. Some faults have formed geometric-linkage with major faults by fault reactivation and dip-propagation. Connection to which major fault is displayed at **(b)**.

9 Conclusions and further work

9.1 Conclusions

In this study, a structural model has been generated by the use of 2-D and 3-D seismic reflection data from a normal fault network from the Browse Basin, NW Australia. To gain better understanding of interactions in normal fault networks and the influence of pre-existing structures on fault network growth and development. This study includes a characterisation of interactions and distribution of strain within a fault network with the use of fault attribute maps, throw-length profiles, cumulative plots and heterogeneity analysis. In addition, a fault model for fault reactivation and growth by integrating time-thickness maps with throw-depth profiles. The conclusions drawn from the results can be divided into two sections; general characteristics and interaction between the fault populations, and fault activity and reactivation.

9.1.1 General characteristics and interaction between the fault populations

The network comprises two kinematically coherent sub-linear normal fault populations, with a Neogene fault population and an underlying fault population comprising Paleozoic-Mesozoic major rift faults. Hence, the two fault populations possess similar characteristics. The results show that:

1. Palaeozoic-Mesozoic rift faults are oriented with an average orientation of ~60 degrees', setting up horst/graben structures with a decreasing presence up to and including the Turonian horizon. This represents a clockwise rotation in orientation from the originally interpreted NE orientation of the Paleozoic-Mesozoic faults in the area.

2. Neogene fault population related to reactivation/inversion in the Miocene have an average orientation of ~70 degrees' as en-echelon fault arrays. Implying a similar stress field with a slight rotation, generating the two fault populations.

3. Fault relationships are dominated by individual faults, overlapping faults, linked faults and relay ramps. This is distinguishable from a fault network with two extensional phases obliquely oriented on each other where cross-cutting relations, such as abutting faults and trailing segments occur.

4. Neogene fault frequency and throw are overall homogeneously distributed throughout the fault network, although the throw is consistently less homogeneous than the frequency.

Despite this the faults form elongated cluster-groups above Palaeozoic-Mesozoic rift faults, confined mostly within the Neogene package.

5. There is a spatial coherence between high throws exhibited by the two fault populations at the Base Jurassic horizon and the Base Miocene horizon, respectively, usually at places where the two populations are in geometric connection.

6. High throw-peaks in the Neogene fault population is localised in parts with less fault frequency, and the low throw values are distributed in parts with higher fault frequency. This is related to high throws and reactivation in the underlying fault population. As well as areas of damage such as tips of underlying faults.

9.1.2 Fault activity and reactivation

The growth activity to the major rift faults and the Neogene faults was investigated together, for the reason to point out activity patterns and characteristics to the dip-linkage. The research show that:

7. The major rift faults display variations in syn-rift activity through the Palaeozoic and Mesozoic, reflected as syn-depositional growth packages in the hanging walls. The Permian and Triassic are seemingly the most active periods with largest thickness contrasts between hanging walls and footwalls. Fault activity in a lower degree is also present in Jurassic and Early Cretaceous in some fault segments. However, a sag event in Cretaceous is the main driver for sediment thickening in the Early Cretaceous sequence. Every major fault shows individual activities in the four mapped time-intervals. Where some shows continuous growth from the Basement to the Turonian and some display periods of tectonic silence.

8. Neogene faulting has nucleated along and above the major rift faults and was probably only kinematically interacting and soft linked to the major rift faults. The underlying major rift faults thus control the preferential localisation of strain within the Neogene sequence by acting as weakness zones preferential for nucleation sites.

9. Throw-depth profiles reflect different stages of linkage between the two fault populations indicating the two fault populations become hard linked through a combination of isolated Neogene faults propagating downwards and major rift faults reactivating with rotating splays propagating upwards. The dominant mechanism is differing for each fault connection.

10. The geometric dip-linkage resulting from dip-propagation and fault reactivation reflect localised high throw values at segments in both fault populations with geometric connection. This results in many cases in throw-length profiles for Neogene faults where the highest throws are located at segments that are linked at depth.

Overall, this study provides a complete fault network analysis, investigating fault distributions and throw distributions within each fault population both horizontally and vertically. Also, interactions with effects caused by the interference between the two fault populations. Hence, that the pre-existing structures can cause variations in throw and localisation within the Neogene fault population. Further, this study supplies additional data proving that parallels can be drawn in structural geometry among the northern Browse Basin and the northern Bonaparte basin. Where both possess en-echelon faulting above reactivated and nearly sub-parallel pre-existing faults. Displaying the importance of how pre-existing structures on a passive margins can actively control structures formed during later imposed stress fields.

9.2 Further work

This is the first attempt to interpret the section below the Cenozoic with the use of 3D-seismic (TQ3D-survey) in the Caswell Sub-basin. It will be a huge benefit if other people make interpretations in the same two seismic cubes. Most beneficial would be to make another detailed interpretation with closer line spacing, to depict structural features that are excluded when interpreting with a broad spacing. Especially if there are any smaller faults with differing orientations terminating in-between the interpreted fault populations in a shorter time-interval.

My interpretation covers only two out of five seismic 3D-cubes constructed during the TQ3D-survey. Interpreting the remaining three seismic cubes will be useful to get a broader picture of the structural geometry. In addition, if the presence of larger Paleozoic-Mesozoic faults in my study area is a dominant factor for the nucleation of Neogene faulting. Because faulting within the Neogene strata is more extensive in the study area for this thesis than in the three remaining seismic-cubes to the south.

Make a more thorough analysis with throw-depth profiles, for unconnected, geometrically connected and kinematically connected faults. These should include more horizons in the plot

to depict details not visual in the profiles presented in this study. Additionally, with a closer spacing along the strike to the fault, to display variations along the fault plane and not only between individual faults.

Collection of higher quality data will make it considerably easier to interpret the deeper sections in the northern Caswell Sub-basin. Will improve the ability to pick out smaller faults and basement deformation related to initial rifting. As the fault resolution in this study was 70 meters for faults cutting the Base Jurassic horizon. Eventually, also compare faulting at the margins to basinal structures.

10 References

Aksari, D., Karabulut, H., Özalaybey, S. 2010. Stress interactions of three moderate size earthquakes in Afyon, southwestern Turkey. Tectonophysics 485, 141-153.

Aydin, A. 2000. Fractures, faults, and hydrocarbon entrapment, migration and flow. Marine and Petroleum Geology 17, 797–814.

Bailey, W. R., Walsh, J. J., Manzocchi, T. 2005. Fault populations, strain distribution and basement fault reactivation in the East Pennines Coalfield, UK. Journal of Structural Geology 27, 913–928.

Baillie, P. W., Powell, C. M., Li, Z. X., Ryall, A. M. 1994. The tectonic framework of Western Australia's Neoproterozoic to Recent sedimentary basins. In The sedimentary basins of Western Australia: Proceedings of Petroleum Exploration Society of Australia Symposium 1, 45-62.

Baudon, C., Cartwright, J. 2008a. Early stage evolution of growth faults: 3D seismic insights from the Levant Basin, Eastern Mediterranean. Journal of Structural Geology 30, 888-898.

Baudon, C., Cartwright, J. 2008b. The kinematics of reactivation of normal faults using high resolution throw mapping. Journal of Structural Geology 30, 1072-1084.

Belde, J., Back, S., Reuning, L. 2015. Three-dimensional seismic analysis of sediment waves and related geomorphological features on a carbonate shelf exposed to large amplitude internal waves, Browse Basin region, Australia. Sedimentology 62, 87-109.

Bellahsen, N., Daniel, J.M. 2005. Fault reactivation control on normal fault growth: an experimental study. Journal of Structural Geology 27, 769–780.

Blevin, J. E., Struckmeyer, H. I. M., Boreham, C. J., Cathro, D. L., Sayers, J., Totterdell, J. M. 1997. Browse Basin high resolution study. Interpretation report, North West Shelf, Australia. AGSO Record 38.

Blevin, J. E., Struckmeyer, H. I. M., Cathro, D. L., Totterdell, J. M., Boreham, C. J., Romine, K. K., Sayers, J. 1998. Tectonostratigraphic framework and petroleum systems of the Browse Basin, North West Shelf. In The Sedimentary Basins of Western Australia 2: Proceedings of the Petroleum Exploration Society of Australia Symposium, Perth, 369-395.

Bonini, M., Souriot, T., Boccaletti, M., Brun, J.P. 1997. Successive orthogonal and oblique extension episodes in a rift zone: laboratory experiments with application to the Ethiopian Rift. Tectonics 16, 347– 362.

Bouvier, J. D., Kaars-Sijpesteijn, C. H., Kluesner, D. F., Onyejekwe, C. C., Van der Pal, R. C. 1989. Three-dimensional seismic interpretation and fault sealing investigations, Nun River Field, Nigeria. AAPG Bulletin 73, 1397-1414.

Bradshaw, M. T., Yeates, A. N., Beynon, R. M., Brakel, A. T., Langford, R. P., Totterdell, J. M., Yeung, M. 1988. Palaeogeographic evolution of the North West Shelf region. The North West Shelf Australia, 29-54.

Brune, S. 2014. Evolution of stress and fault patterns in oblique rift systems: 3-D numerical lithospheric-scale experiments from rift to breakup. Geochemistry, Geophysics, Geosystems 15, 3392-3415.

Bull, J. M., Barnes, P. M., Lamarche, G., Sanderson, D. J., Cowie, P. A., Taylor, S. K., Dix, J. K. 2006. High-resolution record of displacement accumulation on an active normal fault: implications for models of slip accumulation during repeated earthquakes. Journal of Structural Geology 28, 1146-1166.

Campbell, I. R., Tait, A. M., Reiser, R. F. 1984. Barrow Island oilfield, revisited. The APPEA Journal 24, 289-298.

Cartwright, J. A., Mansfield, C., Trudgill, B. 1996. The growth of normal faults by segment linkage. Geological Society, London, Special Publications 99, 163-177.

Cartwright, J. A., Trudgill, B. D., Mansfield, C. S. 1995. Fault growth by segment linkage: an explanation for scatter in maximum displacement and trace length data from the Canyonlands Grabens of SE Utah. Journal of Structural Geology 17, 1319- 1326.

Chen, G., Hill, K. C., Hoffman, N., O'Brien, G. W. 2002. Geodynamic evolution of the Vulcan Sub-basin, Timor Sea, northwest Australia: a pre-compression New Guinea analogue?. Australian Journal of Earth Sciences 49, 719-736.

Chou, Y.W. 1999 Tectonic framework, flexural uplift history and structural patterns of flexural extension in western Taiwan foreland basin. National Taiwan University, PhD Thesis.

Contreras, J., Anders, M. H., Scholz, C. H. 2000. Growth of a normal fault system: observations from the Lake Malawi basin of the east African rift. Journal of Structural Geology 22, 159-168.

Cowie, P. A. 1998. A healing–reloading feedback control on the growth rate of seismogenic faults. Journal of Structural Geology 20, 1075-1087.

Cowie, P. A., Gupta, S., Dawers, N. H. 2000. Implications of fault array evolution for synrift depocentre development: insights from a numerical fault growth model. Basin Research 12, 241-261.

Cowie, P.A., Scholz, C.H. 1992. Growth of faults by accumulation of seismic slip. Journal of Geophysical Research 97, 11085–11095.

Curewitz, D., Karson, J. A. 1997. Structural settings of hydrothermal outflow: Fracture permeability maintained by fault propagation and interaction. Journal of Volcanology and Geothermal Research 79, 149-168.

Daly, M. C., Chorowicz, J., Fairhead, J. D. 1989. Rift basin evolution in Africa: the influence of reactivated steep basement shear zones. Geological Society, London, Special Publications 44, 309-334.

Davatzes, N. C., Aydin, A., Eichhubl, P. 2003. Overprinting faulting mechanisms during the development of multiple fault sets in sandstone, Chimney Rock fault array, Utah, USA. Tectonophysics 363, 1-18.

Dawers, N. H., Anders, M. H. 1995. Displacement-length scaling and fault linkage. Journal of Structural Geology 17, 607-614.

Dawers, N. H., Anders, M. H., Scholz, C. H. 1993. Growth of normal faults: Displacement- length scaling. Geology 21, 1107-1110.

Dawers, N. H., Underhill, J. R. 2000. The Role of Fault Interaction and Linkage in Controlling Synrift Stratigraphic Sequences : Late Jurassic, Statfjord East Area, Northern North Sea 1, 45–64.

De Charpal, O., Montradert, L., Guennoc, P., Roberts, D. G. 1978. Rifting, crustal attenuation and subsidence in the Bay of Biscay. Nature 275, 706-711.

Deng, C., Fossen, H., Gawthorpe, R. L., Rotevatn, A., Jackson, C. A., & FazliKhani, H. 2017. Influence of fault reactivation during multiphase rifting: The Oseberg area, northern North Sea rift. Marine and Petroleum Geology.

Dewey, J. F., Burke, K. C. 1973. Tibetan, Variscan, and Precambrian basement reactivation: products of continental collision. The Journal of Geology 81, 683-692.

Dubois, A., Odonne, F., Massonnat, G., Lebourg, T., Fabre, R. 2002. Analogue modelling of fault reactivation: tectonic inversion and oblique remobilisation of grabens. Journal of Structural Geology 24, 1741–1752.

Duffy, O. B., Bell, R. E., Jackson, C. A. L., Gawthorpe, R. L., Whipp, P. S. 2015. Fault growth and interactions in a multiphase rift fault network: Horda Platform, Norwegian North Sea. Journal of Structural Geology 80, 99-119.

Duffy, O. B., Nixon, C. W., Bell, R. E., Jackson, C. A. L., Gawthorpe, R. L., Sanderson, D. J., Whipp, P. S. 2017. The topology of evolving rift fault networks: Single-phase vs multi-phase rifts. Journal of Structural Geology 96, 192-202.

Elliott, R. 1990. Browse Basin. Geology and Mineral Resources of Western Australia: Geological Survey of Western Australia, Memoir 3, 535-547.

Etheridge, M. A., O'Brien, G. W. 1994. Structural and tectonic evolution of the Western Australian margin basin system. PESA Journal 22, 45–63.

Ferrill, D. A., Morris, A. P., McGinnis, R. N. 2009. Crossing conjugate normal faults in field exposures and seismic data. AAPG bulletin 93, 1471-1488.

Fossen, H., Rotevatn, A. 2016. Fault linkage and relay structures in extensional settings. A review. Earth-Science Reviews 154, 14-28.

Frankowicz, E., McClay, K. R. 2010. Extensional fault segmentation and linkages, Bonaparte Basin, outer North West Shelf, Australia. AAPG Bulletin 94, 977–1010.

Færseth, R. B. 1996. Interaction of Permo-Triassic and Jurassic extensional fault-blocks during the development of the northern North Sea. Journal of the Geological Society, London 153, 931–944.

Gartrell, A., Bailey, W. R., Brincat, M. 2006. A new model for assessing trap integrity and oil preservation risks associated with postrift fault reactivation in the Timor Sea. AAPG bulletin 90, 1921-1944.

Gawthorpe, R. L., Leeder, M. R. 2000. Tectono-sedimentary evolution of active extensional basins. Basin Research 12, 195-218.

Giba, M., Walsh, J. J., Nicol, A. 2012. Segmentation and growth of an obliquely reactivated normal fault. Journal of Structural Geology 39, 253-267.

Granier, T. 1985. Origin, damping, and pattern of development of faults in granite. Tectonics 4, 721-737.

Gupta, S., P. A. Cowie, N. H. Dawers, J. R. Underhill. 1998. A mechanism to explain rift-basin subsidence and stratigraphic patterns through fault array evolution: Geology 26, 595-598.

Harrowfield, M., Cunneen, J., Keep, M., Crowe, W. 2003. Early-stage orogenesis in the Timor Sea region, NW Australia. Journal of the Geological Society 160, 991-1001.

Henza, A. A., Withjack, M. O., Schlische, R. W. 2010. Normal-fault development during two phases of non-coaxial extension: An experimental study. Journal of Structural Geology 32, 1656-1667.

Henza, A. A., Withjack, M. O., Schlische, R. W. 2011. How do the properties of a pre-existing normal-fault population influence fault development during a subsequent phase of extension? Journal of Structural Geology 33, 1312-1324.

Henstra, G. A., Rotevatn, A., Gawthorpe, R. L., Ravnås, R. 2015. Evolution of a major segmented normal fault during multiphase rifting: The origin of plan-view zigzag geometry. Journal of Structural Geology 74, 45-63.

Hongxing, G., Anderson, J. K. 2007. Fault throw profile and kinematics of Normal fault: conceptual models and geologic examples. Geol. J. China Univ 13, 75-88.

Hooper, E. C. D. 1991. Fluid migration along growth faults in compacting sediments. Journal of Petroleum Geology 14, 161-180.

Hocking, R. M., Mory, A. J., Williams, I. R. 1994. An atlas of Neoproterozoic and Phanerozoic basins of Western Australia. In The Sedimentary Basins of Western Australia: Proceedings of the Petroleum Exploration Society of Australia Symposium, Perth, 21-43.

Holdsworth, R. E., Butler, C. A., Roberts, A. M. 1997. The recognition of reactivation during continental deformation. Journal of the Geological Society 154, 73-78.

Horstad, I., Larter, S. 1997. Petroleum migration, alteration, and remigration within Troll field, Norwegian North Sea. AAPG bulletin 81, 222-248.

Jackson, C. A. L., Rotevatn, A. 2013. 3D seismic analysis of the structure and evolution of a salt-influenced normal fault zone: a test of competing fault growth models. Journal of Structural Geology 54, 215-234.

Keep, M., Clough, M., Langhi, L., Moss, S. J. 2002. Neogene tectonic and structural evolution of the Timor Sea region, NW Australia. In Sedimentary basins of Western Australia: Petroleum Exploration Society of Australia Symposium Proceedings 3, 341-353.

Keep, M., Harrowfield, M. 2008. Elastic flexure and distributed deformation along Australia's North West Shelf: Neogene tectonics of the Bonaparte and Browse basins. Geological Society, London, Special Publications 306, 185-200.

Keep, M., Harrowfield, M., Crowe, W. 2007. The Neogene tectonic history of the North West Shelf, Australia. Exploration Geophysics 38, 151-174.

Keep, M., McClay, K.R. 1997. Analogue modelling of multiphase rift systems. Tectonophysics 273, 239-270.

Keep, M., Moss, S. J. 2000. Basement reactivation and control of Neogene structures in the outer Browse Basin, North West Shelf. Exploration Geophysics 31, 424-432.

Kelly, P.G., Peacock, D.C.P., Sanderson, D.J., McGurk, A.C. 1999. Selective reverse-reactivation of normal faults, and deformation around reverse-reactivated faults in the Mesozoic of the Somerset coast. Journal of Structural Geology 21, 493–509.

Kerrich, R. 1986. Fluid infiltration into fault zones: chemical, isotopic, and mechanical effects. Pure and applied geophysics 124, 225-268.

Kim, Y. S., Andrews, J. R., Sanderson, D. J. 2001. Reactivated strike–slip faults: examples from north Cornwall, UK. Tectonophysics 340, 173-194.

King, G. 1986. Speculations on the geometry of the initiation and termination processes of earthquake rupture and its relation to morphology and geological structure. Pure and Applied Geophysics 124, 567–585.

Krantz, R.W. 1991. Measurements of friction coefficients and cohesion for faulting and fault reactivation in laboratory models using sand and sand mixtures. Tectonophysics 188, 203–207.

Langhi, L., Zhang, Y., Gartrell, A., Underschultz, J., Dewhurst, D. 2010. Evaluating hydrocarbon trap integrity during fault reactivation using geomechanical three-dimensional modeling: An example from the Timor Sea, Australia. AAPG bulletin 94, 567-591.

Larsen, P. H. 1988. Relay structures in a Lower Permian basement-involved extension system, East Greenland. Journal of Structural Geology 10, 3-8.

Lavering, I.H., Pain, L. 1991. Australian Petroleum Accumulations Report 7: Browse Basin. Department of Primary Industries and Energy, Bureau of Mineral Resources, Geology and Geophysics, Australian Government Publishing Service Canberra 1991, 1–45.

Letouzey, J., Werner, P., Marty, A. 1990. Fault reactivation and structural inversion. Backarc and intraplate compressive deformations. Example of the eastern Sunda shelf (Indonesia). Tectonophysics 183, 341-362.

Leveille, G. P., Knipe, R., More, C., Ellis, D., Dudley, G., Jones, G., Allinson, G. 1997. Compartmentalization of Rotliegendes gas reservoirs by sealing faults, Jupiter Fields area, southern North Sea. Geological Society, London, Special Publications 123, 87-104.

Maerten, L., Willemse, E. J., Pollard, D. D., Rawnsley, K. 1999. Slip distributions on intersecting normal faults. Journal of Structural Geology 21, 259-272.

Maerten, L., Gillespie, P., Pollard, D. D. 2002. Effects of local stress perturbation on secondary fault development. Journal of Structural Geology 24, 145-153.

Manzocchi, T., Walsh, J.J., Nicol, A. 2006. Displacement accumulation from earthquakes on isolated normal faults. Journal of Structural Geology 28, 1685– 1693.

McClay, K. R., Dooley, T., Whitehouse, P., Mills, M. 2002. 4-D evolution of rift systems: Insights from scaled physical models. AAPG bulletin 86, 935-960.

McGrath, A. G., Davison, I. 1995. Damage zone geometry around fault tips. Journal of Structural Geology 17, 1011-1024.

McLeod, A. E., Underhill, J. R. 2000. The propagation and linkage of normal faults: insights from the Strathspey–Brent–Statfjord fault array, northern North Sea. Basin Research 12, 263-284.

Meyer, V., Nicol, A., Childs, C., Walsh, J. J., Watterson, J. 2002. Progressive localisation of strain during the evolution of a normal fault population. Journal of Structural Geology 24, 1215–1231.

Mouslopoulou, V., Walsh, J.J., Nicol, A. 2009. Fault displacement rates on a range of timescales. Earth and Planetary Science Letters 278, 186–197.

Morley, C.K., Haranya, C., Phoosongsee, W., Pongwapee, S., Kornsawan, A., Wonganan, N. 2004. Activation of rift oblique and rift parallel pre-existing fabrics during extension and their effect on deformation style; examples from the rifts of Thailand. Journal of Structural Geology 26, 1803-1829.

Morley, C. K. 2007. Variations in late Cenozoic–Recent strike-slip and oblique-extensional geometries, within Indochina: The influence of pre-existing fabrics. Journal of Structural Geology 29, 36-58.

Muraoka, H., Kamata, H. 1983. Displacement distribution along minor fault traces. Journal of Structural Geology 5, 483-495.

Nicol, A., Walsh, J., Berryman, K., Nodder, S. 2005. Growth of a normal fault by the accumulation of slip over millions of years. Journal of Structural Geology 27, 327-342.

Nicol, A., Walsh, J. J., Villamor, P., Seebeck, H., Berryman, K. R. 2010. Normal fault interactions, paleoearthquakes and growth in an active rift. Journal of Structural Geology 32, 1101-1113.

Nicol, A., Walsh, J. J., Watterson, J., Bretan, P. G. 1995. Three-dimensional geometry and growth of conjugate normal faults. Journal of Structural Geology 17, 847851-849862.

Nixon, C. W., Sanderson, D. J., Dee, S. J., Bull, J. M., Humphreys, R. J., Swanson, M. H. 2014. Fault interactions and reactivation within a normal-fault network at Milne Point, Alaska. AAPG Bulletin 98, 2081-2107.

Norton, D., Knapp, R. 1977. Transport phenomena in hydrothermal systems: the nature of porosity. Am. J. Sci.; United States, 277.

O'Brien, G. 1993. Some ideas on the rifting history of the Timor Sea from the integration of deep crustal seismic and other data. PESA Journal 21, 95-113.

O'Brien, G., Lisk, M., Duddy, I. R., Hamilton, J., Woods, P. 1999a. Plate convergence, foreland development and fault reactivation : primary controls on brine migration , thermal histories and trap breach in the Timor Sea , Australia 16, 533–560.

O'Brien G., Morse M., Wilson D., Quaife P., Colwell J., Higgins R., Foster C. B. 1999b. Margin-scale, basement-involved compart- mentalization of Australia's North West Shelf: a primary control in basin-scale rift, depositional and reactivation histories. The APPEA Journal 39, 40–63.

Ocamb, R. D. 1961. Growth faults of south Louisiana.

Peacock, D. C. P. 2002. Propagation, interaction and linkage in normal fault systems. Earth-Science Reviews 58, 121-142.

Peacock, D. C. P., Sanderson, D. J. 1991. Displacements, segment linkage and relay ramps in normal fault zones. Journal of Structural Geology 13, 721-733.

Peacock, D. C. P., Sanderson, D. J. 1994. Geometry and development of relay ramps in normal fault systems. AAPG Bulletin 78, 147-165.

Perrin, C., Manighetti, I., Gaudemer, Y. 2015. Off-fault tip splay networks: A genetic and generic property of faults indicative of their long-term propagation. Comptes Rendus Geoscience 348, 52-60.

Prucha, J. J. 1992. Zone of weakness concept: A review and evaluation. In Basement Tectonics 8, 83-92. Springer Netherlands.

Putz-Perrier, M. W., Sanderson, D. J. 2008a. The distribution of faults and fractures and their importance in accommodating extensional strain at Kimmeridge Bay, Dorset, UK. Geological Society, London, Special Publications 299, 97-111.

Putz-Perrier, M. W., Sanderson, D. J. 2008b. Spatial distribution of brittle strain in layered sequences. Journal of Structural Geology 30, 50-64.

Quigley, M., Van Dissen, R., Litchfield, N., Villamor, P., Duffy, B., Barrell, D., Furlong, K., Stahl, T., Bilderback, E., Noble, D. 2012. Surface rupture during the 2010 Mw 7.1 Darfield (Canterbury) earthquake: Implications for fault rupture dynamics and seismic-hazard analysis. Geology 40, 55–58.

Ravnås, R., Nøttvedt, A., Steel, R. J., Windelstad, J. (2000). Syn-rift sedimentary architectures in the Northern North Sea. Geological Society, London, Special Publications 167, 133-177.

Reeve, M. T., Bell, R. E., Duffy, O. B., Jackson, C. A. L., Sansom, E. 2015. The growth of non-colinear normal fault systems; What can we learn from 3D seismic reflection data?. Journal of Structural Geology 70, 141-155.

Richard, P., Krantz, R. W. 1991. Experiments on fault reactivation in strike-slip mode. Tectonophysics 188, 117-131.

Richards, F. L., Richardson, N. J., Bond, C. E., Cowgill, M. 2015. Interpretational variability of structural traps: implications for exploration risk and volume uncertainty. Geological Society, London, Special Publications 421, 7-27.

Rotevatn, A., Fossen, H., Hesthammer, J., Aas, T. E., Howell, J. A. 2007. Are relay ramps conduits for fluid flow? Structural analysis of a relay ramp in Arches National Park, Utah. Geological Society, London, Special Publications 270, 55-71.

Rouby, D., Raillard, S., Guillocheau, F., Bouroullec, R., Nalpas, T. 2002. Kinematics of a growth fault / raft system on the West African margin using 3-D restoration. Journal of Structural Geology 24, 783–796.

Roure, F., Brun, J. P., Colletta, B., Van Den Driessche, J. 1992. Geometry and kinematics of extensional structures in the Alpine foreland basin of southeastern France. Journal of Structural Geology 14, 503-519.

Sassi, W., Colletta, B., Bale, P., Paquereau, T. 1993. Modeling of structural complexity in sedimentary basins: the role of pre-existing faults in thrust tectonics. Tectonophysics 226, 97–112.

Scholz, C. A., Hutchinson, D. R. 2000. Stratigraphic and structural evolution of the Selenga Delta accommodation zone, Lake Baikal Rift, Siberia. International Journal of Earth Sciences 89, 212-228.

Segall, P., Pollard, D. D. 1980. Mechanics of discontinuous faults. Journal of Geophysical Research: Solid Earth 85, 4337-4350.

Segall, P., Pollard, D. D. 1983. Nucleation and growth of strike slip faults in granite. Journal of Geophysical Research: Solid Earth 88, 555-568.

Sibson, R. H. 1985. A note on fault reactivation. Journal of Structural Geology 7, 751-754.

Sibson, R.H. 1989. Earthquake faulting as a structural process. Journal of Structural Geology 11, 1–14.

Sibson, R. H. 1995. Selective fault reactivation during basin inversion: potential for fluid redistribution through fault-valve action. Geological Society, London, Special Publications 88, 3-19.

Sieh, K., Jones, L., Hauksson, E., Hudnut, K., Eberhart-Phillips, D., Heaton, 1993. Near-field investigations of the Landers earthquake sequence, April to July 1992. Science, 260, 171-171.

Soliva, R., Benedicto, A. 2004. A linkage criterion for segmented normal faults. Journal of Structural Geology 26, 2251-2267.

Soliva, R., Schultz, R. A. 2008. Distributed and localised faulting in extensional settings: insight from the North Ethiopian Rift–Afar transition area. Tectonics 27.

Shuster, M. W., Eaton, S., Wakefield, L. L., Kloosterman, H. J. 1998. Neogene tectonics, greater Timor Sea, offshore Australia: implications for trap risk. The APPEA Journal 38, 351-379.

Stephenson, A. E., Cadman, S. J. 1994. Browse Basin, northwest Australia: the evolution, palaeogeography and petroleum potential of a passive continental margin. Palaeogeography, Palaeoclimatology, Palaeoecology 111, 337-366.

Struckmeyer, H. I., Blevin, J. E., Sayers, J., Totterdell, J. M., Baxter, K., Cathro, D. L. 1998. Structural evolution of the Browse Basin, North West Shelf: new concepts from deep-seismic data. In The Sedimentary Basins of Western Australia 2: Proceedings of the Petroleum Exploration Society of Australia Symposium, Perth, 345-367.

Symonds, P. A., Collins, C. D. N., Bradshaw, J. 1994. Deep structure of the Browse Basin: implications for basin development and petroleum exploration. In The Sedimentary Basins of Western Australia: Proceedings of the Petroleum Exploration Society of Australia Symposium, Perth, 315-331.

Teichert, C. 1939. The Mesozoic transgressions in western Australia. University of Western Australia. Department of Geology.

Teichert, C. 1951. The marine permian faunas of Westcrn Australia. Paläontologische Zeitschrift 24, 76-90.

Trudgill, B., Cartwright, J. 1994. Relay-ramp forms and normal-fault linkages, Canyonlands National Park, Utah. Geological Society of America Bulletin, 106, 1143-1157.

Tvedt, A. B., Rotevatn, A., Jackson, C. A. L., Fossen, H., Gawthorpe, R. L. 2013. Growth of normal faults in multilayer sequences: a 3D seismic case study from the Egersund Basin, Norwegian North Sea. Journal of Structural Geology 55, 1-20.

Veevers, J. J., Powell, C. M., Roots, S. R. 1991. Review of seafloor spreading around Australia. I. Synthesis of the patterns of spreading. Australian journal of earth sciences 38, 373-389.

Walsh, J. J., Bailey, W. R., Childs, C., Nicol, A., Bonson, C. G. 2003. Formation of segmented normal faults: A 3-D perspective. Journal of Structural Geology 25, 1251–1262.

Walsh, J.J., Nicol, A., Childs, C. 2002. An alternative model for growth of faults. Journal of Structural Geology 24, 1669-1675.

Walsh, J. J., Watterson, J. 1987. Distributions of cumulative displacement and seismic slip on a single normal fault surface. Journal of Structural Geology 9, 1039-1046.

Walsh, J. J., Watterson, J. 1988. Analysis of the relationship between displacements and dimensions of faults. Journal of Structural Geology 10, 239-247.

Walsh, J. J., Watterson, J., Bailey, W. R., Childs, C. 1999. Fault relays, bends and branch-lines. Journal of Structural Geology 21, 1019-1026.

Wesnousky, S. G. 1986. Earthquakes, Quaternary faults, and seismic hazard in California. Journal of Geophysical Research. Solid Earth 91, 12587-12631.

Whipp, P. S., Jackson, C., Gawthorpe, R. L., Dreyer, T., Quinn, D. 2014. Normal fault array evolution above a reactivated rift fabric; a subsurface example from the northern Horda Platform, Norwegian North Sea. Basin Research 26, 523-549.

Willis, I. 1988. Results of exploration, Browse Basin, North West Shelf, Western Australia. In The North West Shelf, Australia: Proceedings of the Petroleum Exploration Society of Australia Symposium, Perth, 259-272.

Wiprut, D., Zoback, M. D. 2000. Fault reactivation and fluid flow along a previously dormant normal fault in the northern North Sea. Geology 28, 595-598.

Woods, E. P. 1992. Vulcan Sub-basin fault styles—implications for hydrocarbon migration and entrapment. The APPEA Journal 32, 138-158.

Yeates, A. N., Bradshaw, M. T., Dickins, J. M., Brakel, A. T., Exon, N. F., Langford, R. P., Yeung, M. 1987. The Westralian superbasin: an Australian link with Tethys. In International symposium on Shallow Tethys 2, 199-213.

Zhang, X., Sanderson, D. J. 1996. Numerical modelling of the effects of fault slip on fluid flow around extensional faults. Journal of Structural Geology 18, 109-119.

Zhang, X., Sanderson, D. J. 1998. Numerical study of critical behaviour of deformation and permeability of fractured rock masses. Marine and Petroleum Geology 15, 535-548.

Appendix A – Workflow interpretation in Petrel 2013

Horizon and fault interpretation

Horizon interpretation is done by following a deviating amplitude from zero crossing. Either a downward increase in acoustic impedance (peak) or a downward decrease in acoustic impedance (trough). Zero-crossing separates the two amplitudes. Peaks are displayed in red, whereas troughs are displayed in blue. Zero-crossings are displayed in thin grey bands (Fig.11.1).
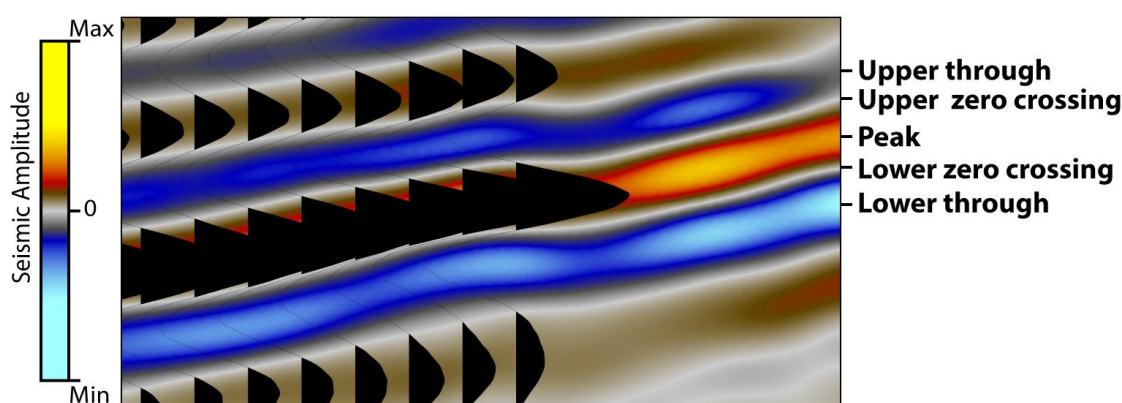
Figure. 11.1: Window clipart from seismic data with labelled peak, through and zero crossing. The left part of the seismic include both the wavelet phase and the amplitudes.

Horizons from Turonian and upwards has been interpreted with a combination of Manual interpretation with the shift-button pressed down and 2D-Autotracking with a sufficient seed-confidence. 3D-autotracking was used in some areas when the reflector had a very high amplitude. The 3D-autotracking was used mostly in the end when enough manual lines were interpreted. Applying autotracking systematically with high seeding-confidence in the beginning and work towards lower values. Until most of the 3D-Cube is tracked and the autotracking still makes reasonable choices. By using a combination of these three techniques, the interpretation is done in an effective and controlled way. In areas with extensive faulting, precautions were made to autotracking, and extra lines were interpreted perpendicular to the fault planes. In these areas, the measuring tool and ghost tool gave good guidance to determine the right reflector in the hanging wall and footwall.

For horizons interpreted below Turonian it was only used manual-interpretation with some contribution of holding the shift-button while interpreting in areas where it was of any help. To follow one specific reflector in lower part was very challenging due to poor reflectors. Fault

interpretation was done by a combination of interpretation in both interpretation window and map-view. The faults located above Turonian was very straight forward to map in the interpretation window. With the help of variance map in map-view to connect each individual fault correctly.

After sufficient amounts of interpretation, surface maps were created for each of the interpreted horizons except Lower Miocene and Base Eocene. Base Cretaceous was truncated in the northernmost part of the seismic cube, all other horizons covered the whole area.

Appendix B – Workflow fault model in Petrel 2013

Generate the fault model

1. Create a fault model for each separate fault population. The first step is to create a model: "Corner point gridding" – "define model" – "apply".

2. The new model is in **models**, highlight the created model by one left click to make it active.

3. Go back to **input** and right click on the folder with the interpreted fault polygons – "convert to faults in fault model".
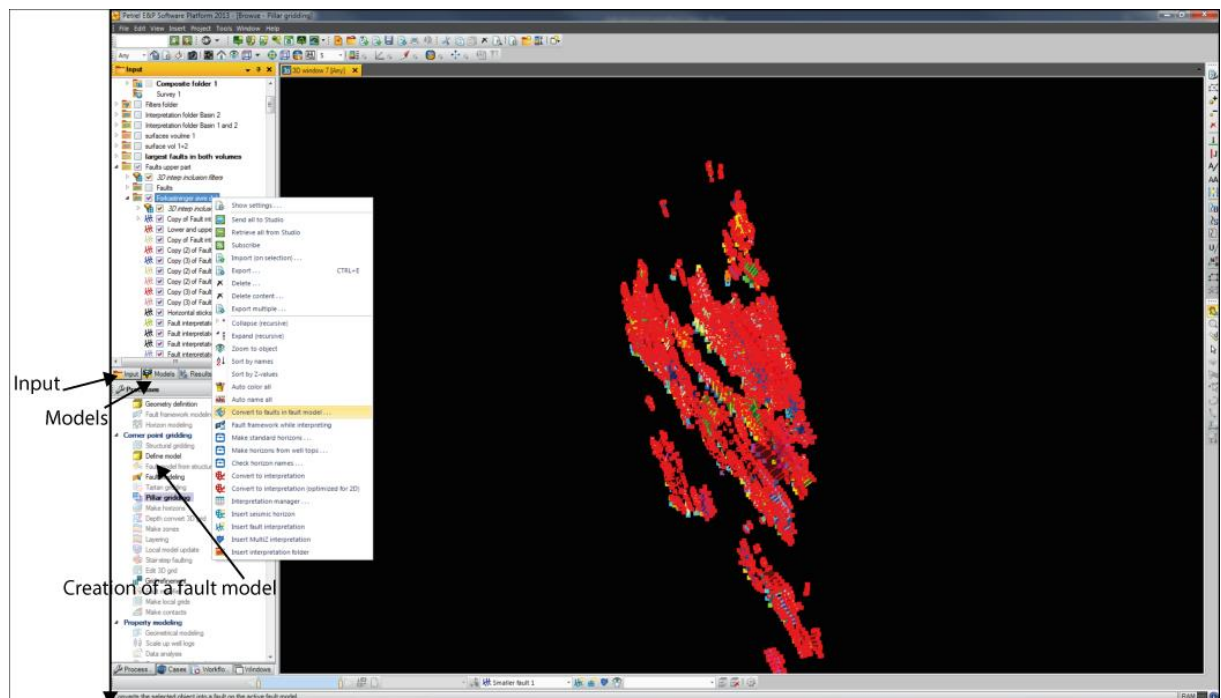
4. Double left click on fault modelling to open the menu, insert desired surface horizons by highlighting the surface and left-clicking on the blue arrow. Choose desired option, then cutting/extending the fault planes left click on cut/extend. It´s also possible to do automatic fault connection between separate polygons. Choose desired distance and left-click on auto connect. Finish by left-clicking on "apply". The fault planes can also be modified in the 3D window with the use of several tools.
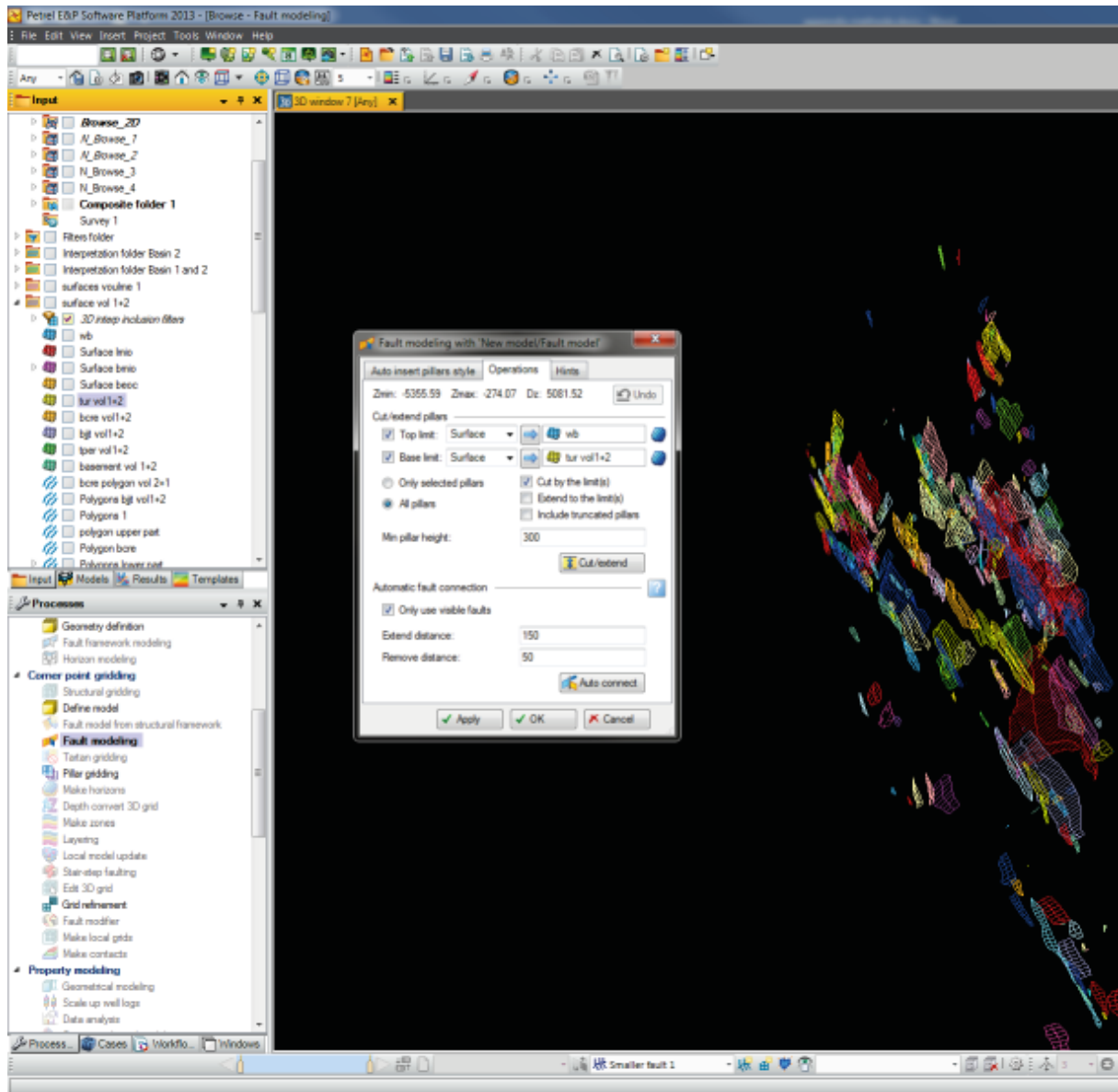
5. The next step is Pillar gridding where three skeletons (lower, middle and upper) are created to the faults, where the increments and the pillar geometries are chosen. This must be completed in a 2D window with every fault in the fault model turned on. First step is to make boundary around the faults with the "boundary tool" – "apply". If some faults are causing trouble it will stop and an error message will appear. The faults that needs to be fixed, if not excluded from the model, are highlighted. These faults can be fixed by tools on the right-hand side. After pressing "apply" the first skeleton is created, press "OK" to develop the two remaining skeletons.
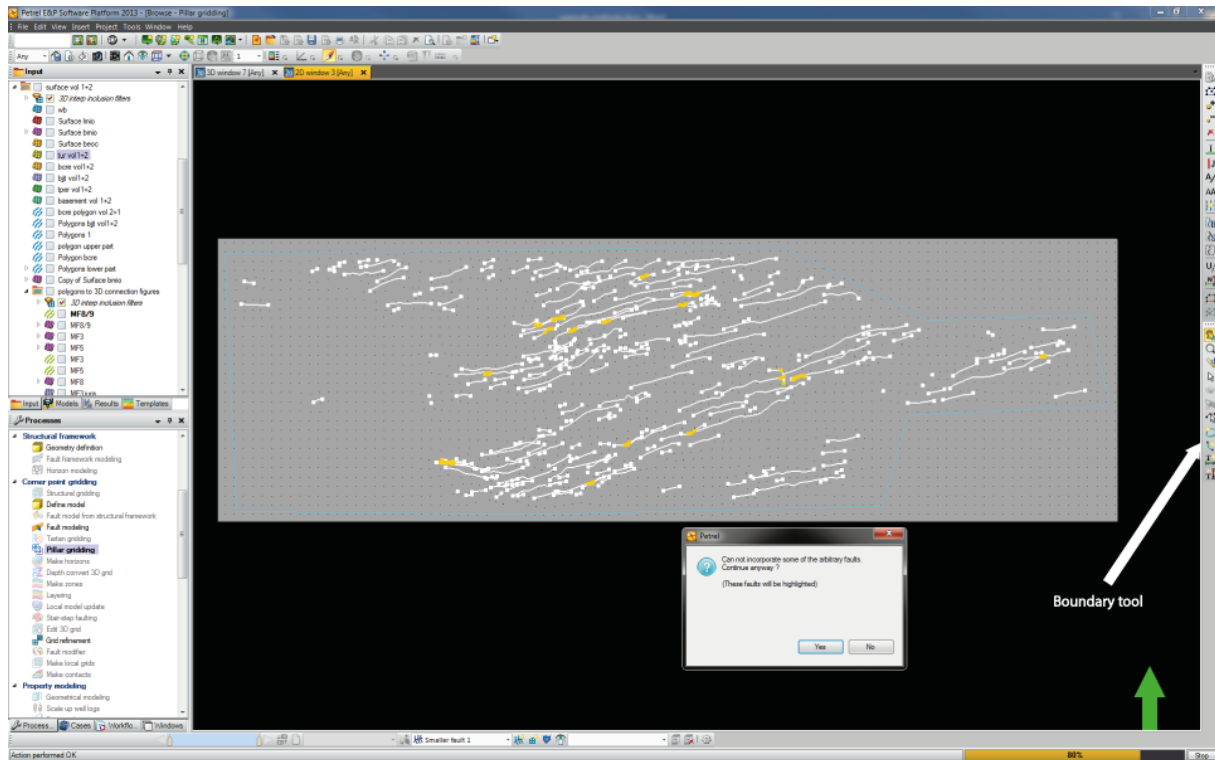
6. When the pillar gridding is done, horizons can be incorporated in the model, by pressing "Make horizon" – "Horizons". The input are the surface maps made from interpretation. Add locations for surfaces by pressing the "insert" buttons. Highlight the desired surface and press the blue arrow underneath "Input #1". Repeat for all horizons in stratigraphic order. When all the surfaces are in place, the cut-off values for hanging wall and footwall can be set in the "Faults" tab by ticking on "diff. sides". The values can be set differently for the different horizons and for each of the faults. Finish with "OK".
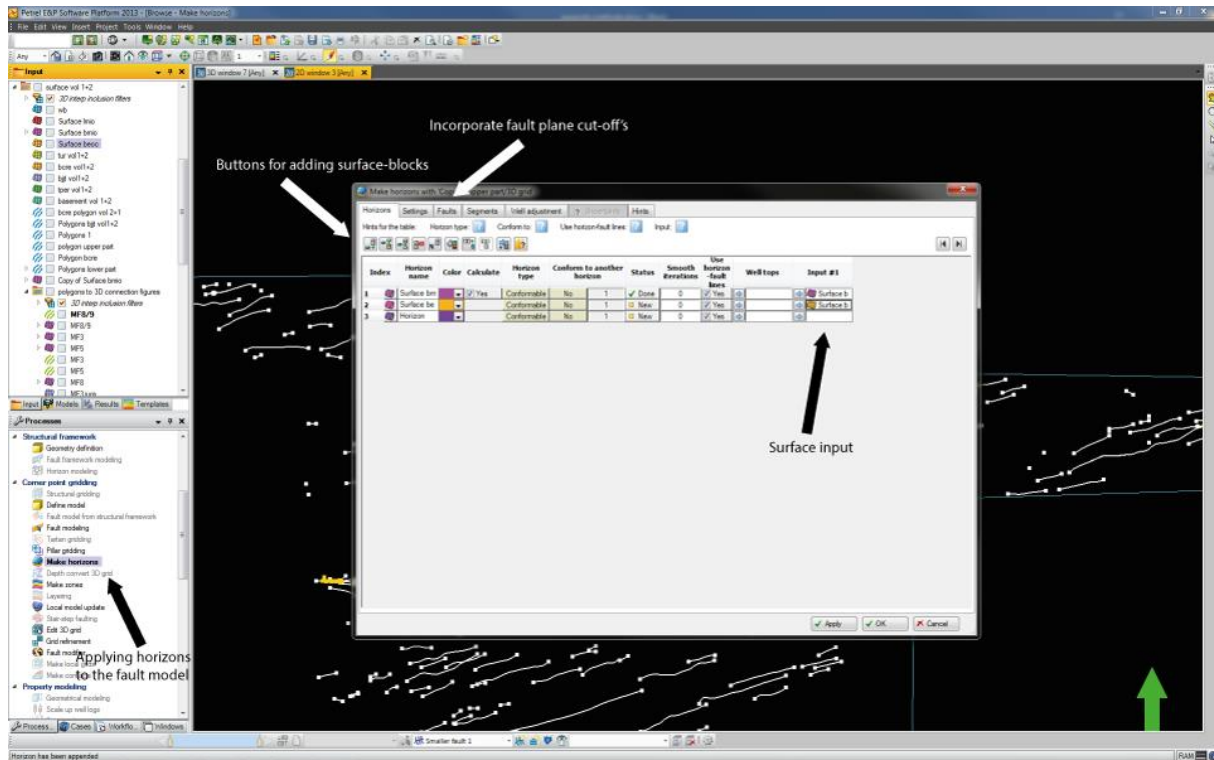
Surface maps from the fault model

7. Creation of surface maps with the faults cut out: Expand "3D Grid" – right-click "horizons" – "converte to structured surface". For more details right-click "Horizons" – "Settings for horizons" – "Operations".

Isochore maps from the fault model

8. Creation of isochore maps with fault cut out: right click Expand "3D Grid" – right click "Zone filter" – Show settings – Convert zone(s) to isochore. Input the desired surface in template surface. Remove tic in the box: Fill in faulted areas. Press OK.

Generate and extract throw values from the fault model

9. Generate throw values along each fault for all horizons: Expand "3D Grid – right click "faults" – "Structural operations" – "Throw profile" – Choose desired horizon for throw values – "Run". The values will appear in the **input** catalogue in "RDR throw profiles".

10. Expand "throw point data" – highlight all the faults that you want to extract. Right click – "export multiple" – Save as format: "Petrel points with attributes (ASCII)(*.*)".
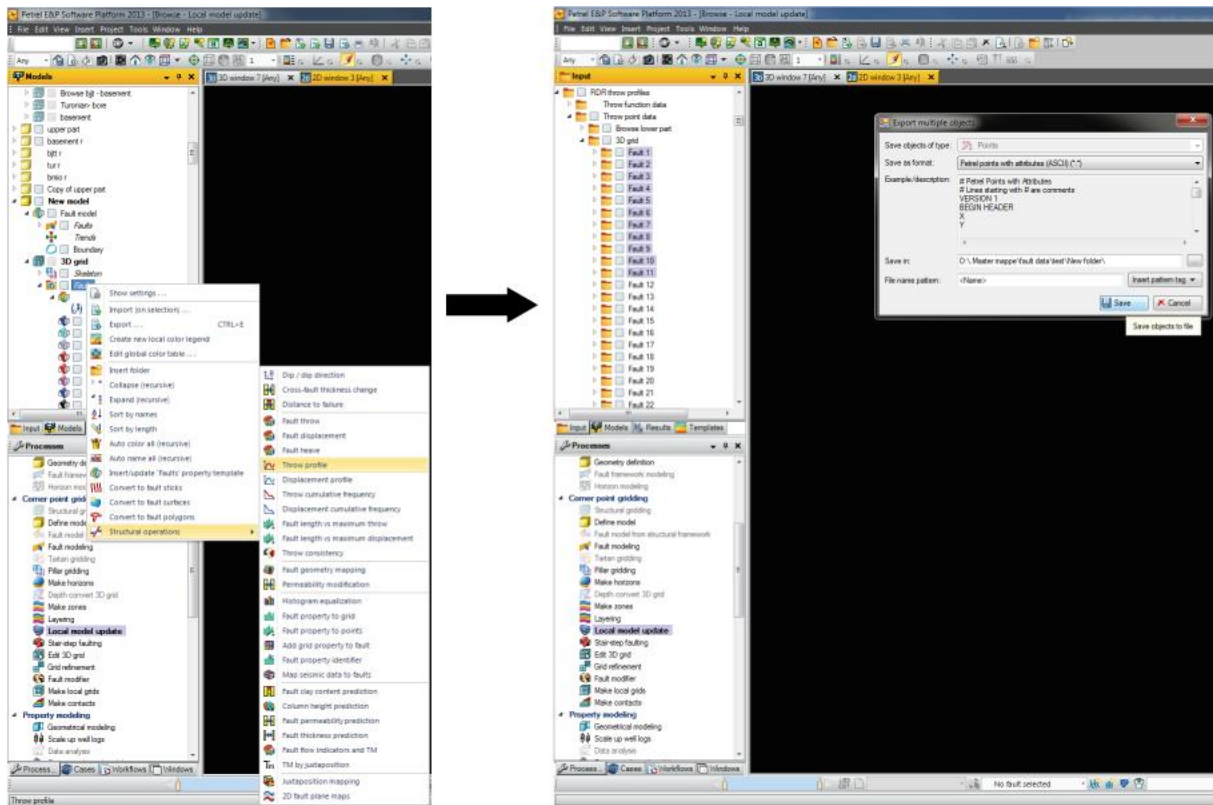
Import data to Excel format

11. Each fault file must be imported separately in the following way: open the file in Excel – "delimited" – "Next" – Delimiters tic on "Space" – Left click the column with the throw values and click on "Text" – "Finish".

12. Add X, Y, Z, Z, D and T manually at the top. Then add a fault number and repeat step 11. Copy all fault data in to one single excel file.
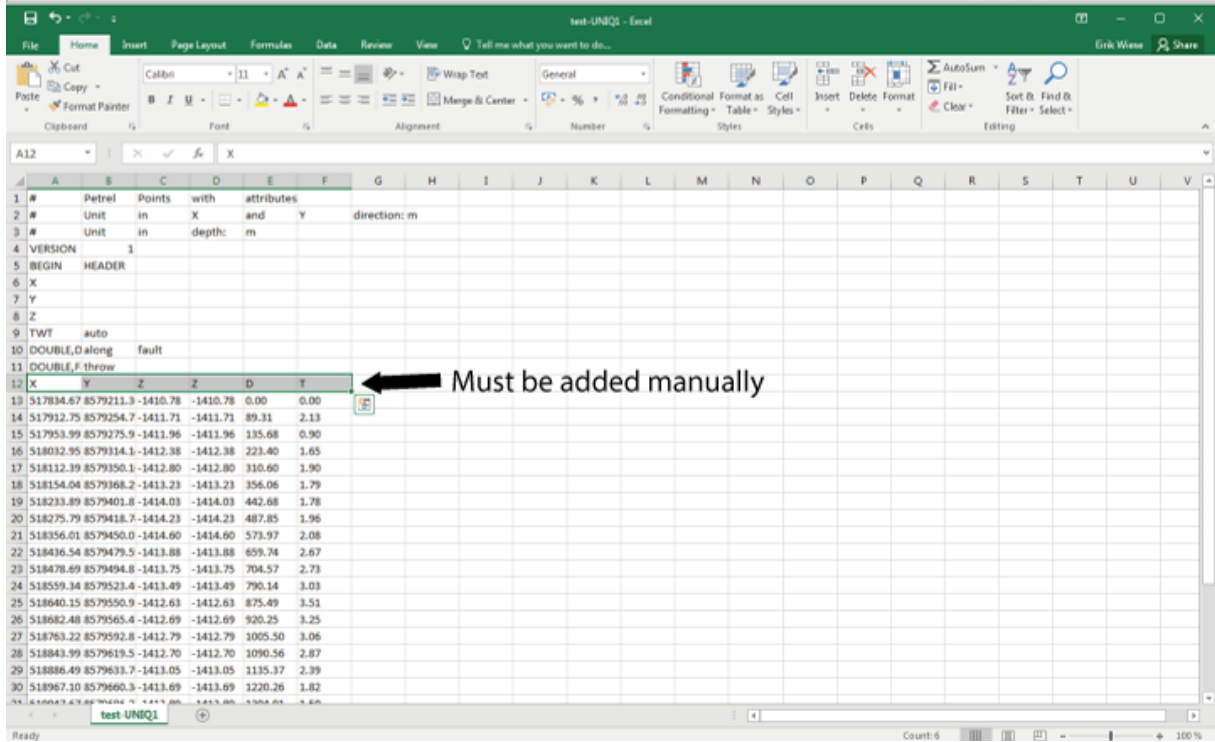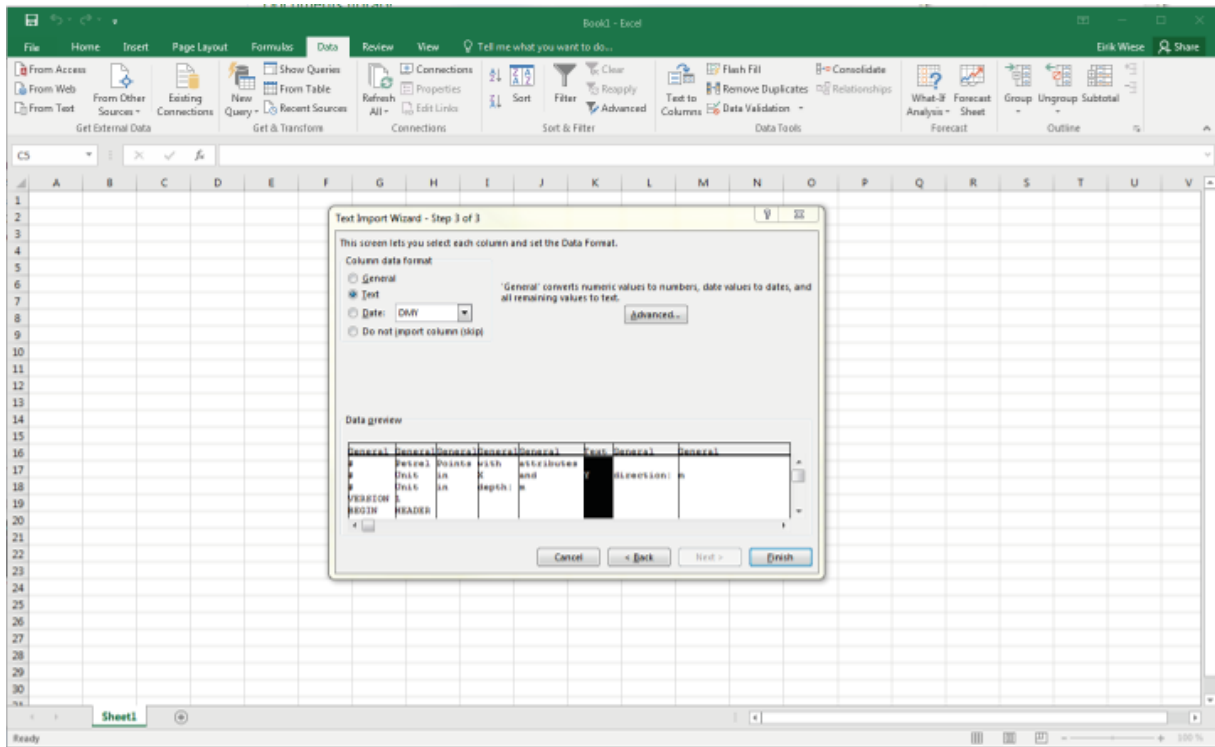
Appendix C – Additional results
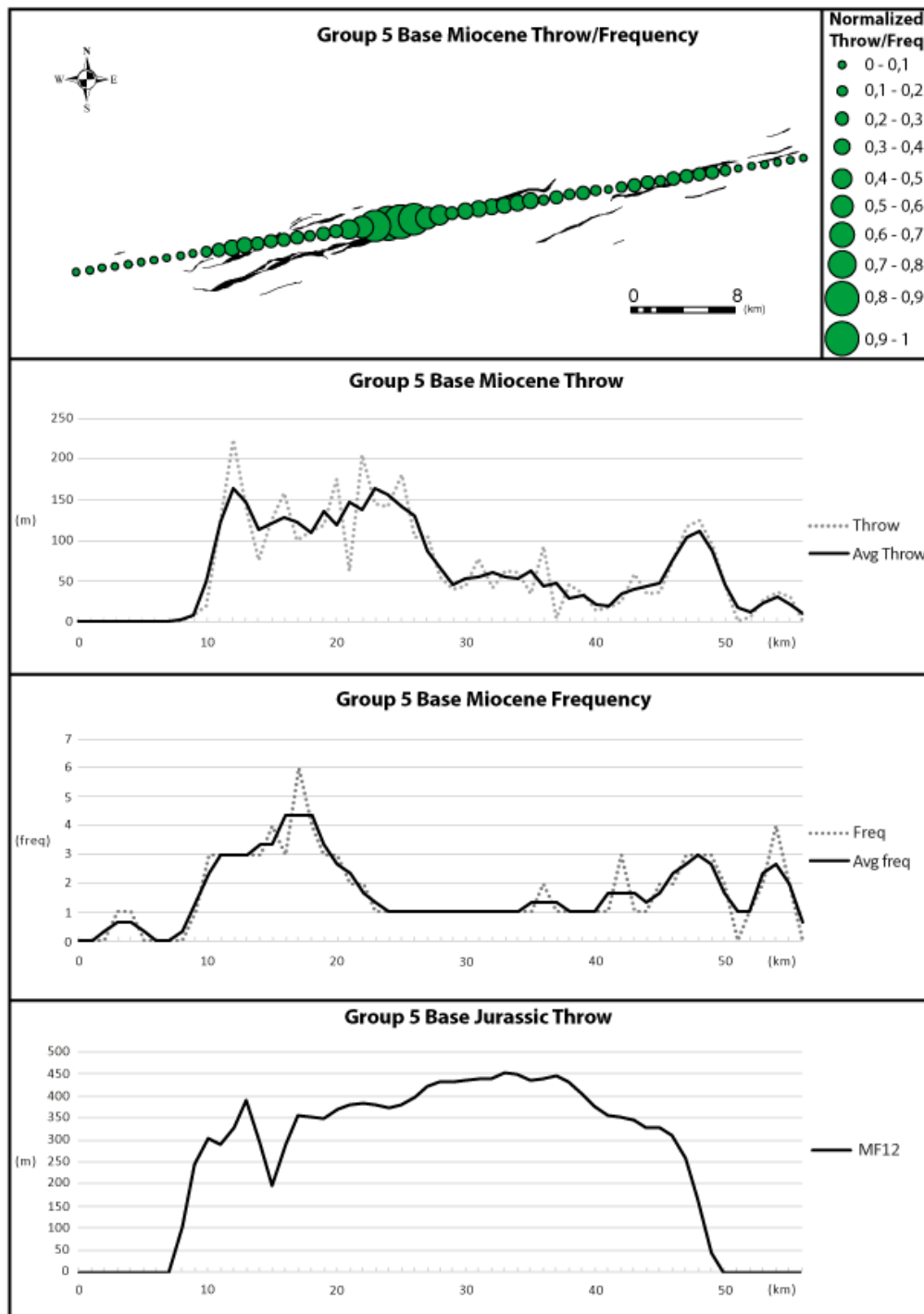
Figure. 11.2: All profiles are oriented West-East, and are aligned after same scales, with same sampling spacing. **Group 5 Base Miocene Throw/Frequency** is displayed as green circles with sizes according to scale. The Neogene faults within the group are displayed underneath. **Group 5 Base Miocene** have cumulative throw as stippled, and three-points weighted average as a solid black line. **Group 5 Base Miocene Frequency** have cumulative frequency as stippled, and three-points weighted average as a solid black line. **Group 5 Base Jurassic Throw** have MF12's throw values as a solid black line.
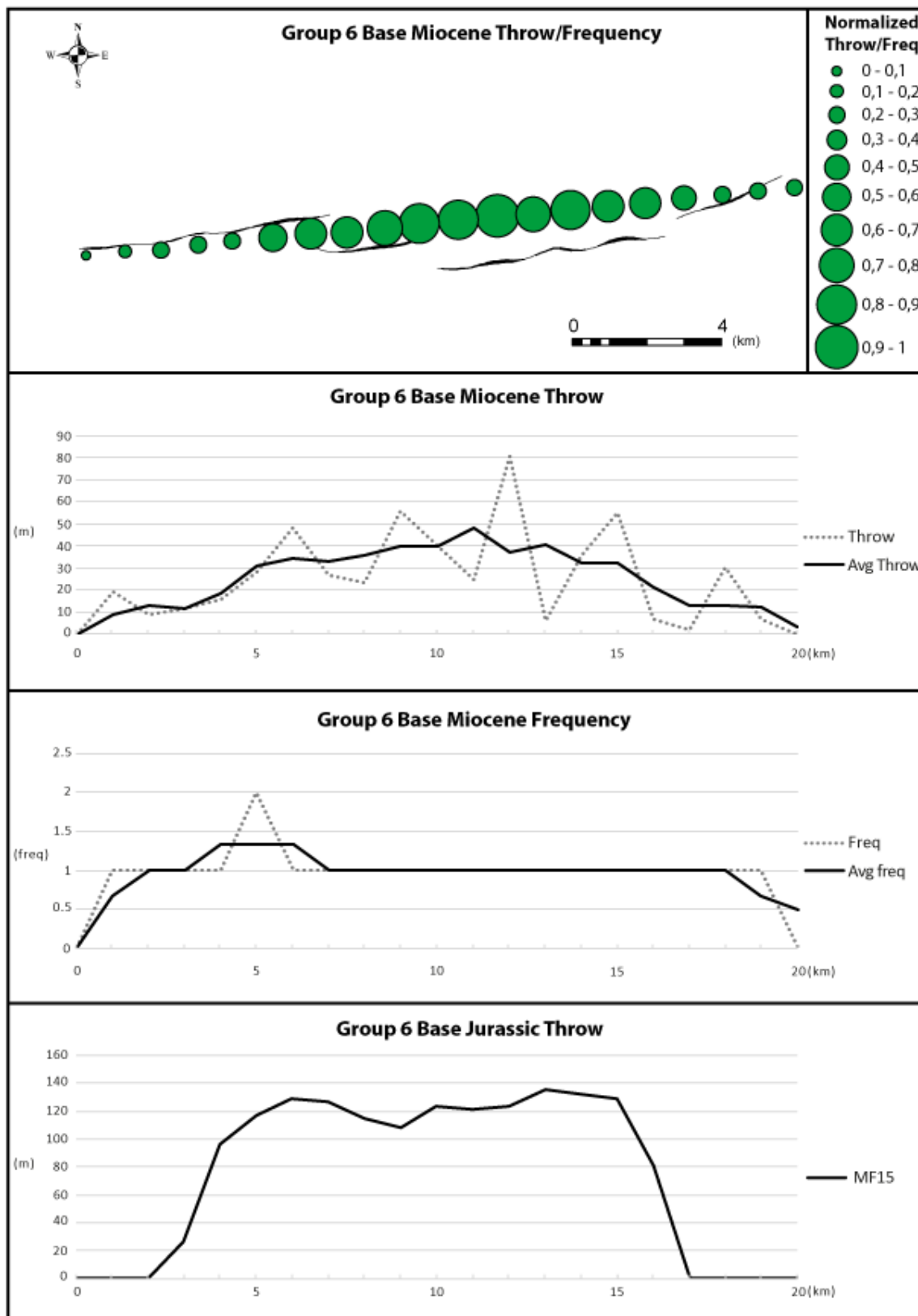
Figure. 11.3: All profiles are oriented West-East, and are aligned after same scales, with same sampling spacing. **Group 6 Base Miocene Throw/Frequency** is displayed as green circles with sizes according to scale. The Neogene faults within the group are displayed underneath. **Group 6 Base Miocene** have cumulative throw as stippled, and three-points weighted average as a solid black line. **Group 6 Base Miocene Frequency** have cumulative frequency as stippled, and three-points weighted average as a solid black line. **Group 6 Base Jurassic Throw** have MF15's throw values as a solid black line.

105